Doctor of Philosophy

Metal Oxide Catalysts Applied for Carbon Dioxide Electroreduction Reaction

The Graduate School of the University of Ulsan

Department of Chemical Engineering

Hongyan Yu

Metal Oxide Catalysts Applied for Carbon Dioxide Electroreduction Reaction

Supervisor: Professor Eun Woo Shin

Professor Yong Men

A Dissertation Submitted to

The Graduate School of the University of Ulsan

In partial Fulfillment of the Requirements

for the Degree of

Doctor of Philosophy

by

Hongyan Yu

School of Chemical Engineering

Ulsan, South Korea

(October 2021)

Metal Oxide Catalysts Applied for Carbon Dioxide Electroreduction Reaction

This certifies that the dissertation

of Hongyan Yu is approved.

Committee Chair Professor Sung Gu Kang

Committee Member Professor Eun Woo Shin

Committee Member Professor Ik Keun Yoo

Committee Member Professor Won Mook Choi

Committee Member Professor Yong Men

Department of Chemical Engineering

Ulsan, South Korea

(October 2021)

ABSTRACT

Due to a recent rapid increase of the CO_2 concentration in the Earth's atmosphere, there is a worldwide necessity to search for suitable and capable catalytic systems for CO_2 conversion. Since electrochemical reduction of CO_2 (CO_2RR) is a promising approach, the work presented in this dissertation deal with the greenhouse gas CO_2 by using metal oxide catalysts to convert it to value-added fuels. The main statement is to produce electrocatalysts which can be applied for CO_2 electroreduction.

In Part I, we prepared hexagonal and monoclinic phases of $La_2O_2CO_3$ nanoparticles by different wet preparation methods and investigated their phase-related CO_2 behavior through field-emission scanning microscopy, high-resolution transmission electron microscopy, Fourier transform infrared, thermogravimetric analysis, CO_2-temperature programmed desorption, and linear sweeping voltammetry of CO_2 electrochemical reduction. The monoclinic $La_2O_2CO_3$ phase was synthesized by a conventional precipitation method via $La(OH)CO_3$ when the precipitation time was longer than 12 h. In contrast, the hydrothermal method produced only the hexagonal $La_2O_2CO_3$ phase, irrespective of the hydrothermal reaction time. The $La(OH)_3$ phase was determined to be the initial phase in both preparation methods. During the precipitation, the $La(OH)_3$ phase was transformed into $La(OH)CO_3$ owing to the continuous supply of CO_2 from air whereas the hydrothermal method of a closed system crystallized only the $La(OH)_3$ phase. Based on the CO_2-temperature programmed desorption and thermogravimetric analysis, the hexagonal $La_2O_2CO_3$ nanoparticles (HL-12h) showed a higher surface CO_2 adsorption and thermal stability than those of the monoclinic $La_2O_2CO_3$ (PL-12h). The crystalline structures of both $La_2O_2CO_3$ phases predicted by the density functional theory calculation explained the difference in the CO_9 behavior on each phase. Consequently, HL-12h showed a higher current density and a more positive onset potential than PL-12h in CO_2 electrochemical reduction.

In Part II, ZnO /$La_2O_2CO_3$ composite materials have been used as a catalyst for CO_2 electroreduction reactions and the morphology of macropores an important factor to influence on

catalyst performance. In this study, we prepared $La_2O_2CO_3$/ZnO composite materials by two different methods – precipitation (CoLZ) and ethylene glycol combustion (LZ) – as functions of La/Zn ratios and calcination temperatures. All of the materials prepared by the solution combustion method clearly showed disordered macroporous morphology whose framework was composed of ZnO and $La_2O_2CO_3$ nanoparticles. The addition of ZnO can promote the production of CO, and the dominant products of ZnO/$La_2O_2CO_3$ are CO. The CO_2RR onset potential of CoLZ was more negative than those of the LZ, and LZ showed the lower interfacial charge transfer resistance. Moreover, the LZ sample can form C_2H_4 products by further converting the CO.

In Part III, Cu/$La_2O_2CO_3$ composite materials have been used as a catalyst for CO_2 electroreduction reactions and the loading of copper can cause phase conversion, which play an important role in the catalyst performance. In this study, we prepared $La_2O_2CO_3$ support by ethylene glycol combustion (EL) and the copper was doped through hydrothermal method-as functions of Cu/$La_2O_2CO_3$ ratios. The materials prepared clearly showed copper lattice grew into disordered macroporous framework. EL-Cu-*x* series catalysts were well prepared by hydrothermal method and the main phase of copper was converted from CuO to $Cu_2(OH)_3Cl$ with the increasing content of copper precursor. The unique nanostructures cuprous chloride derived Cu can suppress the HER and enhance the CO_2RR catalytic performance. For further improving the electrical conductivity and surface area of the catalysts, the four kinds of carbon supports were employed. Except the carbon spheres were synthesized by hydrothermal method, the other three carbon supports including carbon nanotube, graphene oxide and activated carbon were commercially purchased. And it was found the largest surface area and mesoporous AC-Cu sample showed the highest CO_2RR catalytic activity (FE_{C2H4}=50.8%) which is keep consistent with its lowest interfacial electron transfer resistance.

ACKNOWLEDGEMENT

First and foremost, I would like to sincerely appreciate my advisors, Professor Eun Woo Shin and Professor Yong Men for giving me a generous guidance and expert advice through all stages of my research as well as the preparation of all the manuscripts for publication. Professor Shin always taught me patiently and gave me an allowance when I was in Ulsan. He always encouraged me to make new attempt in my research. Professor Men lets me know a researcher should also be proficient in equipment and machine. He always suggested us to think independently and combine our hands with brains to explore the science. He is strict but helpful. With the supervision of Professors, I know that I can overcome all the challenges by study and efforts. The life of being a researcher can be very meaningful and enriched. They taught me knowledge is infinite, not only in research but also in life.

I would like to thank all of the members of my committee, Professor Ik Keun Yoo, Professor Won Mook Choi, and Professor Sung Gu Kang for their advice and contributions to this work. I am also pleased to send my honor word to Professor Wei An, Professor Jing Guo Wang and Doctor Shuang Liu for their kindly support and help with my experiments.

Thanks to all my labmates in Ulsan, Thanh-Truc Pham, Do Thi Lien, Chan Yi Park, Kai Ming Jiang, Haewon Jung and Nguyen Phu Huy for their professional suggestions in researching and their friendships. They made me feel warm and adapt to the life in Korea more easily.

To my juniors in SUES, Bei Jin, Min Chen, Shuo Li and Chao Song, thank you for accompany and help in my research and life. They make me become motivated and inspirated in my work. My roomates Yu Jia Fu and Xing Ai Li, they are always beside me whether hard or cheerful, thank you for taking care of me a lot.

Last but not least, a deep gratitude to my family, my Dad, my Mom and my younger brother. They always believe in me and give me inspiration throughout my graduate study. Special thanks to my boyfriend for your love, care, support, advice during these nine years.

TABLE OF CONTENTS

LIST OF FIGURES

LIST OF TABLES

NOMENCLATURES

Abbreviations

EDX	Energy Dispersive X-ray spectra
EIS	Electrochemical Impedance Spectroscopy
FE-SEM	Field Emission Scanning Electron Microscopy
FFT	Fast Fourier Transform
FT-IR	Fourier Transform Infrared Spectra
FWHM	Full width at half maximum
GO	Graphene Oxide
HR-TEM	High Resolution Transmission Electron Microscopy
IUPAC	International Union of Pure and Applied Chemistry
RGO	Reduced Graphene Oxide
TGA	Thermal Gravimetric Analysis
XPS	X-ray Photoelectron Spectroscopy
XRD	X-ray Diffraction

Roman and Greek letters

d_p	Pore diameter [nm]
d	Average crystallite size [nm]
q_e	Equilibrium adsorption capacity [mg/g]
S_{BET}	Specific surface area [m^2/g]
λ	Wavelength [nm]

PART I – OVERVIEW OF DISSERTATION

Chapter 1. Introduction

1.1. Overview

1.1.1. CO_2 emission

Due to the unprecedented technological innovation, progress, and prosperity driven by energy, an increasing amount of carbon emissions in the atmosphere has been caused by industrial activities. The industrial revolution, since the 1860s, and the exponential urbanization during last two decades caused a promising increase in the global atmospheric concentration of anthropogenic greenhouse gases, which contributed to most of the unprecedented global warming over the past decade (**Figure 1.1**). Furthermore, climate change results in a decline in global agricultural output because of low rainfall, fluctuation in seasons, and temperature rise [1]. Many places in the world are enduring drought and becoming not suitable for commercial farming any more. The soil and water degradation are probably to be accelerated by incessant temperature and precipitation changes. Nevertheless, adaptive behavior has the potential to alleviate these impacts because land use and management have been reported as having a deeper impact on soil conditions than the indirect influence of climate change[2]. Even if all emissions from human activities suddenly stop, climatic conditions would continue to change[3]. The current extent of the indiscriminate emission of greenhouse gases into the atmosphere and anthropogenic pollution could exacerbate ocean acidification, global warming, desertification, as well as changing weather conditions. Besides, food security, rising sea levels and severe storms affecting coastal areas, health problems, migration, and the growing economic losses are just some of the immediate influences of climate change. Anthropogenic CO_2 emission results from direct human activities on forestry and other land use, including deforestation, land clearing for agriculture, and soil degradation[4][5]. Other sources of anthropogenic CO_2 classified in this study are human respiration,

automobiles, power plant, and airplane emissions. It is worth noting that the exhalation of CO_2 during human respiration does not play any important role in the depletion of the ozone layer (a layer in the Earth's stratosphere that prevents most of the sun's ultraviolet radiation from reaching the Earth), global warming, and climate change[6]. The CO_2 emission into the atmosphere does not directly affect climate change. Actually, it depletes the ozone layer and exposes the Earth's surface to the ultraviolet radiations of the sun directly which brings about the global warming issue and then an incessant shift in global or regional climatic patterns of the Earth (climate change) occurs. A schematic illustration of the climate change evolution trend is presented in **Figure 1.2**.

Carbon dioxide (CO_2) is emitted from the burning of fossil fuels (e.g., coal, natural gas, and oils), solid waste, trees, and other biological material [7]. In addition, CO_2 can get emitted as product of certain chemical reactions (e.g., the production of cement). Human activities can also alter the carbon cycle, which add more CO_2 to the atmosphere and affect the capacity of natural sinks, such as forests. Though certain diversifications in land use (e.g., deforestation) can result in the emission of CO_2 into the atmosphere, the dominant human activity related to the emission of CO_2 is caused by the burning of fossil fuels for energy and transport[8]. As part of the carbon life cycle, plants can absorb carbon dioxide, thus it is naturally removed from the atmosphere (or sequestered). Moreover, the CO_2 emission from stationary point sources (e.g., power and cement production plants) can also be reduced by CO_2 capture, storage, and utilization. Co-gasification of coal with biomass materials during combustion in coal-fired power plants is another efficient approach for alleviating CO_2 emission[9].

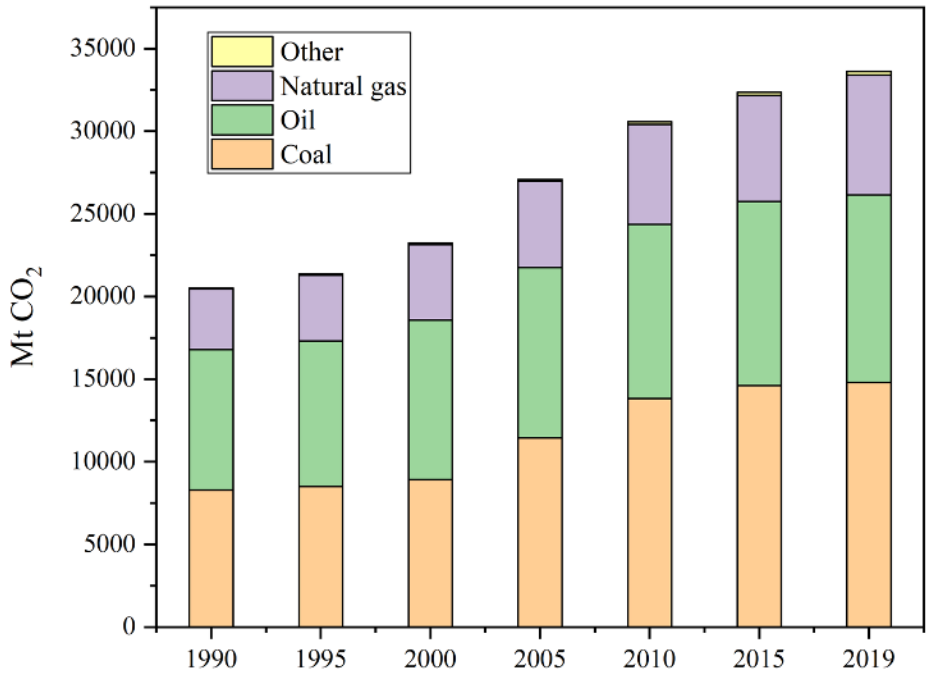

Figure 1.1. IEA, Global energy-related CO_2 emissions, 1990-2021, IEA, Paris.

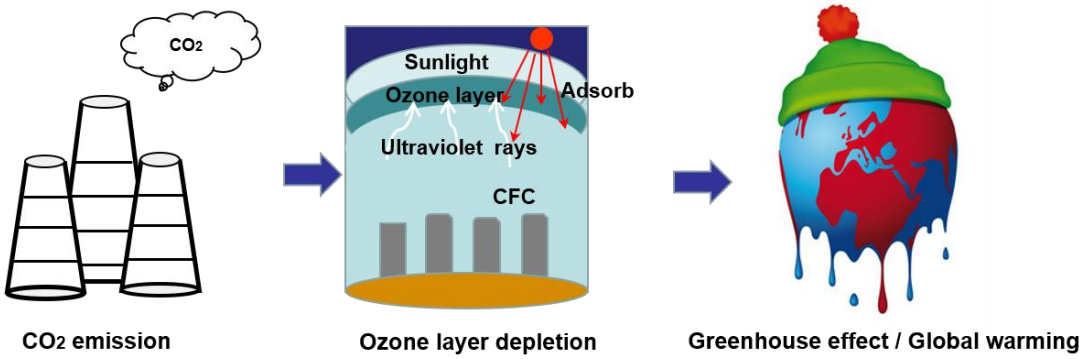

Figure 1.2. volution of global warming and climate change from the combustion of fossil fuels. Modified from How Carbon Capture Works, HowStuffWorks, 2008. 09 July.

1.1.2. CO_2 utilization approaches

The US Department of Energy's (DOE) Carbon Sequestration Program mainly focuses on the research fields in the CO_2 utilization consists of CO_2 reforming to hydrocarbons, manufacture of chemicals, mineralization and polymerization process[10]. All of these domains

have great potential to convert high capacities of CO_2 to value-added chemicals. There is still a huge challenge existed between CO_2 generated and CO_2 converted despite various products that can be obtained by CO_2. Thereupon, it is better to promote the utilization of renewable sources like wind, solar, hydrothermal and geothermal energies instead of fossil fuels. If these renewable energies are connected with different CO_2 utilization strategies, it paves the way for decreasing the atmospheric CO_2 to a great extent. In the recent years, researchers have taken advantages of plentiful approaches such as photocatalytic reduction of CO_2, electrochemical and thermal approaches for the CO_2 utilization and transformation[11]. The various approaches for CO_2 utilization and conversion into economical chemicals are shown in **Figure 1.3**. The advantages and disadvantages of CO_2 utilization approaches are summarized in the **Table 1.1**.

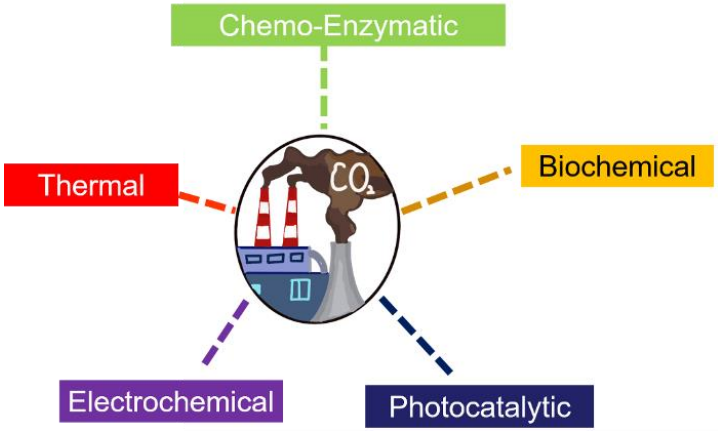

Figure 1.3. Different approaches for CO_2 utilization and conversion.

Table 1.1. Advantages and disadvantages of various CO_2 utilization approaches.

Approaches	Advantages	Disadvantages	References
6ftElectrochemical	● No additional heat is required ● Easy to scale-up ● Recycled electrolyte reduces the total electrolyte consumption ● Renewable energy source can be utilized ● High selectivity ● Long term stable operation	● Lifespan of catalyst is low ● Economically not feasible ● Required more electric energy	(Agarwal et al., 2011; Zhu, 2019)
Thermal	● Produce a high yield	● Required high temperature ● Stability of the catalyst is low	(Hu et al., 2013; Galadima and Muraza, 2019)
Photocatalytic	● Do not require additional energy ● Environment friendly ● Economically feasible	● Low product selectivity ● Produce a less yield	(Alper and Orhan, 2017; Gao et al., 2020)
Biochemical	● Toxic tolerance ● Higher selectivity ● Require low pressure and temperature	● Time consuming process ● Require high cost ● Produce a less yield ● Need specialized bioreactor	(Appel et al., 2013; Yaashikaa et al., 2019)
Chemo-enzymatic	● Produce bulk chemicals	● Require high temperature which affects enzyme activity	(Yong et al., 2015; Long et al., 2017)

1.1.2.1. Thermal approach

At present, due to its unfavorable impacts to the environment, it has caused the primary concern by researchers and industries to capture and utilize CO_2. Consequently, researchers have investigated lots of methods to convert CO_2 into value-added chemical feedstocks, fuels, etc[12]. Carbon monoxide (CO) can be formed through reverse water-gas shift (RWGS) reaction by the conversion of CO_2 and hydrogen[13]. The produced CO from RWGS can be employed in steel

fabrication, pharmaceutical and biotechnology-based industries[14]. The RWGS is an endothermic reaction happens at the high temperature (550-750 °C) and low pressure (0-5 bar).

$CO + H_2 \rightarrow CO + H_2O$ .....

$\Delta H = + 41$ kJ/mol ..... (1)

In view of the conditions of the reaction, it can conduct directly in both forward and reverse direction with adjusting the temperature and pressure slightly[15][16]. The dry reforming reaction can transform CO_2, natural gas and coal into syngas (CO and H_2), without water generation which is different from the RWGS process. The reaction occurs in the dry reforming process is given as:

$CO_2 + H_2 \rightarrow CO + H_2O$ ..... (2)

What's more, the yielded syngas can be further converted into hydrocarbons and chemical feedstocks. When the steam methane reforming is combined with the dry reforming reaction, syngas can also be produced and the bi-reforming reaction is given as:

$CH_4 + H_2O \rightarrow CO + 3H_2$ ..... (3)

$CO_2 + CH_4 \rightarrow 2CO + 2H_2$ ..... (4)

Moreover, tri-reforming is another reforming method which integrates the two reforming processes mentioned above (steam methane and dry reforming) and partial oxidation of methane. The distinguishing feature of this process is diverse hydrocarbon products can be yielded by regulating the CO and H_2 ratio[17]. It is expected that methanol can possibly replace the fossil fuels in the near future and methanol converted from CO_2 renewably serves as a promising method to diminish the atmospheric CO_2 concentration. The reaction is denoted by,

$CO + 2H_2 \rightarrow CH_3OH$ ..... (5)

The methanol converted from CO_2 is an exothermic reaction in property and it occurs at the temperature ranges of 210 - 290° C and 50 - 80 bar pressure. In addition, methanol can be

further converted to dimethyl ether through olefin or gasoline technology. Urea synthesis reaction is another pathway to utilize CO_2. It is a two-step process was given below,

$2NH_3 + CO_2 \rightarrow H_2N\text{-}COONH_4$ ..... (6)

$H_2N\text{-}COONH_4 \rightarrow (NH_2)_2CO + H_2O$..... (7)

Firstly, the carbamate is synthesized from the liquid ammonia and gaseous CO_2 **Eq. (6)** and then it can decompose into urea with water as byproduct which is explained in **Eq. (7)**. The formed urea can be employed as various fertilizers and polymers through urea formaldehyde synthesis reaction[18]. Unfortunately, these approaches can promote the CO_2 utilization, but most of these methods can also aggravate the emission of CO_2 [19].

1.1.2.2. *Biochemical approach*

Photochemical catalytic, electrochemical catalytic approaches are the most extensively developed pathways for the conversion of CO_2. Bio catalytic reaction can also be utilized own to their efficiency and toxicity tolerance despite its low yield, requirement of high pressure and temperature [20]. Biochemical reaction is to convert carbohydrates into simple sugars by enzymes or microbial catalyst with higher selectivity and low temperature [21]. Photochemical synthesis is to transform CO_2, water and sunlight to organic compounds naturally, which can fix carbon. The biotic system to is taken advantage to produce fuel from the biomass for the conversion of CO_2. Plants and prokaryotic organism can turn the CO_2 in the atmosphere into biomass through the Pentose phosphate pathway and the fructose 1, 6-bisphosphate and 1, 5-ribulosebisphosphate is released as intermediate in the process[22]. What's more, other biochemical CO_2 conversion pathways include acetyl-CoA pathway, reductive citric acid pathway and Fuchs-Holo cycle [23,24]. At present, the genetic engineering of algal metabolism is the primary research area so as to ameliorate the oil production [25-26]. In addition, cyanobacteria can also directly utilize CO_2 to produce diverse economical chemical feedstocks such as ethanol [27], iso-butanol [28], Isoprene [29], ethylene [30] and alkanes. In detail, the genetically engineered cyanobacteria Synechococcus

elongates can synthesize isopropanol by 26.5 mg/L [31-33]. Through the reductive Acetyl-CoA pathway, CO_2 can be converted into Acetyl-CoA by Acetogenic bacteria, which further yield acetic acid [34]. Methanogen microorganisms include Methanobacterium paulstre, Methanothermobacter marburgensis and Methanocaldococcus jannaschii, which can directly exploit the electrons generated in CO_2 reduction process to get methane [35]. However, due to its expensive cost and need of particular bioreactor, the bio-chemical CO_2 reduction technology is limited to be applied for industries [36]. Besides, the bio-chemical reaction may lead to the food shortage issue which is prevalent in the world because it needs to provide lots of nutrients to the microbial. In general, it can be an effective approach if the substrates in significant quantities are be used for modifying the microbes or the substrates that are the byproducts or wastes produced from the food industry are utilized such as corn steep liquor. Accordingly, the development of this pathway is primarily concerned about the technology of synthetic biology where genetic control of the organism can affect the biochemical reduction to synthesize the desired product in large scale [37].

1.1.2.3. Chemo-enzymatic approach

As mentioned above, the enzymatic method has several advantages such as the reactions don't require changeable conditions, higher yield and selectivity which is quite important in the current situation [38]. Chemo-enzymatic is the process applied in the industries which combines biocatalytic reaction to capture CO_2 released from the power plant for the production of bulk chemicals [39,40]. Diagrammatic illustration of chemo-enzymatic pathway for CO_2 utilization and reduction is shown in **Figure 1.4**. CO_2 is reduced to CO by [NiFe] carbon monoxide dehydrogenase, which further transformed into various value−added chemicals such as hydrocarbons, methanol and acetic acid [41]. Conversion of carbon-dioxide with enzyme has been extensively studied to generate formate, formic acid and methanol [42]. CO_2 can also be reduced to formate by the formate dehydrogenase extracted from the organism syntrophobacter fumaroxidans [43]. High efficiency of about 93% in the synthesis of formate is acquired by utilizing

the photo generated electrons. The CO_2 conversion to formate takes place by the following reactions [44],

$$CO_2 + H^+ + 2e^- \rightarrow HCOO^- \quad (8)$$

$$CO_2 + 2H^+ + 2e^- \rightarrow CO + H_2O \quad (9)$$

It is well known that methanol is one of the significant chemical products and it can be synthesized by the chemoenzymatic CO_2 reduction. When the electrochemical method was combined with chemo-enzymatic approach, Faradic efficiency of (FE) of about 10% could be achieved [45]. It is necessary to find other renewable energy to replace the electron source such as $NADPH^+$ /NADP couple which limits the reduction of CO_2 to methanol [46]. Moreover, Yang et al. have studied the enzyme nitrogenase for methane production and 21 nmol of methane can be yielded by 1 nmol of nitrogenase at optimal conditions [47]. Carbonic anhydrase (CA) can also catalyze the reduction of CO_2 into bicarbonate (HCO_3^-) with a higher reaction rate than other enzymes and the reaction for bicarbonate production is given below,

$$CO_2 + H_2O \rightarrow HCO_3^- + H^+ \quad (10)$$

During the CO_2 conversion process, carbonic anhydrase (CA) participates in both CO_2 capture and sequestration. Due to the high temperature reaction condition which affects the activity of the enzyme, the enzyme needs to be immobilized onto beads or other matrix materials. On the whole, the chemo-enzymatic approach can promote CO_2 capture and conversion to produce value-added chemicals stably [48]. The lyase enzyme can catalyze Michael addition reaction where the chemical bonds are broken and it can also be applied for the carboxylation of molecules to produce various chemical feedstocks [49]. There carboxylation reaction includes four types: (i) Carboxylation of epoxides, (ii) Carboxylation of aromatics, (iii) Carboxylation of hetero aromatics and (iv) Carboxylation of aliphatic Substrates. Currently, the multi-enzyme system for the conversion of CO_2 have been extensively studied to synthesize iso-butyraldehyde [50], sugars [51] and L-Lactic acid.

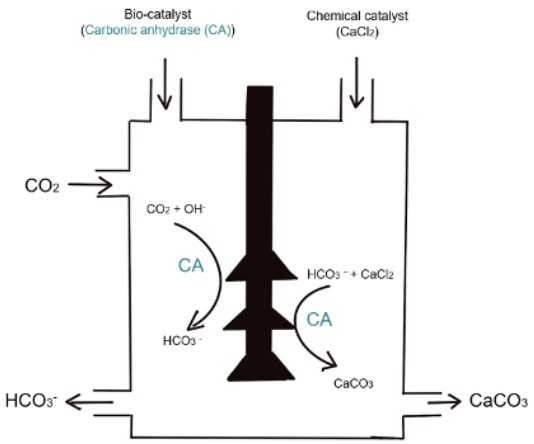

Figure 1.4. Chemo-enzymatic CO_2 utilization and conversion.

1.1.2.4. Photocatalytic approach

Photocatalytic CO_2 conversion is one of the hotpots in the research area, which reduces CO_2 into useful products under light irradiation by photocatalyst, which is the light sensitive catalyst [52]. The superiority of this technique is its energy efficiency and sustainability compared with electrochemical, thermal CO_2 reduction approaches. The graphic illustration of CO_2 photocatalytic conversion process is shown in **Figure 1.5**. However, it has poor product selectivity, so many researches purpose to optimize it by exploiting new types of photocatalyst and photoreactor [53]. The photocatalysts are divided into homogeneous and heterogeneous catalyst [54]. The process of conversion of CO_2 into fuels via solar irradiation is sustainable because of its renewability. Semiconductors are widely applied for heterogeneous photocatalytic reactions and metal oxides have often been used in water treatment or other valuable process. For example, methane is generated by photocatalytic CO_2 conversion catalyzed by various metal oxides such as $W_{18}O_{49}$ [55], HNb_3O_8 [56], Bi_2WO_6 [57], TiO_2 [58] and Zn_2GeO_4 [59]. When the CO_2 photoreduction is catalyzed by various metal oxides catalysts including $CuGaO_2$, $LiNbO_3$, $BiVO_4$, ZnO, TiO_2 and WO_3, different value-added products such as CO, formic acid, formaldehyde and ethanol were synthesized [60]. It is reported that ZnS was employed as catalyst for the production of methanol and methane from CO_2 because metal sulphide catalysts can achieve high yield own to its

promising solar energy absorption ability. In addition, metal phosphide semiconductors were widely utilized in the methanol production, but they require high potential for better yield. It is reported CO_2 is catalyzed by p-type GaP to produce methanol and the faradaic efficiency of 100% is observed [61]. When the metal is doped on semiconductor, it can provide the electron for the CO_2. For example, carbon doped TiO_2 was utilized as a catalyst to convert CO_2 into formic acid. Moreover, when the Dye-sensitized TiO_2 was loaded by 1% weight of Pt, the main product became to methane. Another emerging research area in the CO_2 reduction is to employ the quantum dot-sensitized photocatalyst. For instance, it is reported the highest CO_2 conversion rate was achieved by the PbS QDs sensitized Cu-TiO_2 catalyst [62]. In addition, phthalocyanine sensitized photocatalyst was also employed in CO_2 conversion process because its optimal chemical stability and semi-conductivity. The substrate based photocatalyst with high surface area has been utilized such as polyethylene terphthalate (PET) and polyethylene (PE) and the PET supported TiO_2 can transform CO_2 into CO under a light source [63]. The various value-added products produced through various CO_2 conversion pathways and the catalysts employed for the conversion process is summarized in the **Table 1.2.**

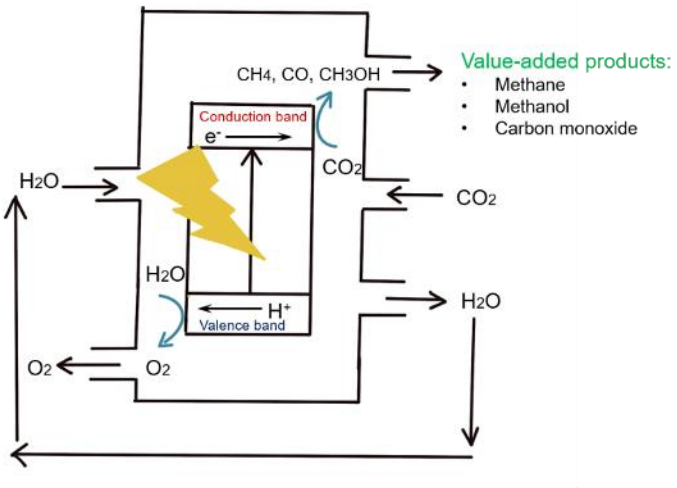

Figure 1.5. Photocatalytic CO_2 utilization and conversion.

Table 1.2. List of catalysts used for the production of valuable products through CO_2 utilization and conversion approaches.

No.	Catalysts	Products	Approaches	References
1	Sulfur modified copper	Formate	Electrochemical	(Chen et al., 2019a, 2019b)
2	Formate Dehydrogenase	Formate	Chemo-Enzymatic	(Reda et al., 2008)
3	Pd/HZSM-5	Dimethyl ether	Hydrogenation	(Chu et al., 2017)
4	Nitrogenase	Methane	Chemo-Enzymatic	(Yang et al., 2012)
5	Carbonic anhydrase	Bicarbonate (HCO_3^-)	Chemo-Enzymatic	(Yong et al., 2015)
6	$CuInS_2$ thin film	Methanol	Photoelectrochemical	(Yuan and Hao, 2013)
7	Indium	Acetate and Formate	Electrochemical	(Zha et al., 2020)
8	Nickel (Ni)	Methane	Thermal (Reforming)	(Zhang et al., 2020b)
9	TiO_2	Methane & Methanol	Photocatalytic	(Koci et al., 2009)
10	HNb_3O_8 nanobelt	Methane	Photocatalytic	(Li et al., 2012)
11	Bi_2WO_6 nanoplate	Methane	Photocatalytic	(Zhou et al., 2011)
12	Zn_2GeO_4 nanoribbon	Methane	Photocatalytic	(Liu et al., 2010)
13	$Cu/ZnO/Al_2O_3$	Carbon monoxide	Reverse water gas shift (RWGS)	(Zhuang et al., 2019)
14	ZnS	Methanol and Methane	Photocatalytic	(Koci et al., 2009)
15	p-type GaP	Methanol	Photoelectrochemical	(Barton et al., 2008)
16	PET supported TiO_2	Carbon monoxide	Photocatalytic	(Jensen et al., 2011)
17	Zeolite membrane	Methanol	Hydrogenation	(Raso et al., 2020)
18	CuZnZr/ferrierite hybrid	Dimethyl ether (DME)	Hydrogenation	(Sheng et al., 2020)
19	$RuCl_3$ xH_2O	Formate	Hydrogenation	(Jaleel et al., 2019)
20	Au/Al_2O_3	Formate	Hydrogenation	(Filonenko et al., 2016)

1.1.2.5 Electrochemical approach

It has been extensively reported in numerous publications the CO_2 is electrochemical reduced to generate different products, which can be driven by renewable energy/integrated into renewable energy system. In the research field of CO_2 conversion, electrocatalytic reduction seems to be the most feasible because it can be carried out under ambient conditions with a highly controllable reaction step and comparatively good conversion efficiency. Essentially, the electrochemical reduction of CO_2 in aqueous electrolyte is to transform CO_2 to carbon containing products including carbon monoxide (CO), methane (CH_4), formic acid (HCOOH), methanol (CH_3OH), ethylene (C_2H_4), ethanol (C_2H_3OH) by electron and proton transfer shown in **Figure**

1.5. The chemical equations for various products with their corresponding standard electrode potential [64] (V vs. RHE) are shown in **Table 1.3**. The CO_2 reduction products are diversified through different reaction pathways. As shown in the following equations (**Table 1.3**), the CO_2RR can conduct by two-, four-, six-, eight-, and twelve-electron transfer pathways in aqueous solution. **Table 1.3** lists the standard molar free energy of formation for different products and their corresponding standard electrode potentials. In detail, when the applied potential is sufficed, the reaction priority and reaction rate can also be affected remarkably by the electrolyte environment and the type of catalysts. Disparate metal catalysts possess different adsorption ability for the intermediates of CO_2 reduction (as denoted in the volcano plot for carbon dioxide reduction on metals (**Figure 1.6**). [65] From a general perspective, metal catalysts can be classified into four categories. (1) Pb, [66] In, [67] Sn [68,69] and Bi, [70,71] have weak binding energy to ECR intermediate products, in which the C-M (metal) bonds easily break and a large amount of formic acid is generated after the simple two electron transfer pathway. The second kind of catalyst, acting as an electron source, has poor adsorption with H*, leading to low competitive strength in hydrogen evolution reaction; (2) Au, [72] Ag, [73] Zn, [74] Pd [75,76] and Ga, [77] thought to have stronger combination with intermediates than (1), whilst have a weaker adsorption capacity for *H, results in there are not enough protons and the major products are CO by formula ③; (3) Cu [78-81] is the only particular metal which can produce C_{2+} compounds by multi electron reaction, which has moderate binding strength to the intermediates that can provide sufficient time for C-C dimerization and suppresses the hydrogen evolution reaction at the same time; (4) The C-M bond of Ni, Fe, Pt and Ti is too strong, which leads to heavy hydrogen evolution reaction. Except for metal catalysts, the two-dimensional transition metal carbide/nitride (MXene), [82-84] homogeneous catalyst including transition-metal complexes with organic ligands [85] and copper-based multinary sulfides (CMSs) [86] have been extensively reported and reviewed in the CO_2RR research area.

Table 1.3. Standard formation free energy and the related standard potential of different CO_2RR products in aqueous solution at 1.0 atm and 25 °C.

Substance	Chemical formula	Standard molar free energy of formation($\Delta_f G^{\ominus}m$) (kJ/mol)	Half-electrochemical CRR reactions	Electrode potentials (V vs. RHE)
Water (l)	H_2O	−237.129		
Carbon dioxide (g)	CO_2	−394.359		
Carbon monoxide (g)	CO	−137.168	$CO_2+2H^++2e^-\rightarrow CO+H_2O$	−0.104
Formic acid (l)	HCOOH	−361.350	$CO_2+2H^++2e^-\rightarrow HCOOH$	−0.171
Formaldehyde (g)	HCHO	−102.530	$CO_2+4H^++4e^-\rightarrow HCHO+H_2O$	−0.142
Methanol (l)	CH_3OH	−166.270	$CO_2+6H^++6e^-\rightarrow CH_3OH+H_2O$	0.016
Methane (g)	CH_4	−50.720	$CO_2+8H^++8e^-\rightarrow CH_4+2H_2O$	0.169
Ethylene (g)	C_2H_4	68.150	$2CO_2+12H^++12e^-\rightarrow CH_2CH_2+4H_2O$	0.079
Ethane (g)	C_2H_6	−32.820	$2CO_2+14H^++14e^-\rightarrow CH_3CH_3+4H_2O$	0.143
Ethanol (l)	CH_3CH_2OH	−168.490	$2CO_2+12H^++12e^-\rightarrow CH_3CH_2OH+3H_2O$	0.079

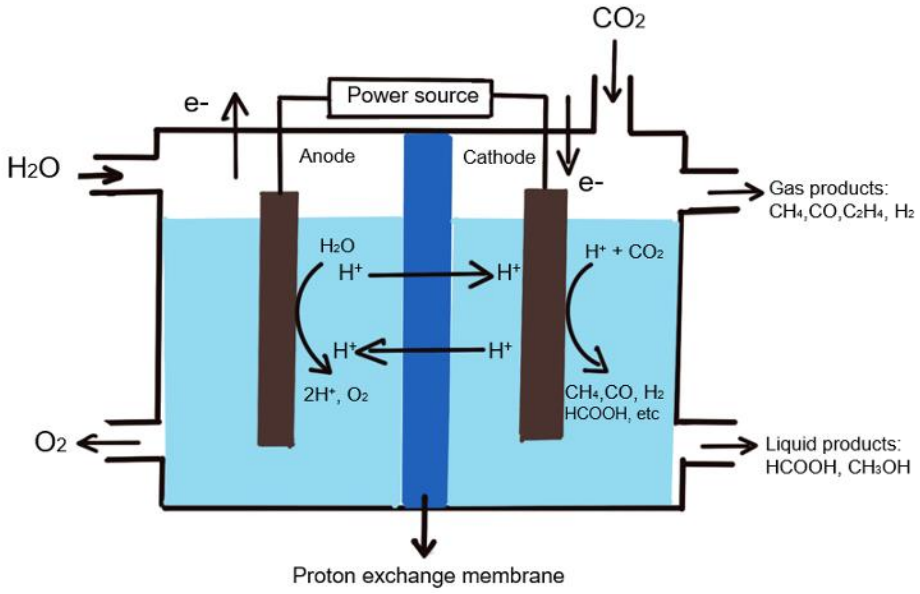

Figure 1.6. Electrochemical CO_2 utilization and conversion.

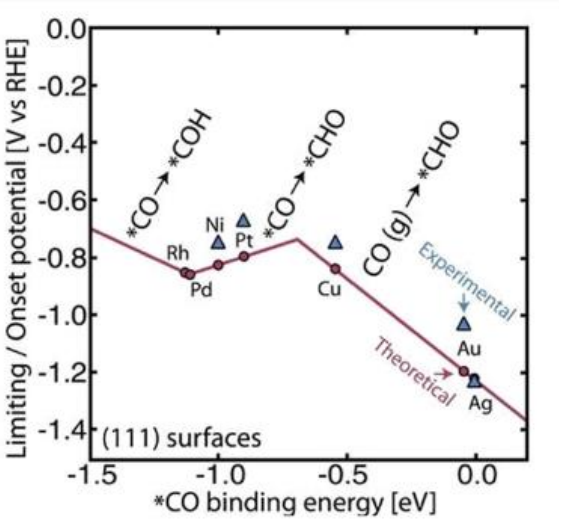

Figure 1.7 Volcano plot for carbon dioxide reduction on metals. [65] Copyright 2017, American Association for the Advancement of Science.

1.1.3 Motivation

As stated above, the more developed industry, the more serious environmental problems from CO_2 emission, which causes global warming issue. With a regard to contribute to solving these problems, the present study promotes an approach driven by renewable electricity to convert CO_2 into value-added products at atmospheric pressure and ambient temperature in terms of sustainable chemistry and carbon neutral. Moreover, the CO_2RR system still faces various issues and tough challenges at present, such as a low current density and poor selectivity for C_2 or C_{2+} products, mediocre stability, ultra-low CO_2 conversion and dismal energy efficiency, which remarkably limits its practical implementations in the future. This study is aimed to ameliorate the low current density and improve the selectivity of ethylene product.

1.1.4 Research objectives

The overall goal of the present research is to improve the current density as well as electrocatalytic activity of metal oxide based (including $La_2O_2CO_3$ and CuO) composite catalysts. The metal oxide electrocatalysts were first chose based on the following points:

- Reduce CO_2 at low overpotentials.
- Selective or efficient catalysts.
- Non-toxicity and low cost.

The study is focus on the preparation of single phase of $La_2O_2CO_3$, macroporous $ZnO/La_2O_2CO_3$ composites, $Copper/La_2O_2CO_3$ and Copper/C composites. The modification of catalysts helps to improve CO_2 electroreduction activity.

1.2. Outline of dissertation

This research focuses on the development of La-based and Cu-based electrocatalyst and their application in CO_2 electroreduction. The structure of this dissertation contains three main parts as followed:

- *Part I. Overview of dissertation*

Chapter 1 presents of CO_2 emission, its influence to the environment, the different approaches of CO_2 utilization followed by introduction of basic mechanism of electrocatalysis in aqueous media. The objectives and overview of the dissertation are presented. The next part in this chapter gives an introduction of Lanthanum Oxycarbonate, Copper oxide, Carbon support and their role in the electroreduction. Here also present drawbacks of this material and review some methods to overcome those disadvantages.

- *Part II. Improvement the $La_2O_2CO_3$ catalyst by introducing ZnO*

Chapter 2 introduces $La_2O_2CO_3$ as an electrocatalyst because of its promising adsorption ability of CO_2. Herein, the hexagonal and monoclinic phases of $La_2O_2CO_3$ nanoparticles were synthesized by different wet preparation methods and their phase-related CO_2 behavior were investigated.

Chapter 3 promotes two methods for preparing $La_2O_2CO_3$/ZnO electrocatalyst with different morphology. With the addition of Zinc, the selectivity of CO can be improved, result in

the dominant products of $ZnO/La_2O_2CO_3$ are CO. Moreover, we observed there is C_2H_4 generated by macroporous $ZnO/La_2O_2CO_3$ catalyst.

- *Part III. The catalytic performance improvement of copper-based catalysts*

Chapter 4 Copper supported by $La_2O_2CO_3$ series catalysts were well prepared by hydrothermal method and the main phase of copper was converted from CuO to $Cu_2(OH)_3Cl$ with the increasing content of copper precursor. The EL-Cu-2 sample shows the highest BET surface and show the best activity towards CO_2RR with its highest FE_{C2H4}= 25%.

Chapter 5 is a modification of copper-based catalyst by supporting by carbon. The BET surface area in the following order: AC-Cu > GO-Cu > CNT- Cu > CSs- Cu which is consist with the CO_2RR catalytic performance. The highest FE_{C2H4}= 50.8 % of CuO/C was achieved by AC-Cu possibly own to its highest surface area and lowest impedance. From the ex-situ surface analysis by XRD, XPS, and XANES, it was found that C_2H_4 production was favored on the catalysts containing mixed oxidized copper species along with high oxygen content.

Figure 1.8. The main structure of dissertation.

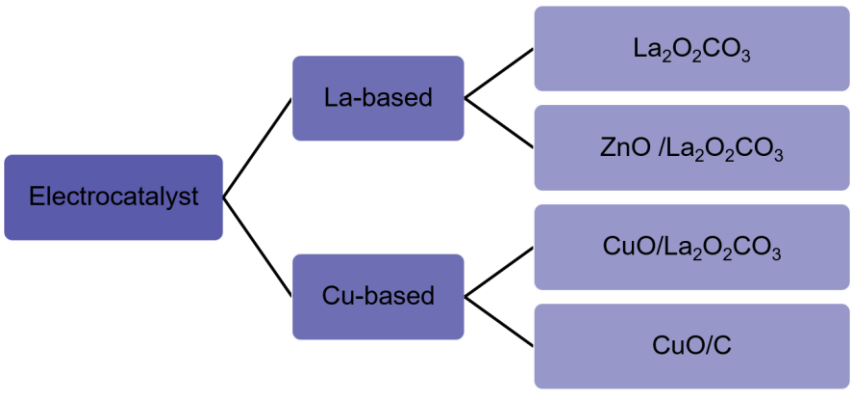

1.3. Introduction of materials

1.3.1. Metal oxides

1.3.1.1. Lanthanum Dioxide Carbonate（$La_2O_2CO_3$)

Lanthanum (La_2O_3) has been widely used as a promoter or support in heterogeneous catalysis [87–89]. The basicity of La_2O_3 readily induces the adsorption of CO_2 to form the lanthanum oxycarbonate ($La_2O_2CO_3$) phase, which is an important species in the La_2O_3-containing catalytic reaction [90-93]. The crystalline structures of $La_2O_2CO_3$ can be divided into three types of different polymorphs: a tetragonal $La_2O_2CO_3$ (type I), a monoclinic $La_2O_2CO_3$ (type Ia), and a hexagonal $La_2O_2CO_3$ (type II) [94–96]. The hexagonal type II $La_2O_2CO_3$ has a higher chemical stability to water and carbon dioxide than the monoclinic type Ia [90,97,98]. In addition, the different crystalline structures of the $La_2O_2CO_3$ phases affect the interaction between $La_2O_2CO_3$ and ZnO in the $La_2O_2CO_3$/ZnO composite materials as well as the catalytic behavior of the composite materials on glycerol carbonation with CO_2 [90,99]. Meanwhile, the monoclinic type Ia $La_2O_2CO_3$ phase closely resembles the crystalline structure of lanthanum (La) oxysalts (e.g., oxysilicates, oxyhalides, and oxysulfates), whereas the hexagonal type II one is similar to A-type La sesquioxides.

1.3.1.2. Brief introduction of Cu-based electrocatalyst

Cu-based catalyst has unique properties among metal catalysts and has been considered as an ideal material for electrocatalytic reduction of CO_2 to polycarbonate. From the point of reaction kinetics, the dimerization reaction of intermediate (*CO) needs to overcome a high potential barrier. However, before the dimerization reaction, *CO tends to desorb and release C_1 product or the excessive adsorbed *H leads to the hydrogen evolution reaction. Hori et al. carried out a series of studies [100–102] and found that CO_2 can be reduced to ethylene and other C_2 products on copper catalysts, which broke new ground for metal catalysts to obtain C_{2+} products in ECR.[100] Since then, researchers have devoted to developing new Cu-based catalysts with lower over potential, larger current density, and higher selectivity, so as to convert CO_2 into ethylene, ethanol, ethane and other C_2 products, even C_3 and C_4 products.

1.3.2. Carbon-based catalyst

Carbon electrodes, such as glassy carbon electrodes (GCE), boron doped-diamond (BDD), graphite, graphene, carbon black, carbon nanotubes (CNTs), and carbon fiber, have been widely used for the electrochemical application, such as electrochemical sensor and electrocatalysis [103,104]. The carbon electrode has distinct properties compared to the metal-based ones, such as extensive lifetime for electrochemical application, relatively low-cost, wider potential window, and controllable surface modification [105,106]. Ramli et al. [107] stated that carbon as a support electrode might affect the catalyst by improving the mass transfer, conductivity, active surface area, and even the metal stability decorated on the surface of the carbon-based electrode. Various carbon-based electrodes, such as CNTs, GCE, and BDD, have been used to support metal NPs for CO_2 electrochemical reduction. As previously reported, CO_2 electrochemical reduction was widely performed on a bulk surface of metal electrodes [101] which were known to have a high catalytic activity to support the high overpotential of CO_2 reduction.

PART II – IMPROVEMENT OF LANTHANUM DIOXIDE CARBONATE BY INTRODUCING METALS

Chapter 2. $La_2O_2CO_3$ electrocatalyst

2.1. Introduction

Recently, the synthesis of nanomaterials with controllable morphologies and phases has attracted considerable attention in the fields of materials science and inorganic chemistry because the physicochemical and structural properties of the nanomaterials strongly correlate with the types of crystal structures as well as the morphologies of nanoparticles [90,108-112]. The unique properties of nanomaterials can be properly tuned by controlling various factors, which results in potential applications of nanomaterials in catalysis, biological labeling, sensing, and optics [108,113-115]. Among the methods for synthesizing nanomaterials, wet chemical processes have been considered as the most effective and convenient approaches for the controllable phases of ceramic materials [116].

Lanthana (La_2O_3) has been widely used as a promoter or support in heterogeneous catalysis [87–89]. The basicity of La_2O_3 readily induces the adsorption of CO_2 to form the lanthanum oxycarbonate ($La_2O_2CO_3$) phase, which is an important species in the La_2O_3-containing catalytic reaction [90-93]. The crystalline structures of $La_2O_2CO_3$ can be divided into three types of different polymorphs: a tetragonal $La_2O_2CO_3$ (type I), a monoclinic $La_2O_2CO_3$ (type Ia), and a hexagonal $La_2O_2CO_3$ (type II) [94–96]. The hexagonal type II $La_2O_2CO_3$ has a higher chemical stability to water and carbon dioxide than the monoclinic type Ia [90,97,98]. In addition, the different crystalline structures of the $La_2O_2CO_3$ phases affect the interaction between $La_2O_2CO_3$ and ZnO in the $La_2O_2CO_3$/ZnO composite materials as well as the catalytic behavior of the composite materials on glycerol carbonation with CO_2 [90,99]. Meanwhile, the monoclinic type Ia $La_2O_2CO_3$ phase closely resembles the crystalline structure of lanthanum (La) oxysalts

(e.g., oxysilicates, oxyhalides, and oxysulfates), whereas the hexagonal type II one is similar to A-type La sesquioxides. Thus, the type Ia $La_2O_2CO_3$ phase has been readily prepared by the thermal decomposition of La compounds (e.g., oxalates and acetates); however, it is difficult to prepare type II $La_2O_2CO_3$ in a single phase by the conventional wet preparation methods [117]. Accordingly, it is necessary to investigate i) the preparation conditions used to form type Ia and type II $La_2O_2CO_3$ phases in the conventional methods and ii) the CO_2 behavior on the $La_2O_2CO_3$ structures, which is an essential step in the CO_2-involving catalytic reactions, as well as the formation of the different $La_2O_2CO_3$ phases.

In this study, we prepared the nanoparticles with type Ia and type II $La_2O_2CO_3$ crystal structures by conventional wet preparation methods and investigated the formation of different $La_2O_2CO_3$ phases with Fourier transform infrared (FT-IR), X-ray diffraction (XRD), field-emission scanning electron microscopy (FE-SEM), and high-resolution transmission electron microscopy (HR-TEM). Furthermore, the CO_2 behavior on the different $La_2O_2CO_3$ crystal structures was observed by CO_2-temperature programmed desorption (TPD), thermogravimetric analysis (TGA), and linear sweeping voltammetry (LSV) of CO_2 electrochemical reduction. The superior CO_2 behavior of the hexagonal $La_2O_2CO_3$ phase to the monoclinic phase was additionally explained by the crystalline structures of both $La_2O_2CO_3$ phases, which was predicted by the density functional theory (DFT) calculation.

2.2. Materials and analysis technologies

2.2.1. Preparation procedures

A total of 1.00 g of $La(NO_3)_3 \cdot 6H_2O$ was added to 50.0 mL of deionized water, and the resultant solution was vigorously stirred to ensure complete dissolution. The pH of the solution was adjusted to 12 with a 10 wt % NaOH solution, which yielded a white precipitate after the mixture was stirred for approximately 10 min. The sample was continuously stirred for another 6, 12, or 24 h, and the obtained product was centrifuged. The separated precipitate was washed with distilled water and ethanol and then dried at 80 °C for 12 h, followed by the calcination step

at 500 °C for 2 h. Depending on the precipitation time, the solid samples prepared by the precipitation method were denoted as PL-*x*h (*x* = 6, 12, or 24), where *x* represents the precipitation time.

For the hydrothermal method, the procedure was almost the same as that in the precipitation method, except using an autoclave for the hydrothermal treatment. The pH-adjusted solution containing the La precursor was transferred to an autoclave (200 mL), heated to 160 °C, and maintained at this temperature for 6, 12, or 24 h. The obtained product was centrifuged, and the remained steps were also the same as those in the precipitation method. The $La_2O_2CO_3$ samples synthesized by the hydrothermal method were designated as HL-*y*h (*y* = 6, 12, or 24), where *y* represents the hydrothermal treatment time.

2.2.2. Characterization techniques

The morphologies of the samples were observed by a field-emission scanning electron microscope (JEOL, JSM-600F, Tokyo, Japan) instrument equipped with an energy-dispersive spectrometer. HR-TEM images were obtained using a JEOL JEM-2100F instrument (JEOL Ltd., Tokyo, Japan). The samples were prepared by suspending and grinding in an ethanol solution whose drops were placed on a carbon-film-coated copper grid. XRD patterns were measured at room temperature on a Rigaku D/MAX-2200 powder X-ray diffractometer (Rigaku Corporation, Tokyo, Japan) using a Cu Kα radiation source (λ = 0.15418 nm). The X-ray tube was operated at 35 kV and 20 mA, and the 2θ angle was scanned from 10° to 90° (with a step of 0.02°) at a speed of 2°/min. The FT-IR spectra of the samples were collected for the KBr powder-pressed pellets on a Nicolet 380 FT-IR spectrophotometer (Thermo Fisher Scientific, Waltham, MA, USA) under ambient conditions. The CO_2-TPD experiments were conducted in a quartz flow reactor. The calcined samples were preheated from room temperature up to 600 °C (with a ramping rate of 15°C/min) for 1 h under He flow (100 mL/min). The CO_2 gas (10 vol.% CO_2/He) was fed into the reactor with a flow rate of 30 mL/min at 50 °C for CO_2 adsorption before

conducting the CO_2-TPD measurements. Finally, the temperature was increased from 50 to 600 °C at the ramping rate of 1.5 °C/min in He flow (30 mL/min). The weight loss in the samples was determined by a thermogravimetric analyzer (TA Instruments Q50, New Castle, DE, USA). A total of 20 mg of the samples was charged into the sample pan and heated to 1000 °C at a rate of 5 °C /min in air flow.

2.2.3. Electrocatalytic performance

The CO_2 electrochemical reduction was carried out via the LSV measurement with an Ag/AgCl electrode as a reference electrode and Pt wire as a counter electrode. The working electrode was prepared by dispersing 10 mg of the samples in a mixture of 2 mL of alcohol and 100 µL of 5% Nafion and then pipetting 10 µL of suspension on the GCE (0.07065 cm^2). The working electrode was tested 20 times at a scan rate of 20 mV/s. The electrolyte was 0.1 M $NaHCO_3$ saturated with CO_2. Before each experiment, high-purity CO_2 gas was bubbled at a flow rate of 30 mL/min for 30 min to remove all oxygen from the electrolyte. The generated gaseous products (H_2, CO, CH_4, and C_2H_4) of CO_2RR were analyzed by a gas chromatograph (GC9800, Kechunang, equipped with a thermal conductivity detector and a flame ionization detector.

2.2.4. DFT calculation

Using the Vienna Ab initio Simulation Package (VASP) [118,119], DFT calculatimons were conducted along with the GGA–PBE (Perdew–Burke–Ernzerhof) functional [120]. The cutoff energy of 600 eV was chosen in our calculations. The criteria of convergence of energies and forces for geometry optimization were 10−4 eV and 10−2 eV/Å, respectively. For the calculation of disordered hexagonal $La_2O_2CO_3$, the lowest energy configuration among the other randomly selected 50 structures was used. The Monkhorst-Pack *k*-point meshes of 3 × 5 × 2 and 9 × 9 × 3 were used for the geometry optimization of monoclinic and hexagonal phase of $La_2O_2CO_3$, respectively [121].

2.3. Results and discussions

2.3.1. Synthesis of Monoclinic and Hexagonal $La_2O_2CO_3$ Nanoparticles

Figure 2.1 shows the XRD patterns of $La_2O_2CO_3$ nanoparticle materials prepared at each reaction time. The two types of $La_2O_2CO_3$ phases are primarily detected in the PL samples: the monoclinic type Ia and hexagonal type II $La_2O_2CO_3$ phases. For 6 h of precipitation (PL-6h), the characteristic XRD peaks in the hexagonal $La_2O_2CO_3$ crystal phase are clearly observed at 2θ = 25.7, 30.2, 47.2, and 56.6° (JCPDS 37-0804) (**Figure 2.1 (Aa)**) [108,90,98,99,122,123]. However, when the precipitation time is increased to 12 and 24 h, the characteristic XRD peaks in the monoclinic $La_2O_2CO_3$ phase clearly appear at 2θ = 22.8, 29.3, 31.0, 39.9, and 44.4° with a C12/C1 space group (JCPDS 48-1113) (**Figure 2.1 (Ab, Ac)**), which indicates the prevalence of the hexagonal $La_2O_2CO_3$ phase during the initial precipitation time, followed by the transformation into the monoclinic $La_2O_2CO_3$ phase after 12 h of precipitation. In contrast, the HL samples show the XRD patterns that contain the characteristic peaks in only the hexagonal type II $La_2O_2CO_3$ phase, regardless of the reaction time during the hydrothermal preparation, which demonstrates that there is no change in the $La_2O_2CO_3$ phase during the preparation process (**Figure 2.1 (Ba–Bc)**).

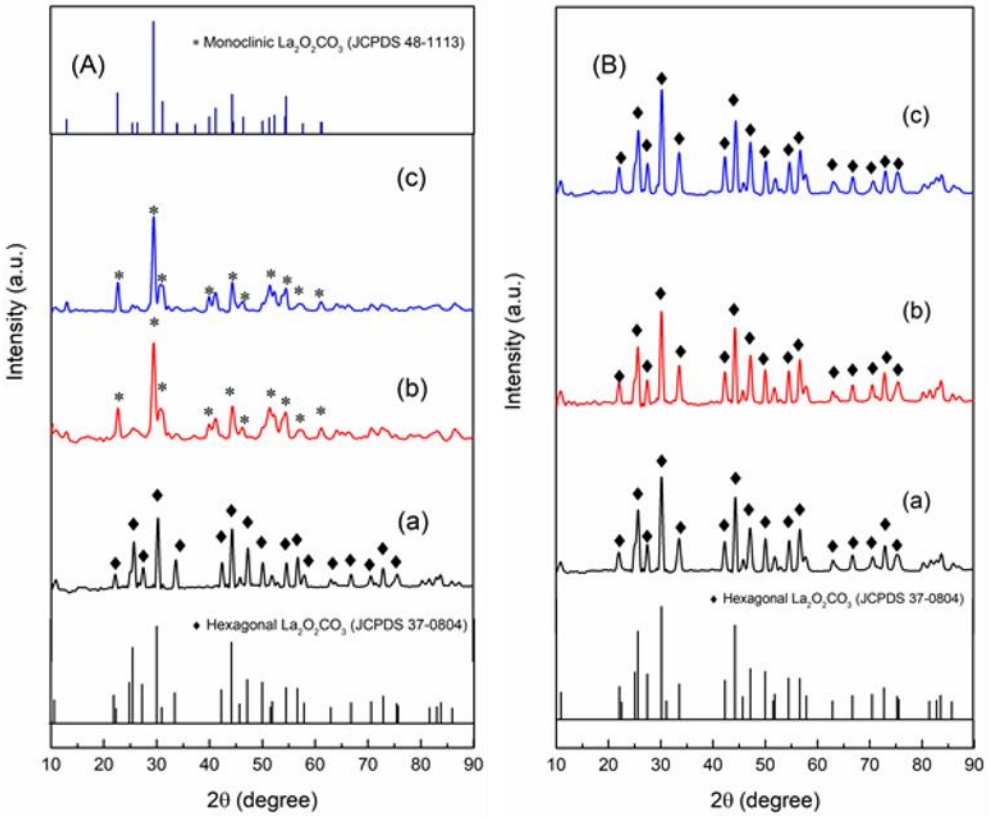

Figure 2.1. XRD patterns of A(a-c) PL-6h, PL-12h, and PL-24h and B(a-c) HL-6h, HL 12h, and HL-24h.

The FT-IR spectra of the PL and HL samples also confirm the formation of each $La_2O_2CO_3$ crystal phase depending on the preparation methods, as shown in **Figure 2.2**. According to the assignments of typical FT-IR bands for carbonates in the $La_2O_2CO_3$ phases, the bands at 745, 855, 1066, and 1518 cm^{-1} are interpreted as CO_3^{2-} vibrations related to the $La_2O_2CO_3$ phase. The three-fold splitting bands at approximately 845 cm^{-1} (υ2) and a strong band at 1367 cm^{-1} (υ3) are assigned to the unique carbonate vibrational mode for the monoclinic type Ia $La_2O_2CO_3$ phase [90,112,99,118]. The FT-IR spectra in Figure 2.2**(b)** and **(c)** of only the PL-12h and PL-24h samples show the characteristic bands (υ2 and υ3) of type Ia $La_2O_2CO_3$, whereas the FT-IR spectra of the other samples show the typical bands of the $La_2O_2CO_3$ phase, which further confirms that the formation of the type Ia and II $La_2O_2CO_3$ phases depends on the preparation

conditions. In the precipitation method, the monoclinic type Ia $La_2O_2CO_3$ phase is mainly formed when the precipitation time is longer than 12 h, whereas the hydrothermal method produces only the hexagonal type II $La_2O_2CO_3$ phase. This is consistent with the XRD results in this study.

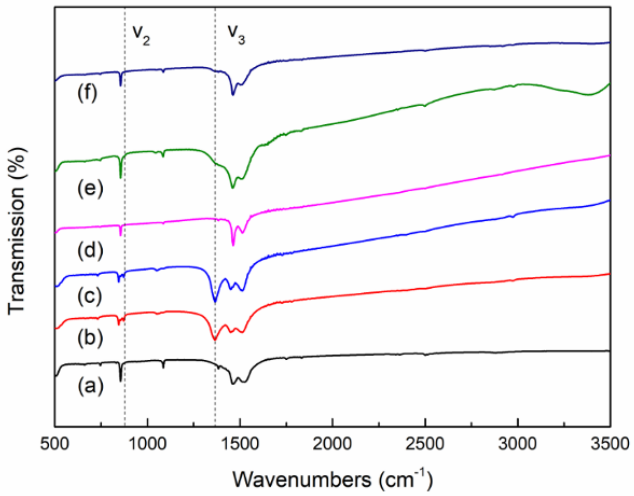

Figure 2.2. FT-IR spectra of (a) PL-6h, (b) PL-12h, (c) PL-24h, (d) HL-6h, (e) HL-12h, and (f) HL-24h.

Moreover, TEM measurements also provide additional evidence for the existence of the monoclinic and hexagonal $La_2O_2CO_3$ phases in the samples. **Figure 2.3 (a–c)** show the TEM images and fast Fourier transform patterns of PL-6h, PL-12h, and HL-12h. The (207) plane of the monoclinic type Ia $La_2O_2CO_3$ phase is detected in the PL-12h sample whereas the (260) plane of the hexagonal type II $La_2O_2CO_3$ phase is observed in the HL-12h sample. Similarly, the PL-6h sample shows the (004) plane of the type II $La_2O_2CO_3$ phase, which is in good agreement with the XRD and FT-IR data. However, the morphological structures of PL-12h, HL-12h, and PL-6h samples are similar, as shown by the FE-SEM images; the aggregates of nanoparticles have different sizes: smaller than 10 nm for PL-12h, 10–30 nm for HL-12h, and 30–60 nm for PL-6h [**Figure 2.3 (d–f)**].

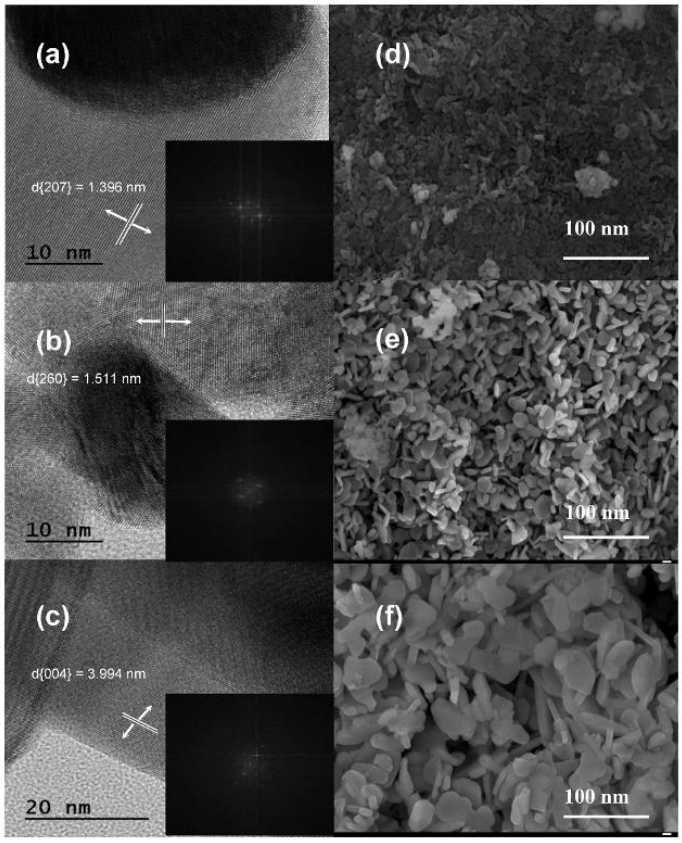

Figure 2.3. High-resolution transmission electon microscopy (HR-TEM) images of (a–c) PL-12h, HL-12h, and PL-6h, and FE-SEM images of (d–f) PL-12h, HL-12h, and PL-6h. The insets of (a–c) show their fast Fourier transform patterns.

To further understand the formation mechanism of the monoclinic and hexagonal $La_2O_2CO_3$ phases, uncalcined samples after precipitation or hydrothermal treatment were investigated. The XRD and FT-IR measurements indicate that different chemical products are also produced depending on the preparation conditions (**Figure 2.4**). The XRD peaks in **Figure 2.4(Aa–Ac)**, shown as circles, are indexed to the pure hexagonal phase of $La(OH)_3$ with a P63/m(176) space group (JCPDS 36-1481) [108,112,89,99,122,123,124], which clearly shows that the initial $La(OH)_3$ phase remains unchanged in the hydrothermal method. With an increase in the preparation time during the hydrothermal method, the crystallinity of the $La(OH)_3$ structure becomes stronger with sharper XRD characteristic peaks. Meanwhile, in the precipitation method, the $La(OH)_3$ phase is produced with a very low crystallinity for PL-6h (weak and broad

characteristic XRD peaks in **Figure 2.4(Ac)**). However, when the precipitation time is increased up to 12 h, the characteristic XRD peaks assigned to the orthorhombic $La(OH)CO_3$ structure (JCPDS 49-0981) appear with the disappearance of the XRD peaks in the $La(OH)_3$ structure (**Figure 2.4(Ad)**)[115,125]. Therefore, in the precipitation method, the dominant phase evolves from $La(OH)_3$ to $La(OH)CO_3$, with an increase in the precipitation time. However, the initial $La(OH)_3$ phase in the hydrothermal method is more crystallized during the hydrothermal treatment.

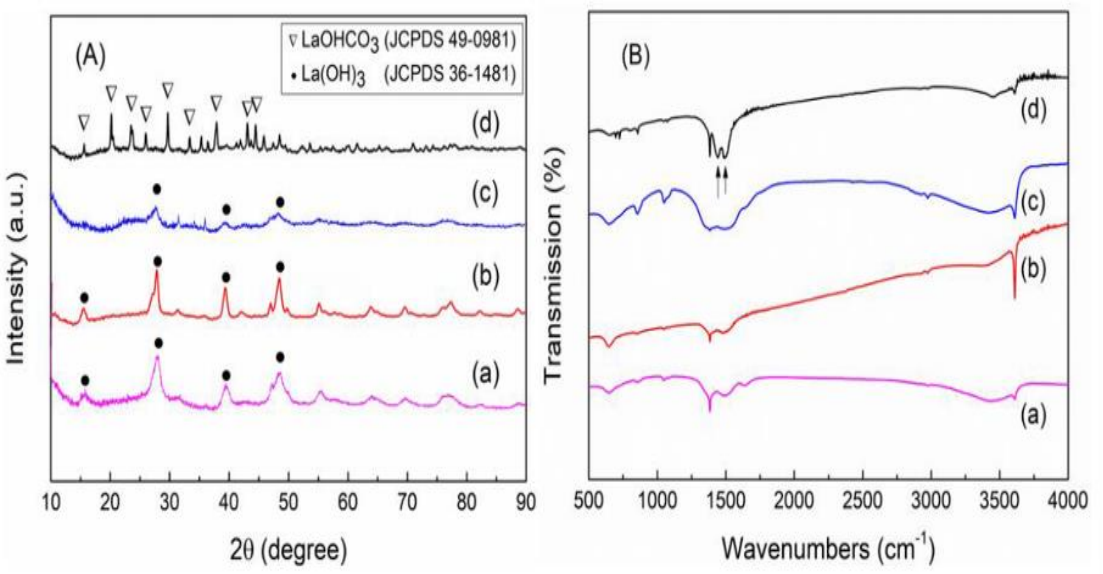

Figure 2.4. (A) XRD patterns and (B) FT-IR spectra of uncalcined samples. (a) HL-6h, (b) HL-12h, (c) PL-6h, and (d) PL-12h.

The FT-IR spectra of the uncalcined samples are monitored to confirm the existence of $La(OH)_3$ and $La(OH)CO_3$. First, the strong bands at 1438 and 1491 cm−1 shown in **Figure 2.4 (Bd)** can be assigned to the bending vibrations of CO_3^{2-}, which confirms the presence of carbonate species in the intermediate [115]. A band at 3616 cm^{-1} and a broad band at 3410 cm^{-1} represent the O–H stretching mode in La–OH [112,115,123]. The bands at 850 and 1052 cm^{-1} correspond to the vibrational modes of carbon-related bonds, such as CH and CO, which

remain before the calcination step. Thus, the FT-IR spectrum in **Figure 2.4(Bd)** clearly confirms the existence of $La(OH)CO_3$ as an intermediate in the PL-12h sample, which is consistent with the XRD data shown in **Figure 2.4A**. For $La(OH)_3$, the characteristic FT-IR bands for the O–H stretching and bending modes in La–OH are clearly observed at 3616, 3410, and 1640 cm^{-1}, as shown in **Figure 2.4(Ba–Bc)** [112,115,123]. Other bands at approximately 2800–3000, 850, and 1052 cm^{-1} can also be assigned to the vibrational modes of carbon-related bonds. Interestingly, for the samples in the precipitation method, the characteristic IR bands for CO_3^{2-} at approximately 1350–1500 cm^{-1} become sharp and strong with an increase in the reaction time (**Figure 2.4(Bc, Bd)**), whereas the characteristic IR band for OH at 3616 cm^{-1} is strongly intensified during the hydrothermal method (**Figure 2.4(Ba, Bb)**). Therefore, the precipitation method induces the transformation from $La(OH)_3$ into $La(OH)CO_3$ through the reaction with CO_2. In the hydrothermal method, the crystallization of $La(OH)_3$ goes further, which results in the high crystallinity of $La(OH)_3$.

A critical difference between the two preparations is an open or closed reaction system, which is related to the supply of carbonate sources. For either the precipitation or hydrothermal method, the La precursor in the aqueous solution is dissociated into La cations and is then readily crystallized into the $La(OH)_3$ phase, because the initial pH conditions are strongly basic (i.e., pH = 12). In the hydrothermal method, a Teflon-lined autoclave reactor is used as a closed reaction system. Because it is a closed system, there is no further transformation of the La intermediate, which only results in the strong crystallization of the $La(OH)_3$ phase for the HL-12h and HL-24h samples. However, in the precipitation method, the precipitation is carried out in an open beaker; thus, the carbonate source (i.e., CO_2 from the air) can be continuously dissolved into the aqueous solution. Therefore, the initial phase, $La(OH)_3$, can be converted into the $La(OH)CO_3$ phase by the reaction with CO_2 at a time longer than 12 h, even though the 6-h precipitation produces only a weakly crystallized $La(OH)_3$. Under the continuous CO_2 supply condition, there is a transformation from $La(OH)_3$ into $La(OH)CO_3$. In the literature, it was reported that

$La(OH)_3$ changed into an La carbonate when it was exposed to air [112,123,124]. More importantly, the $La(OH)CO_3$ phase is finally converted into the monoclinic type Ia $La_2O_2CO_3$ phase in the precipitation, while $La(OH)_3$ is transformed into the hexagonal type II structure in the hydrothermal method. The sufficient supply of CO_2 into the aqueous solution produces the $La(OH)CO_3$ that can be changed into the monoclinic $La_2O_2CO_3$ phase.

2.3.2. CO_2 Behavior on $La_2O_2CO_3$ Nanoparticles

To investigate the CO_2 behavior on each $La_2O_2CO_3$ phase, TGA, CO_2-TPD and CV of CO_2 electrochemical reduction for PL-12h (monoclinic type Ia $La_2O_2CO_3$ phase) and HL-12h (hexagonal type II $La_2O_2CO_3$ phase) were conducted in this study. **Figure 2.5A** shows the derivative TGA (DTGA) profiles of PL-12h and HL-12h, where the decomposition peaks correspond to CO_2 gases that leave from the $La_2O_2CO_3$ phases. The weight loss due to the thermal decomposition occurs at 326 °C and in the temperature range of 770–800 °C. According to previous studies [90,30], the CO_2 peak, which appears during the decomposition of $La_2O_2CO_3$ above 600 °C, can be assigned to CO_2 gases leaving from the bulk structure of the $La_2O_2CO_3$ phases, which is then transformed into the La_2O_3 phase. The CO_2 decomposition from the bulk structure of the hexagonal $La_2O_2CO_3$ phase occurs at approximately 800 °C, which is higher than the temperature of CO_2 production during the decomposition of the bulk structure of the monoclinic $La_2O_2CO_3$ phase. This result shows that the thermal stability of the hexagonal $La_2O_2CO_3$ phase is higher than that of the monoclinic phase [99]. The weight loss at approximately 326 °C is assumed to be due to the release of CO_2 gas that is adsorbed on the surface of the $La_2O_2CO_3$ phase. The decomposition peak at approximately 326 °C has a much smaller intensity than that at 650 °C, which indicates that a much lower amount of CO_2 is adsorbed onto the surfaces of the $La_2O_2CO_3$ phase than that released from the bulk structure. Furthermore, based on each peak's intensity, shown in **Figure 2.5A**, the hexagonal type II $La_2O_2CO_3$ phase contains more CO_2 on the surface than that on the monoclinic type Ia phase.

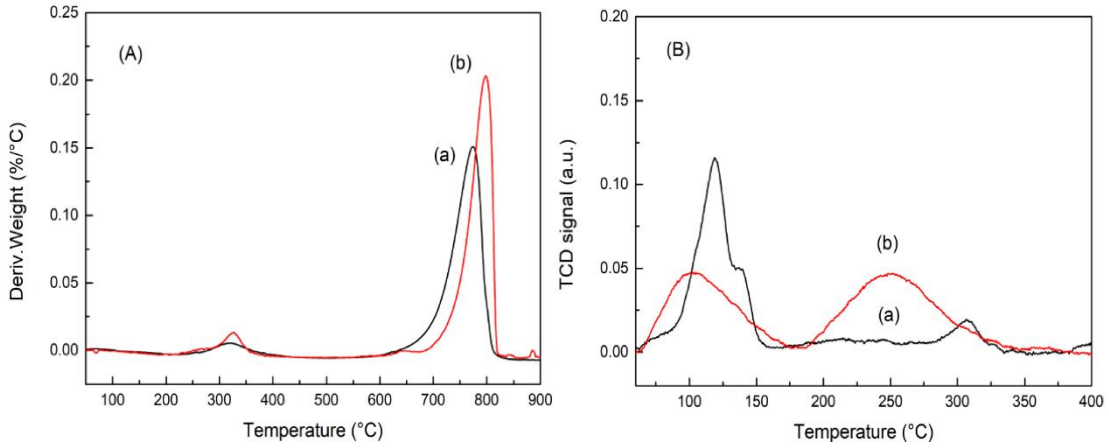

Figure 2.5. (A) Derivative thermogravimetric analysis (TGA) profiles and (B) CO_2-tempurate-programmed desorption (TPD) patterns of (a) PL-12h and (b) HL-12h.

To better understand the CO_2 adsorption ability on the surface of each $La_2O_2CO_3$ phase, the CO_2-TPD profiles of PL-12h and HL-12h were acquired. Before conducting the CO_2-TPD experiments, both samples were thermally treated at 600 °C for 1 h in He gas, and then CO_2 was introduced into the reactor at 50 °C to perform the CO_2 adsorption. Therefore, CO_2 can be assumed to adsorb on the surface of $La_2O_2CO_3$ phases and then desorb from the adsorption surface sites, which demonstrates the CO_2 adsorption behavior on the monoclinic and hexagonal $La_2O_2CO_3$ phases. In **Figure 2.5B**, the CO_2 desorption peaks can be approximately categorized into three types. The peak at approximately 100 °C is related to a weak basic site, and the peaks in the range of 200–400 °C correspond to medium and strong basic sites [109,89,133,129]. The CO_2 adsorption modes on each basic site have been studied by a combination of FT-IR spectroscopy and CO_2-TPD measurements [133,129]. Manoilova et al. [132] investigated the CO_2 adsorption onto La_2O_3 by IR spectroscopy, TPD, and DFT calculations. The DFT calculation for the CO_2 adsorption on La_2O_3 predicted that CO_2 gas adsorbed on the surface in the form of polydentate and monodentate species as a starting structure, and then La_2O_3 made a stable connection with polydentate and asymmetric CO_2 adsorptions at the saturated coverage. The CO_2 desorption peak at approximately 290 °C in the CO_2-TPD profile of LaOCl was

assigned to the decomposition of coupled bridged CO_2 adsorbate species [133]. On the basis of the results from the FT-IR and CO_2-TPD measurements of Mg–Al basic oxides, Di Cosimo et al. [126] suggested that the three types of CO_2 adsorption modes (e.g., bicarbonate, bidentate carbonate, and unidentate carbonate) were low-strength, medium-strength, and high-strength basic sites, respectively. It was determined that bidentate and unidentate carbonates remained on the surface at approximately 300 °C; only unidentate carbonate was detected at 350 °C [129]. Therefore, in this study, the peak at 110 °C, peaks at approximately 240 °C, and shoulders at approximately 310 °C can be assigned to the desorption of CO_2 species adsorbed on weak, medium and strong basic sites, respectively**. Figure 2.5B** and **Table 2.1** shows that the HL-12h sample has a higher combined intensity of medium and strong basic sites than PL-12h, which suggests that the hexagonal type II $La_2O_2CO_3$ phase provides more CO_2 adsorption sites on the surface. This observation is in good agreement with the TGA results shown in **Figure 2.5A**.

Table 2.1. The peak intensities quantified in the CO_2-TPD patterns.

Samples	Temperature at maximum (°C)	Quantity (cm^3/g STP)
PL-12h	119	31.7
	306	3.38
HL-12h	109	24.6
	241	29.0

A DFT calculation was performed to optimize the bulk structures of both $La_2O_2CO_3$ phases (**Figure 2.6**). The lattice constant of $La_2O_2CO_3$ in the disordered hexagonal structure was predicted by considering the ratio (c/a) of lattice parameters (a and c) of the hexagonal structure [126]. Our DFT calculated lattice constants of $La_2O_2CO_3$ nanoparticles in both monoclinic and hexagonal structures, similar to the available experimental data from the literature, which are shown in **Table 2.2**[127,128]. On the basis of the DFT calculation, we can optimize the hexagonal type II and monoclinic type Ia $La_2O_2CO_3$ nanopartilces, as shown in

Figure 2.7 From the optimized structure of each phase, the La atom is determined to have seven and eight oxygen atoms as nearest neighbors in monoclinic and hexagonal structures, respectively. The eight coordination numbers of the La atom in the hexagonal type II $La_2O_2CO_3$ nanoparticles can produce stronger bonding with carbonate species, which results in the higher stability of the hexagonal type II structure compared to that of the monoclinic type Ia $La_2O_2CO_3$.

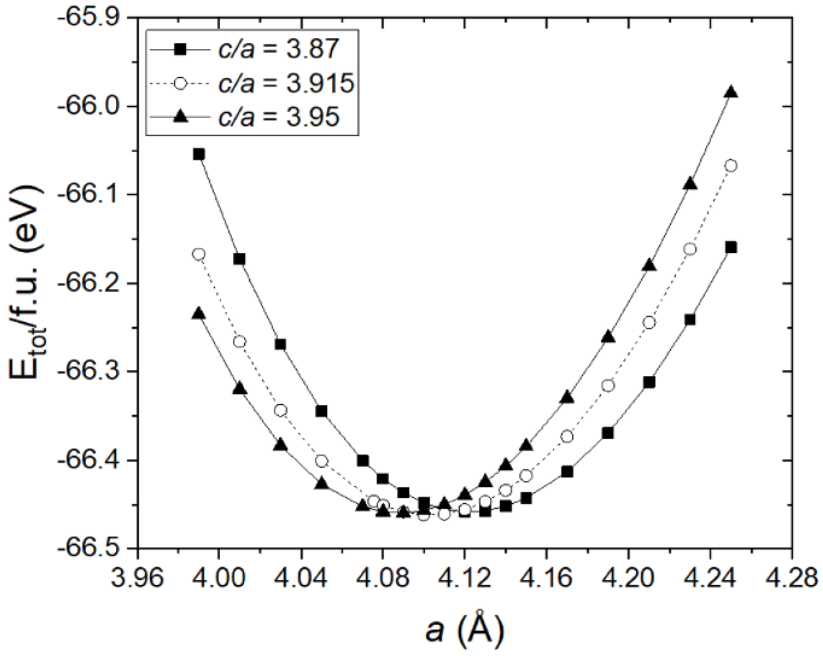

Figure 2.6. Density functional theory (DFT) total energy (per formula unit) of $La_2O_2CO_3$ in the hexagonal structure for three c/a values.

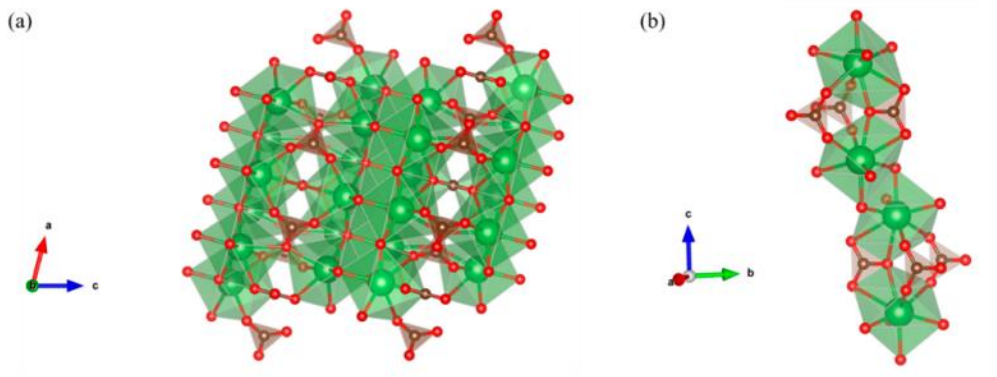

Figure 2.7. DFT-optimized structure of $La_2O_2CO_3$ in (a) monoclinic and (b) hexagonal phases.

Table 2.2 . Lattice constants of $La_2O_2CO_3$ in monoclinic and hexagonal structures. The experimental lattice data of monoclinic [126] and hexagonal [127] structures is available from the literature.

$La_2O_2CO_3$	DFT calculated data	Experimental data [33,34]
Monoclinic	a = 12.286 Å	a = 12.239 Å
	b = 7.097 Å	b = 7.067 Å
	c = 16.531 Å	c = 16.465 Å
	β = 75.677	β = 75.690
Hexagonal	a = 4.100 Å	a = 4.076 Å
	b = 4.100 Å	b = 4.076 Å
	c = 16.053 Å	c = 16.465 Å
	γ = 120	γ = 120

2.3.3. CO_2 Electrochemical Reduction

Figure 2.8 shows LSV curves ranging from 0 to −0.6 V vs. Ag/AgCl for PL-12h and HL-12h in CO_2-saturated 0.1 M $NaHCO_3$ electrolyte. HL-12h exhibits a maximum total current density of −25.2 mA/cm^2 at −1.26 V vs. Ag/AgCl, whereas a maximum current density of −17.97 mA/cm^2 for PL-12h is achieved at −1.438 V vs. Ag/AgCl. In addition, HL-12h shows a more positive onset potential toward CO_2 electrochemical reduction than PL-12h in **Figure 2.8**. Both the higher current density and more positive onset potential apparently indicate a higher activity toward the CO_2 electrochemical reduction in HL-12h compared to that of PL-12h.

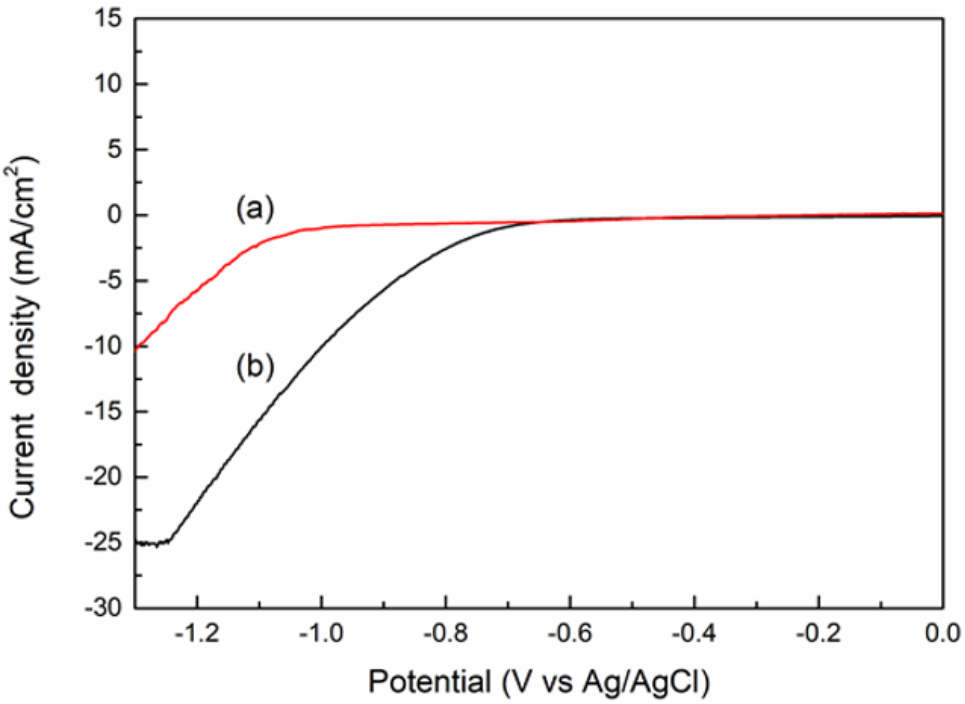

Figure 2.8. Linear sweeping voltammetry (LSV) curves of electrodes at various reaction times in a 0.1M $NaHCO_3$ solution at a scan rate of 20 mV/s: (a) PL-12h; (b) HL-12h.

The chronoamperometry (CA) experiments were performed at different potentials for each 10 min, and gaseous products were determined by GC. For both PL-12h and HL-12h, the main gaseous products are CH_4, C_2H_4, C_2H_6 and H_2. **Figure 2.8** shows the Faraday efficiency (FE) of carbon-containing products for PL-12h and HL-12h, resulting in a much higher FE for HL-12h than those for PL-12h. C_2H_4 is a dominant carbonaceous product at lower potential. A maximum of the ethene FE (9.4%) for HL-12h is achieved at −0.6 V (vs Ag/AgCl), while that for PL-12h is lower than 5%. Interestingly, CO gas was not detected in the potential range, even for the two $La_2O_2CO_3$ samples. This indicates that $La_2O_2CO_3$ catalysts are efficient for C-C coupling rather than desorption to form CO gas, since CO is an intermediate for CO_2 transformation to ethene during CO_2 reduction [131]. The superior electrocatalytic activity of HL-12h to PL-12h would result from the better CO_2 adsorption ability which can optimize the first step involving electron and proton transfer to form a *COOH intermediate, which is then

converted to other carbonaceous products [130]. The higher electronegativity of hexagonal $La_2O_2CO_3$ of HL-12h leads to the better CO_2 adsorption ability [134].

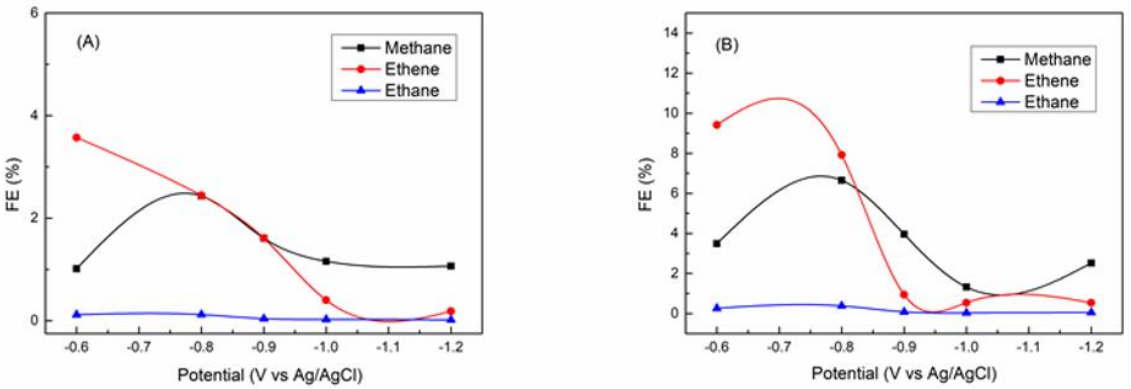

Figure 2.9. FE values for the (A) PL-12h and (B) HL-12h as a function of the potential.

2.4. Conclusions

In this study, $La_2O_2CO_3$ nanoparticles with hexagonal and monoclinic phases were prepared by different preparation methods, and the CO_2 behavior on each crystalline structure was investigated by CO_2-TPD, TGA measurements, and CO_2 electrochemical reduction. The hydrothermal method produced the hexagonal type II $La_2O_2CO_3$ phase, whereas the monoclinic type Ia phase was synthesized by the precipitation method (PL-12h and PL-24h). The initial $La(OH)_3$ phase was transformed into the $La(OH)CO_3$ phase by the reaction with CO_2 supplied from air in the precipitation method. The hexagonal $La_2O_2CO_3$ phase showed a higher CO_2 adsorption ability on the surface and a higher stability in the bulk structure than the monoclinic phase, owing to the differences in optimized crystalline structures predicted by the DFT calculation. Consequently, the hexagonal $La_2O_2CO_3$ phase of HL-12h had a higher current density and a more positive onset potential than the monoclinic $La_2O_2CO_3$ of PL-12h in CO_2 electrochemical reduction.

Chapter 3. Influence of macroporous structure of ZnO/ $La_2O_2CO_3$

3.1. Introduction

Lanthanum has been widely employed as an electronic material [135], a special glass for optical devices [136], and in catalysts (or supports) [137-140] because it has unique electric, optical, and catalytic properties due to its partially filled 4f shell electronic configuration. The solid state compounds of lanthanum have also been used for diverse applications in the forms of oxide, hydroxide, carbonate, titanate and oxycarbonate [141-148]. Specially, lanthanum oxycarbonate has been reported as a promising CO_2 sensor and efficient catalyst (or support). Single phase $La_2O_2CO_3$ nanoparticles were synthesized by a hydrothermal process, resulting in good sensing properties for CO_2 [142]. The $La_2O_2CO_3$ phase was also introduced as a catalyst support for hydrogen production processes and an active intermediate of La_2O_3 in the dry reforming of methane [143,145]. Recently, $La_2O_2CO_3$/ZnO materials were used as catalysts for CO_2-based reactions [146-148] and as commercially-available heterogeneous catalysts for microwave-assisted biofuel production [149].

Controlling the structural properties (including size, shape, and phase) is of considerable interest because it is a key variable influencing material performance [142,144-146,150-152]. The size of $La_2O_2CO_3$ nanoparticles had an effect on the catalytic activity and CO_2-sensing response [142,150]. Porous $La_2O_2CO_3$ material made of hollow microspheres was successfully fabricated and applied for fluorescent biological labeling [151]. Metal catalysts supported by nanorod-shaped $La_2O_2CO_3$ exhibited excellent catalytic performance in selective hydrogenation and dry reforming of methane [144,145]. The existence of $La_2O_2CO_3$ phase in the dry reforming of methane enhanced the removal of carbonaceous deposits from neighboring active sites [145,153,154]. Meanwhile, ordered or disordered macroporous La-containing materials have been prepared by various methods [146,155,156]. Sadakane et al. introduced a facile preparation route to form orderedmacroporous perovskite-type mixed $La_{1-x}Sr_xFeO_3$ materials using colloidal crystal templating method [155].

Disordered macroporous $La_{1-x}K_xCo_{1-y}Fe_yO_3$ complex oxide catalysts were synthesized by an ethylene glycol-ligation and solution combustion method and used for diesel soot combustion [156]. In addition, the disordered macroporous $La_2O_2CO_3$/ZnO materials were prepared by a solution combustion method [146]. The $La_2O_2CO_3$ phase influenced the catalytic performance in studies of $La_2O_2CO_3$/ZnO materials for glycerol carbonylation with CO_2; the monoclinic $La_2O_2CO_3$ phase in the materials was superior to the hexagonal $La_2O_2CO_3$ phase in the production of glycerol carbonate [146]. However, in literature, the structural properties of the disordered macroporous $La_2O_2CO_3$/ ZnO materials have not yet been investigated in detail. In this study, disordered macroporous $La_2O_2CO_3$/ZnO materials were prepared by a solution combustion method, and their microstructures and phases were investigated as functions of the La/Zn ratios and the calcination temperatures to understand their structural properties. The disordered macroporous structure of the materials was well developed with the formation of monoclinic $La_2O_2CO_3$ phase irrespective of the La/Zn ratios as well as the calcination temperatures. Even at high temperature calcination (700 °C), the disordered macroporous morphology was maintained while the monoclinic $La_2O_2CO_3$ [[1] was transformed into La_2O_3. The disordered macroporous $La_2O_2CO_3$/ZnO materials in this study have a potential as a heterogeneous catalyst for CO_2-related or heavy-coke generated chemical reactions.

3.2. Materials and analysis technologies

3.2.1. Preparation procedures

3.2.1.1. Synthesis of disordered macroporous ZnO/$La_2O_2CO_3$

We prepared disordered macroporous $La_2O_2CO_3$/ZnO materials by a solution combustion method [146]. In the preparation, $Zn(NO_3)_2{\cdot}6H_2O$ (Sigma-Aldrich Korea, Gyounggi, South Korea) and $La(NO_3)_3{\cdot}9H_2O$ (Sigma-Aldrich Korea, Gyounggi, South Korea) were used as starting materials. Two precursors were dissolved into the ethylene glycol solution at ambient temperature for 2 h. After complete mixing, moderate amounts of methanol were added. Then,

the ethylene glycol-methanol solution was mixed with metal nitrates, heated in a muffle furnace with the ramping rate of 1° C/min to the selected calcination temperature, and held there for 5 h. The final products were named as "LZ-x-y" where x and y indicate the La and Zn atomic ratio and the calcination temperature, respectively.

3.2.1.2. Synthesis of nanoparticle ZnO/$La_2O_2CO_3$

For comparison, another type of $La_2O_2CO_3$/ZnO materials was synthesized by a conventional co-precipitation method. $Zn(NO_3)_2 \cdot 6H_2O$ (Sigma-Aldrich Korea, Gyounggi, South Korea) and $La(NO_3)_3 \cdot 9H_2O$ (Sigma-Aldrich Korea, Gyounggi, South Korea) were well dissolved into a 2 M NaOH solution, and the mixed solution was added dropwise to deionized water. The detailed procedure for the preparation is described elsewhere [146]. The materials calcined at different temperatures were named as "CoLZ-x-y," where x and y indicate the La and Zn atomic ratio and the calcination temperature, respectively.

3.2.2. Characterization techniques

To obtain information on the morphology of the composite materials, the samples were investigated using field emission-scanning electron microscopy (FE-SEM, JSM-600F, JEOL, Japan) and high-resolution transmission electron microscopy (HR-TEM, JEM-2100F, JEOL, Japan). Samples were cast onto carbon-coated copper grids.

The wide-angle powder X-ray diffraction (XRD, Rigaku D/MAZX 2500V/PC high-power diffractometer, Japan) with an X-ray source employing Cu Kα radiation of maximum wavelength λ_{max} = 1.5415 Å and a scanning rate of 2° (2θ)/min were used for investigating crystalline structures of the composite materials. The porosity characteristics of the photocatalysts were measured by means of N_2 sorption analysis using a Micromeritics ASAP 2020 instrument (USA). The specific surface area, pore volume and pore size distribution

were determined by the Brunauer-Emmett-Teller (BET) and Barret-Joyner-Halenda (BJH) calculations. The infrared spectra of the composite materials were collected using a Nicolet 380 Fourier transform infrared (FTIR) spectrophotometer (ThermoFisher Scientific Co., Waltham, MA, USA). The spectrum was acquired by adding 124 scans with a resolution of 4 cm^{-1} .

3.2.3. Electrocatalytic performance

The CO_2 electrochemical reduction was carried out via the LSV measurement with an Ag/AgCl electrode as a reference electrode and Pt wire as a counter electrode. The working electrode was prepared by dispersing 2 mg of the samples in a mixture of 100 μL of alcohol and 5 μL of 5% Nafion and then pipetting 10 μL of suspension on the GCE (0.07065 cm^2). The working electrode was tested 20 times at a scan rate of 20 mV/s. The electrolyte was 0.5 M $KHCO_3$ saturated with CO_2. Before each experiment, high-purity CO_2 gas was bubbled at a flow rate of 30 mL/min for 30 min to remove all oxygen from the electrolyte. The generated gaseous products (H_2, CO, CH_4, and C_2H_4) of CO_2RR were analyzed by a gas chromatograph (GC9800, Kechunang, equipped with a thermal conductivity detector and a flame ionization detector with a methanizer.

The potential (E) was shown as reversible hydrogen electrode (RHE) potentials using the Nernst formula as below：(all the potential was obtained without iR compensation)

$$E_{(vs\ RHE)} = E_{(vs\ Ag/AgCl)} + 0.197\ V + 0.059\ V * pH$$

3.3. Results and discussions

3.3.1. Characterization of electrocatalysts

3.3.1.1. ZnO/$La_2O_2CO_3$ synthesized by a solution combustion method

The physicochemical properties of the materials prepared by solution combustion and conventional co-precipitation methods are listed in **Table 3.1**. The Brunauer-Emmett-Teller (BET) surface areas of the LZ and CoLZ materials were in the range of 10.8-38.1 m^2 /g, which is similar to those in the literature [146-148]. There was no trend in BET surface area with preparation methods or La/Zn ratio. The pore volumes also showed no trend with preparation method or La/Zn ratio (0.116-0.353 cm3 /g). **Figure 3.1** and **Figure 3.2** show the isotherms for LZ and CoLZ materials, respectively. Irrespective of the preparation methods or the existence of macropores, all of the isotherms follow the type V adsorption pattern with the type H3 hysteresis loop, implying that mesoporosity of LZ and CoLZ materials is similar. However, the values measured by the N_2 adsorption/desorption technique imply that the materials in this study were well prepared.

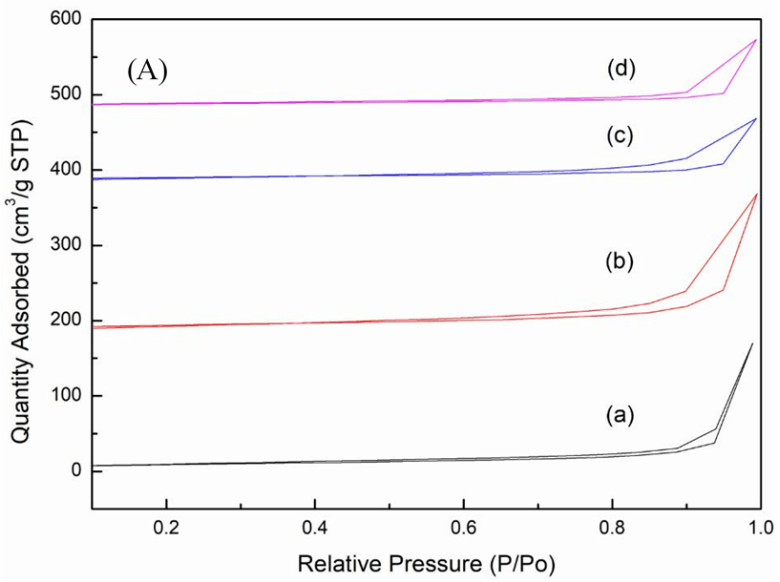

Figure 3.1. Nitrogen adsorption-desorption isotherms of (a) LZ-0.125- 550, (b) LZ-0.25-550, (c) LZ-1-550, and (d) LZ-2-550.

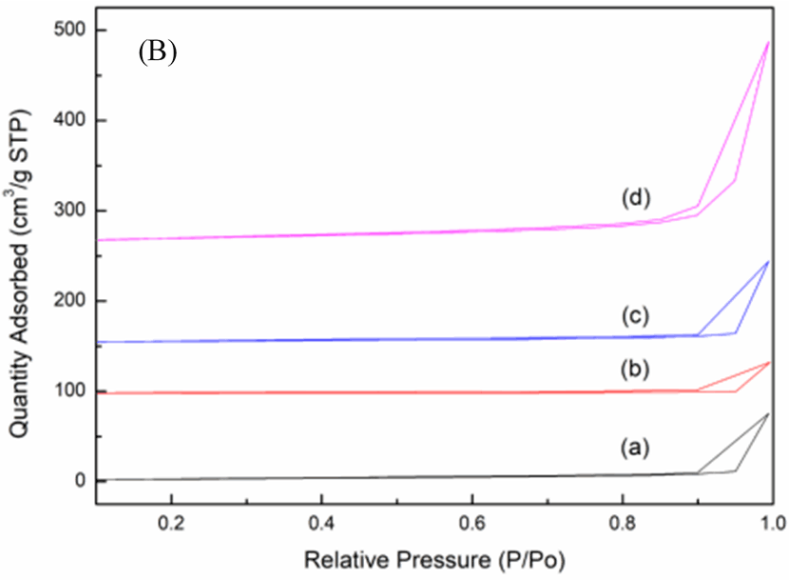

Figure 3.2. Nitrogen adsorption-desorption isotherms of (a) CoLZ-0.125-500, (b) CoLZ-0.25-500, (c) CoLZ-1-500 and (d) CoLZ-2-500.

FE-SEM images of the LZ composite materials with different La/Zn ratios are displayed in **Figure 3.3**. As a whole, all the FE-SEM images of the LZ composite materials clearly confirmed the disordered macroporosity generated by the solution combustion method during the preparation step. The disordered macro-porosity was well developed in all for the LZ composite materials due to the release of gases in the combustion step, but there was a slight change in the disordered macroporosity depending on the La/Zn ratio. That is, the thickness of the disordered-macroporous framework in the LZ composite materials became slightly thinner as the La/Zn ratio increased. Additionally, at La/Zn = 1, the regularity of the macroporous framework (including the thickness) was relatively high (**Figure 3.3(c)**), implying the La/Zn = 1 would be an optimal value for preparing the disordered-macroporous structure. **Figure 3.4(a-d)** shows FE-SEM images of the CoLZ composite materials prepared by the conventional co-precipitation method. The CoLZ composite materials were composed of agglomerates of nanoparticles. As with the LZ composite materials, the nanoparticle morphology of the CoLZ composite materials changed slightly depending on the La/Zn ratio. The irregular nanoparticles with various particle sizes

became larger up to a La/Zn ratio of 1. Then, the nanoparticle size in CoLZ-2-550 suddenly decreased (**Figure 3.4 (d)**). In summary, the solution combustion methods resulted in the disordered macroporosity of the LZ composite materials, which is clearly different from nanoparticle-aggregating morphology observed in the conventional CoLZ composite materials.

Meanwhile, the elemental composition in the composite materials was analyzed by EDS measurements. Actual La/Zn ratios are listed in **Table 3.1** based on the results from the EDS elemental measurements. Even though the actual La/Zn values in the composite materials were a little different from the nominal La/Zn values, the overall trends in the La/Zn ratios were similar.

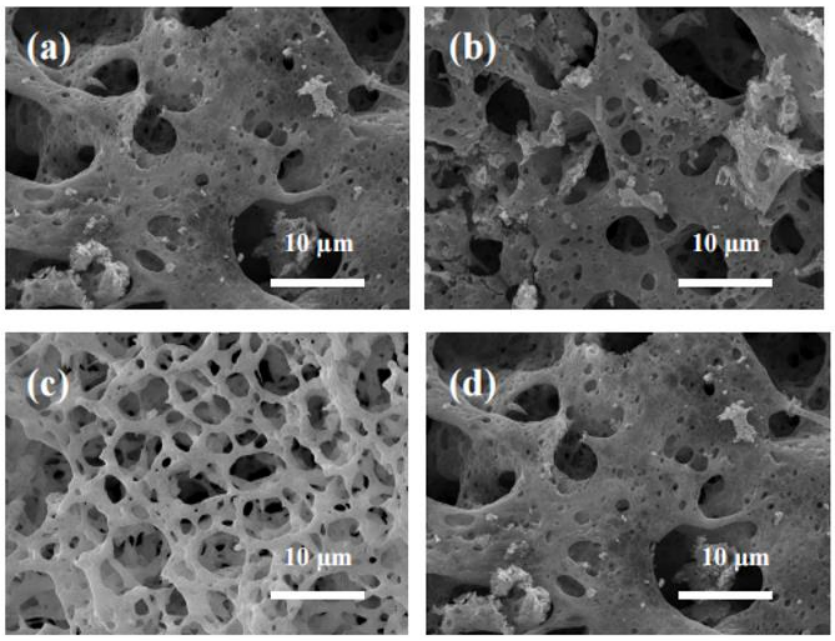

Figure 3.3. FE-SEM images of (a) LZ-0.125-550, (b) LZ-0.25-550, (c) LZ-1-550, and (d) LZ-2-550.

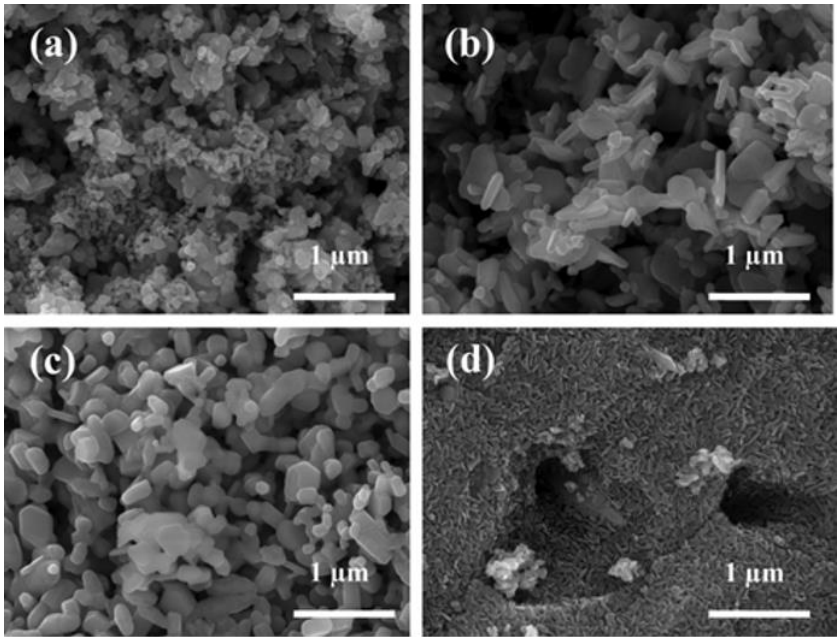

Figure 3.4. FE-SEM images of (a) CoLZ-0.125-500, (b) CoLZ-0.25-500, (c) CoLZ-1-500 and (d) CoLZ-2-500.

Table 3.1. Physicochemical properties of $La_2O_2CO_3$/ZnO composite materials.

Sample	S_{BET} (m^2/g)	Pore volume (cm^3/g)	La/Zn*	Crystallite size (nm)**		
				Hexagonal $La_2O_2CO_3$	Monoclinic $La_2O_2CO_3$	ZnO
LZ-0.125-550	28.1	0.327	0.114	-	-	7
LZ-0.25-550	36.5	0.285	0.180	-	12	4
LZ-1-550	17.4	0.128	1.373	-	14	10
LZ-2-550	14.4	0.137	1.735	8	14	10
CoLZ-0.125-500	10.8	0.117	0.095	44	20	35
CoLZ-0.25-500	10.9	0.116	0.197	58	-	36
CoLZ-1-500	10.9	0.142	1.158	58	-	35
CoLZ-2-500	38.1	0.353	2.417	58	-	29

*Values were obtained from the EDS elemental analysis

**Values were calculated using the Scherrer equation for the corresponding XRD characteristic peaks of the phases

Figure 3.5 shows the XRD patterns of the LZ composite materials prepared at various La/Zn ratios. The typical XRD characteristic peaks for zincite ZnO with a P63mc space group

(JCPDS 36-1451) were observed at 2θ = 31.8°, 34.4°, 36.3°, 47.5°, 56.6°, and 62.9° for all the LZ composite materials. The peak intensity of the ZnO phase depended on the La/Zn ratio. The XRD peak intensity of the ZnO phase decreased with increasing the La/Zn ratio, indicating the low crystallinity of the ZnO phase at high La/Zn ratios. Similarly, the ZnO crystallinity in the LZ composite materials was relatively lower than that of the CoLZ composite materials when comparing the XRD peak intensities of the ZnO phase **(Figure 3.6)**. Through the Scherrer equation, the ZnO crystallite sizes for all the composite materials were calculated, and the values are listed in **Table 3.1**. As expected, the ZnO crystallite sizes in the LZ composite materials (7–10 nm) were much smaller than those in the CoLZ composite materials (28–36 nm), which could be related to the preparation method since the combustion method might inhibit stable growth of each nanoparticle in the LZ composite materials.

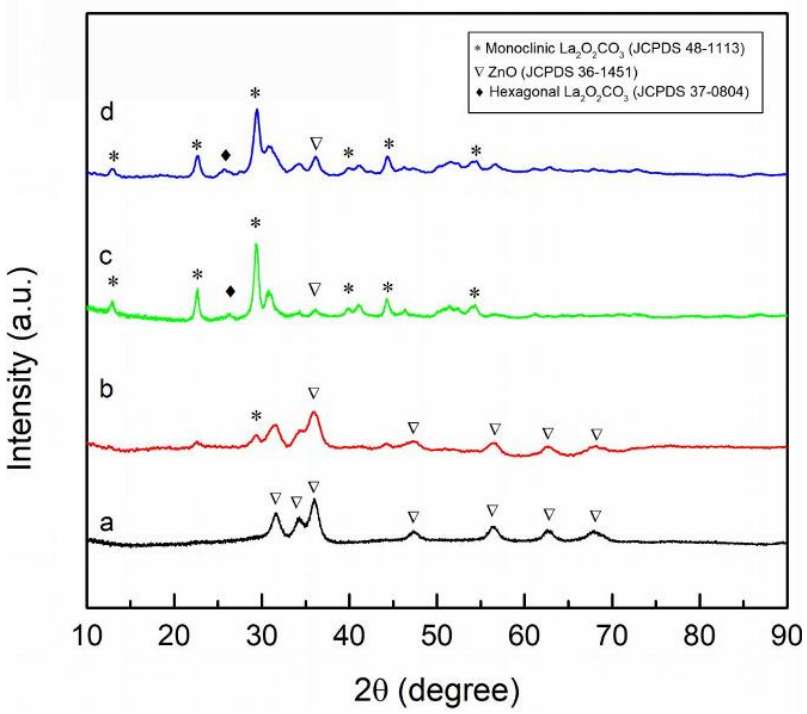

Figure 3.5. XRD patterns of (a) LZ-0.125-550, (b) LZ-0.25-550, (c) LZ-1- 550, and (d) LZ-2-550.

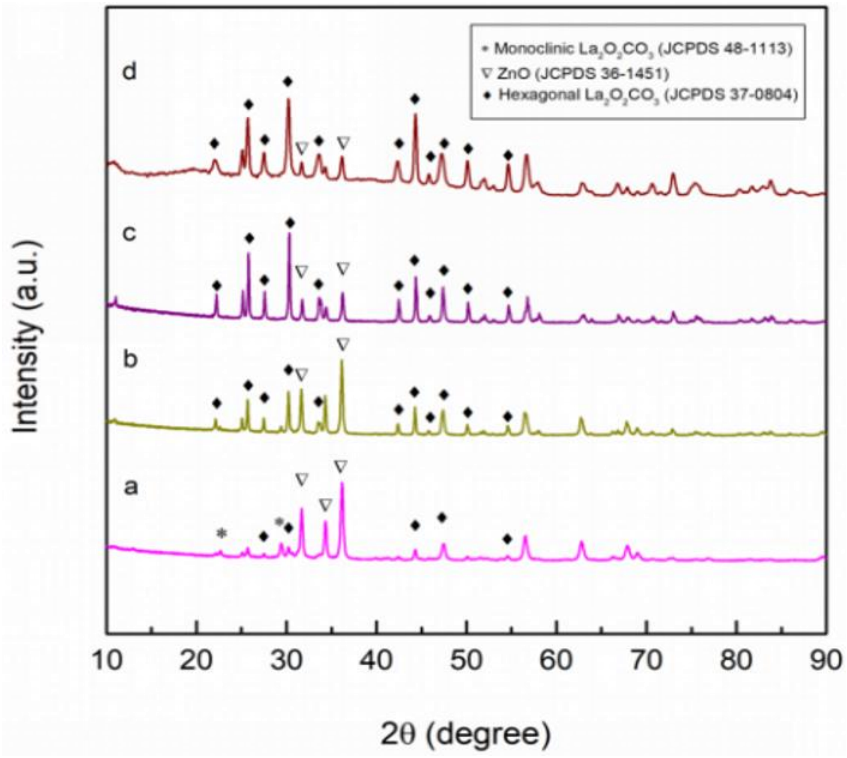

Figure 3.6. XRD patterns of (a) CoLZ-0.125-500, (b) CoLZ-0.25-500, (c) CoLZ-1-500 and (d) CoLZ-2-500.

As shown in **Figure 3.5** and **Figure 3.6** two types of La oxycarbonate were detected: the monoclinic and hexagonal $La_2O_2CO_3$ phases. The XRD patterns of the LZ composite materials show that the monoclinic $La_2O_2CO_3$ phase was mainly observed, indicating that it was dominant in the LZ composite materials. At La/Zn = 0.125, there were no XRD characteristic peaks for $La_2O_2CO_3$ phases (**Figure 3.5(a)**). As the La/Zn ratio increased, the XRD peaks for the monoclinic $La_2O_2CO_3$ phase with a *P*63/*mmc* space group (JCPDS 48-1113) clearly appeared at $2\theta = 13.1^o$, 22.8^o, 26.7^o, 29.5^o, and 44.4^o (**Figure 3.5(c)**). At the highest La/Zn ratio (La/Zn = 2), small XRD peaks for the hexagonal $La_2O_2CO_3$ phase with a $P6_3/m(176)$ space group (JCPDS 37-0804) were additionally detected (**Figure 3.5(d)**) along with the strong existence of the monoclinic $La_2O_2CO_3$ phase. We observed the following in the LZ composite material series: (i) no $La_2O_2CO_3$ phases appeared at La/Zn = 0.125, (ii) the monoclinic $La_2O_2CO_3$ phase was dominant at La/Zn = 1 and (iii) at La/Zn = 2, the monoclinic $La_2O_2CO_3$ phase was still a main $La_2O_2CO_3$ structure whereas the hexagonal $La_2O_2CO_3$ phase existed as a shoulder. Meanwhile,

the XRD patterns of the CoLZ composite materials show different $La_2O_2CO_3$ phase formation behavior (**Figure 3.6**). Monoclinic and hexagonal $La_2O_2CO_3$ phases co-exist together even at low La/Zn ratio (La/Zn = 0.125) (**Figure 3.6(a)**). As the La/Zn ratio increased, the hexagonal $La_2O_2CO_3$ phase became dominant, resulting in the formation of the highest crystalline hexagonal $La_2O_2CO_3$ phase at La/Zn = 1 (**Figure 3.6(c)**). The crystallinity of the hexagonal $La_2O_2CO_3$ phase in CoLZ-2 decreased a little, which was similar to the trend that the monoclinic $La_2O_2CO_3$ phase crystallinity in the LZ composite materials was the highest at La/Zn = 1. Even in the CoLZ composite materials, the portion of hexagonal $La_2O_2CO_3$ phase relatively increased except for La/Zn = 2. For the co-precipitation method, the hexagonal $La_2O_2CO_3$ phase was strongly formed at La/Zn=1 whereas the solution combustion method mainly generated the monoclinic $La_2O_2CO_3$ phase.

The crystallite sizes of the monoclinic and hexagonal $La_2O_2CO_3$ phases were also calculated using the Scherrer equation, and the values are listed in **Table 3.1**. The monoclinic $La_2O_2CO_3$ crystallite sizes in LZ composite materials increased up to 14 nm at La/Zn = 1, while those in the CoLZ composite materials decreased from 20 nm to the point where none were formed. In contrast, the hexagonal $La_2O_2CO_3$ crystallite sizes were in the range of 44–58 nm for the CoLZ composite materials, clearly showing the preference for the formation of hexagonal $La_2O_2CO_3$ phase in the CoLZ series. In addition, the crystallite sizes (44–58 nm) of the hexagonal $La_2O_2CO_3$ phase in CoLZ series were much greater than those of the monoclinic $La_2O_2CO_3$ phase in LZ series (4–10 nm), implying that the growth of monoclinic $La_2O_2CO_3$ nanoparticles was suppressed in the solution combustion method.

Figure 3.7 shows FTIR spectra of the LZ composite materials prepared at various La/Zn ratios. The assignments of typical FTIR bands for carbonates in $La_2O_2CO_3$ phases were described elsewhere in detail [155-158]. The bands at 845 cm^{-1} showed three-fold splitting due to more than one CO_3^{2-} type, and the band around 1367 cm^{-1} was interpreted as a unique carbonate mode for the monoclinic $La_2O_2CO_3$ phase. As seen in **Figure 3.7**, the behavior of the unique carbonate modes for the monoclinic $La_2O_2CO_3$ phase is consistent with the XRD results. The intensities of

the band at 1367 cm^{-1} apparently increased under specific conditions (La/Zn = 1 or 2 of the LZ composites), matching the existence of the monoclinic $La_2O_2CO_3$ phase in the composite materials. The trend in splitting mode at 845 cm^{-1} was the same, the clear appearance of splitting bands only for the LZ composites with La/Zn = 1 or 2. Therefore, FTIR spectra provided additional evidence for the preference of $La_2O_2CO_3$ phase formation in the composite materials which depends on the crystallinity of the $La_2O_2CO_3$ structure (La/Zn ratio) and the preparation methods.

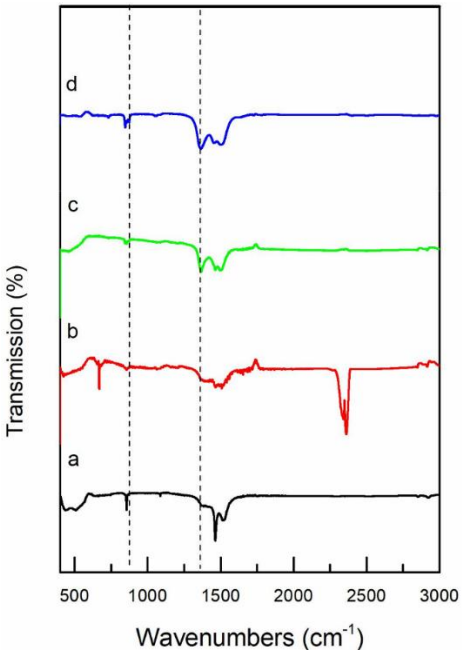

Figure 3.7. FTIR spectra of (a) LZ-0.125-550, (b) LZ-0.25-550, (c) LZ-1- 550, and (d) LZ-2-550.

Figure 3.8 shows the TEM images for the LZ composite materials with different La/Zn ratios. All of the TEM images show an irregularly layered and empty-hole-like structure containing nanoparticles of *ca.* 10 nm. In contrast, dense and big-sized nanoparticles (over 30 nm) appear in the TEM images of the CoLZ composite materials (**Figure 3.9**). This is consistent with the results observed by the XRD measurements.

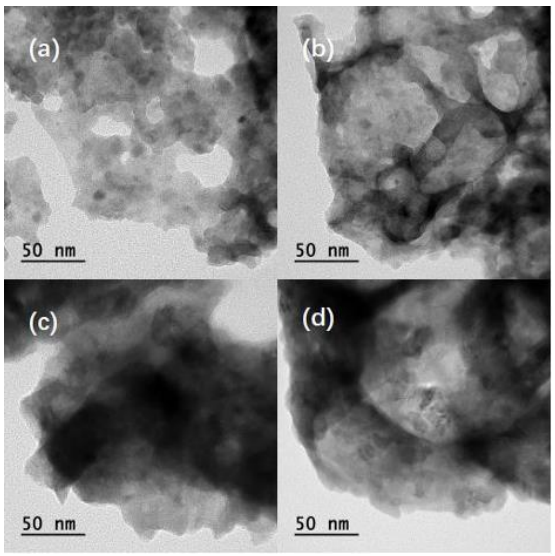

Figure 3.8. HR-TEM images of (a) LZ-0.125-550, (b) LZ-0.25-550, (c) LZ-1-550, and (d) LZ-2-550.

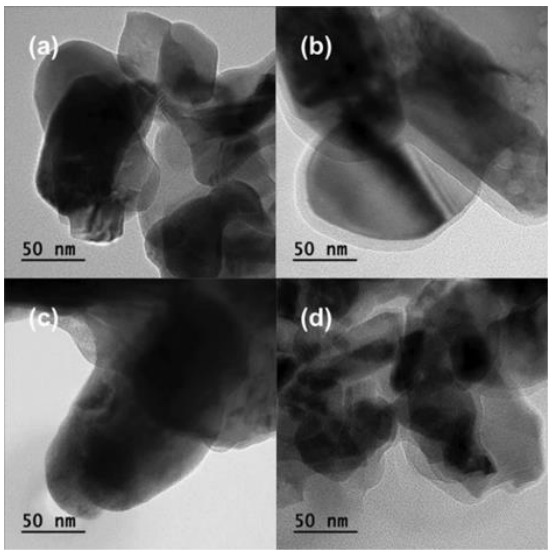

Figure 3.9. HR-TEM images of (a) LZ-0.125-550, (b) LZ-0.25-550, (c) LZ-1-550, and (d) LZ-2-550.

In this study, we also investigated structural properties of the LZ composite materials at different calcination temperatures. The XRD patterns of LZ-1 composites calcined at different temperatures are shown in **Figure 3.10** and **Figure 3.11**. The monoclinic $La_2O_2CO_3$ phase in LZ-1 was stable up to 600 ℃, but the characteristic XRD peaks for the monoclinic $La_2O_2CO_3$ phase were not detected at 650 ℃ and 700 ℃ (**Figure 3.10(d) and (e)**). Instead, the characteristic XRD peaks for the ZnO phase became sharp and clear. At the 700 ℃ calcination, the characteristic XRD peaks for the La_2O_3 phase with a *P-3m1* space group (JCPDS No. 73-2141) appeared at 2θ = 26.1 °, 29.1°, 30.0°, 39.5°, and 46.0°, and the XRD peaks for the ZnO phase became much sharper **(Figure 3.10(e))**. This indicates that the monoclinic $La_2O_2CO_3$ structure collapsed to La_2O_3 phase by releasing CO_2 into the gas phase, and ZnO nanoparticles agglomerated simultaneously. In contrast to this behavior, the XRD patterns of CoLZ-1 remained unchanged even at 650 ℃. The intensities of the characteristic XRD peaks for the hexagonal $La_2O_2CO_3$ phase were still strong irrespective of increasing calcination temperature up to 650 ℃ (**Figure**

3.11), implying higher stability of the hexagonal $La_2O_2CO_3$ phase in CoLZ-1 than the monoclinic $La_2O_2CO_3$ phase in LZ-1. At the 700 ℃ calcination, sharp characteristic XRD peaks for the La_2O_3 phase appeared instead of the peaks of the hexagonal $La_2O_2CO_3$ phase, and the peak intensity for the ZnO phase remained unchanged, which indicates transformation of the hexagonal $La_2O_2CO_3$ into the La_2O_3 phase with no agglomeration of ZnO nanoparticles. Consequently, the thermal stability of the hexagonal $La_2O_2CO_3$ phase in the $La_2O_2CO_3$/ZnO composite materials was greater than that of the monoclinic $La_2O_2CO_3$ phase.

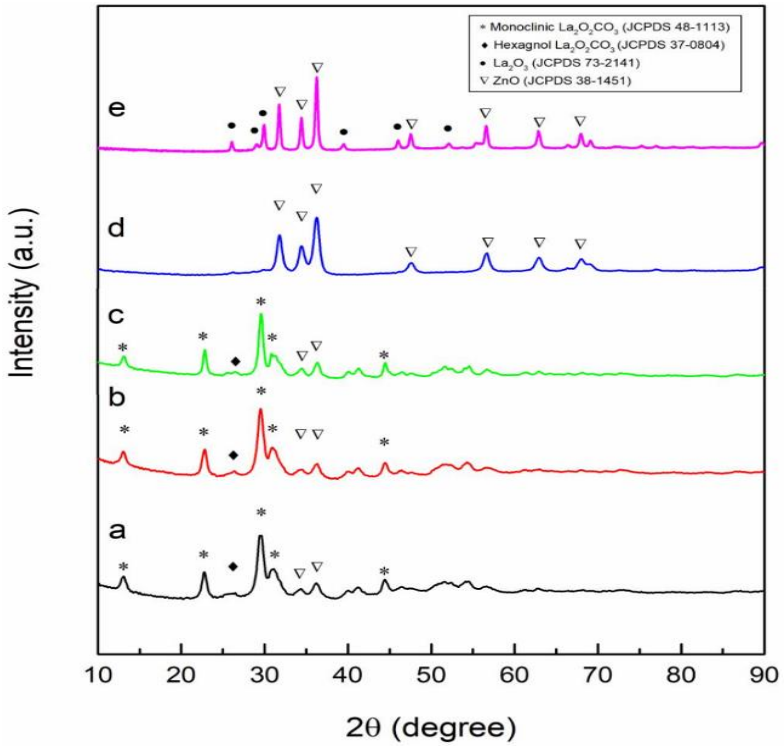

Figure 3.10. XRD patterns of LZ-1 materials calcined at different temperatures. (a) T=500 °C, (b) T=550 °C, (c) T=600 ° C, (d) T= 650 °C, and (e) T=700 °C.

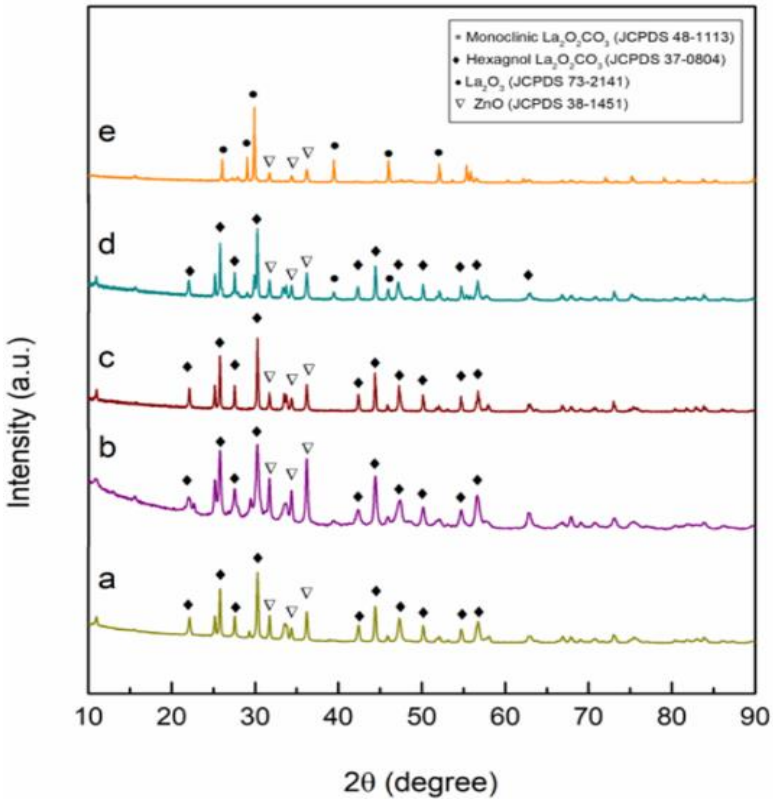

Figure 3.11. XRD patterns of LZ-1 materials calcined at different temperatures. (a) T=500 °C, (b) T=550 °C, (c) T=600 ° C, (d) T= 650 °C, and (e) T=700 °C.

The crystallite sizes of the $La_2O_2CO_3$ and ZnO phases calcined at the different temperatures were calculated by the Scherrer equation. The values are listed in **Table 3.2**. The crystallite sizes of the $La_2O_2CO_3$ phases remained almost unchanged irrespective of increasing the calcination temperatures at around 14 nm for LZ-1 and 49–58 nm for CoLZ-1. Interestingly, the behavior of ZnO crystallite sizes at various calcination temperatures depended on the preparation methods, which is clearly displayed in **Figure 3.12** For the CoLZ composite materials, the ZnO crystallite sizes was maintained at a similar value of around 34 – 39 nm even after the $La_2O_2CO_3$ phase was transformed into La_2O_3 phase at the 700 ℃ calcination. In contrast, the ZnO crystallite sizes for the LZ-1 composte materials suddenly increased from 10 nm to 21 and 24 nm after the CO_2 release from the monoclinic $La_2O_2CO_3$ phase at 650 ℃ and 700 ℃, respectively. Below 600 ℃ calcination and with different La/Zn ratios, the ZnO nanocrystalline sizes were maintained below 10 nm. Accordingly, it can be deduced that there was specific

interaction between the monoclinic $La_2O_2CO_3$ phase and ZnO nanoparticles to inhibit the growth of ZnO nanoparticles in the LZ composite materials.

Table 3.2. Crystallite sizes of each crystalline structure in LZ-1 and CoLZ-1 calcined at different temperatures.

Samples	Crystallite sizes (nm)*		
	Hexagonal La2O2CO3	**Monoclinic LaO2CO3**	**ZnO**
LZ-1-500	-	14	13
LZ-1-550	-	14	10
LZ-1-600	-	14	10
LZ-1-650	-	-	21
LZ-1-700	-	-	24
CoLZ-1-500	58	-	35
CoLZ-1-550	49	-	34
CoLZ-1-600	58	-	39
CoLZ-1-650	54	-	38
CoLZ-1-700	-	-	39

*Values were calculated using the Scherrer equation for the corresponding XRD characteristic peaks of the phases

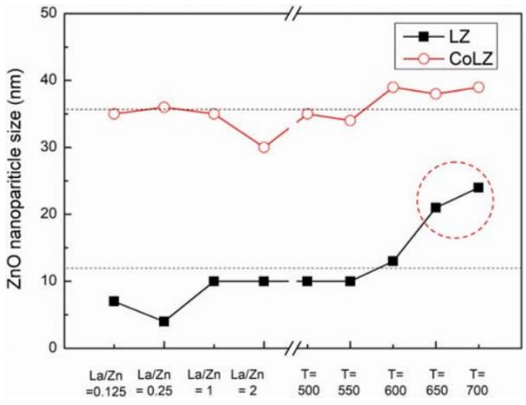

Figure 3.12. ZnO nanoparticle sizes depending on the La/Zn ratios and the calcination temperatures.

Figure 3.13 shows FE-SEM images of the LZ-1 composites calcined at 550 ℃, 650℃ and 700℃. In spite of increasing the calcination temperature, the disordered-macroporous structure in the LZ-1 composites was still maintained. However, a lot of smaller pores were generated in the macroporous framework of LZ-1 calcined at 650 ℃ and 700 ℃ (**Figure 3.13(b-c)**), which is directly related to the CO_2 gas release by the phase transformation from $La_2O_2CO_3$ to La_2O_3.

A schematic illustration of the morphologies and $La_2O_2CO_3$ structures of the LZ composite materials is displayed in **Scheme 3.1**. In the LZ composite materials, the disordered-macroporosity was well developed by the solution combustion method, resulting in small nanocrystallites of ZnO and monoclinic $La_2O_2CO_3$ structures. The continuous gas release in the process of the solution combustion method not only left the disordered-macroporous structure in the solid but also induced the dominant formation of a monoclinic $La_2O_2CO_3$ phase. The presence of the monoclinic $La_2O_2CO_3$ phase in the LZ composites inhibited the growth of ZnO nanoparticles in the disordered-macroporous framework due to the strong interaction between ZnO and monoclinic $La_2O_2CO_3$ nanoparticles, resulting in much smaller ZnO crystallites (4–13 nm) in the LZ composite materials. Conversely, the destruction of the monoclinic $La_2O_2CO_3$ phase by the calcination above 650 ℃ caused a rapid agglomeration of ZnO nanoparticles in the LZ-1 composites (21 – 24 nm). On the other hand, the CoLZ composite materials were composed of aggregates of ZnO and hexagonal $La_2O_2CO_3$ nanoparticles. The larger crystallites of ZnO phase (28 – 36 nm) in the CoLZ composite materials implies no interaction between hexagonal $La_2O_2CO_3$ and ZnO nanoparticles in the conventional co-precipitation process, resulting in the no difference in the ZnO crystallite sizes even after the calcination at 700 ℃.

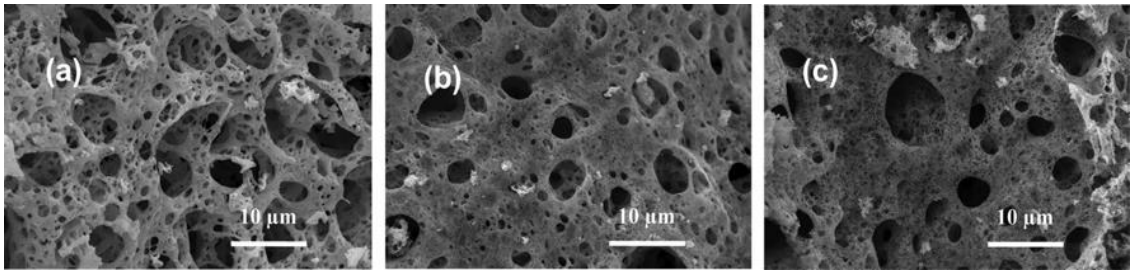

Figure 3.13. FE-SEM images of LZ-1 materials calcined at different temperatures. (a) T=550°C, (b) T=650°C, and (c) T=700°C

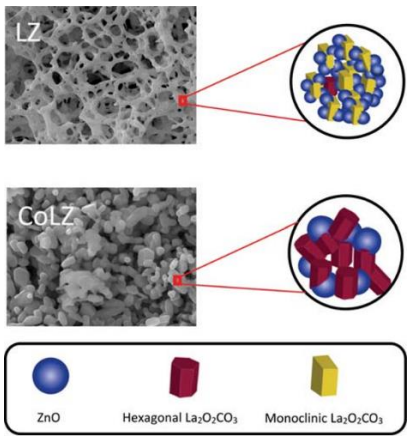

Scheme 3.1. Schematic illustration of morphologies and crystalline structures of LZ and CoLZ.

3.3.2. CO_2 electroreduction activity

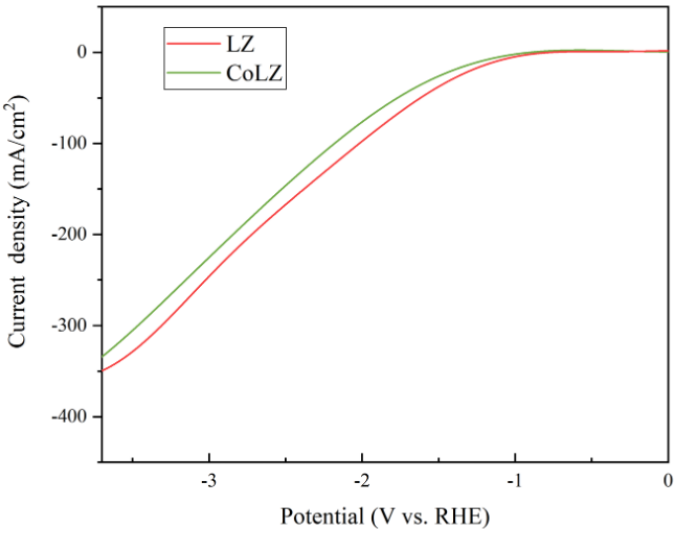

Figure 3.14. LSV curves of LZ and CoLZ in CO_2-saturated 0.5 M $KHCO_3$ solution, scan rate = 100 mV·s^{-1}.

The electrochemical activity of CO_2RR of the LZ and CoLZ were evaluated through LSV method between -0.1 V and -3.8 V at a rate of 100 $mV \cdot s^{-1}$ in CO_2 saturated 0.5 M $KHCO_3$ solutions. Under the condition of CO_2 saturation, the required for the current density of 1 $mA \cdot cm^{-2}$ was defined as the CO_2RR onset potential.[60] As shown in Figure 3.3.1, the CO_2RR onset potential of CoLZ was -0.955 V, which was more negative than those of the LZ (-0.845 V), indicating that LZ had better activity toward CO_2RR.

The CO_2 electroreduction activities of LZ and CoLZ catalysts were tested in a typical H-type cell **(Scheme 3.2**) and CO_2-saturated 0.5 M KHCO3 solution (pH 8.81) was used as electrolyte. Controlled potential electrolysis of CO_2 at each given potential was then performed. Solution phase and gas-phase products were quantified by nuclear magnetic resonance (NMR) spectroscopy and gas chromatography (GC), respectively. Under these conditions, various products, including ethylene, methane, CO, and H_2, were detected with a combined FE of around 100 % for all the studied catalysts (**Figure 3.15** and **Figure 3.16**). The dominant product of CO_2 electroreduction $ZnO/La_2O_2CO_3$ is CO. The maximum FE_{CO} for CO_2 electroreduction products over LZ and CoLZ were 30.96% and 50.1%, respectively. Interestingly, for CoLZ, C_2H_4 products could not be detected compared to LZ catalyst. Since the CO is the intermediate of other further hydrocarbon products, the LZ sample shows higher conversion ability of the CO and the maximum FE for C_2H_4 were 7.3% at -1.3V vs. RHE. The results indicate that the disordered macroporous structure of $ZnO/La_2O_2CO_3$ could benefit to produce C_2H_4 products by converting the CO.

Scheme 3.2. Schematic illustration of H-cell for CO_2RR.

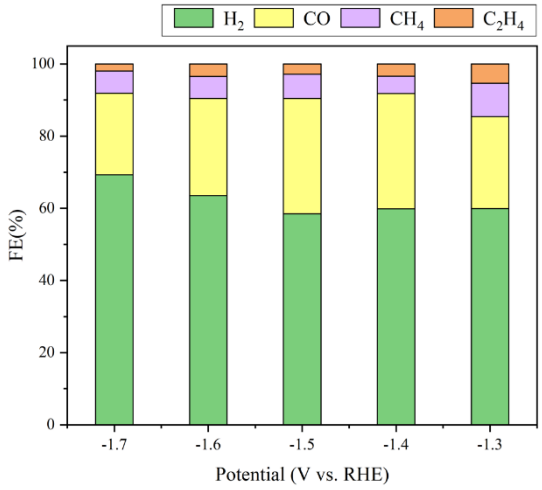

Figure 3.15. The faraday efficiencies of LZ catalysts at different potentials ranging from – 1.3 V to -1.7 V in CO_2-saturated 0.5 M $KHCO_3$ solution.

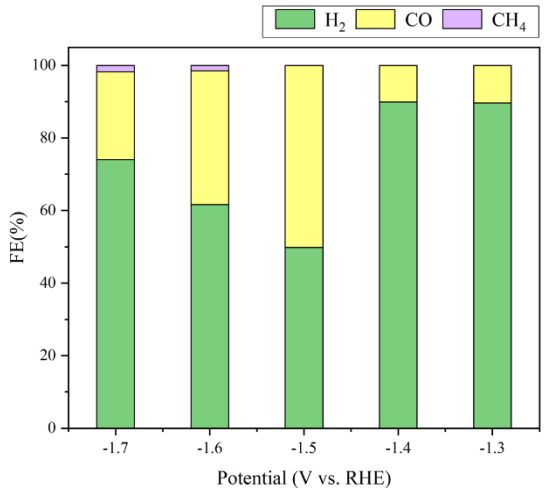

Figure 3.16. The faraday efficiencies of CoLZ catalysts at different potentials ranging from – 1.4 V to -1.8 V in CO_2-saturated 0.5 M $KHCO_3$ solution.

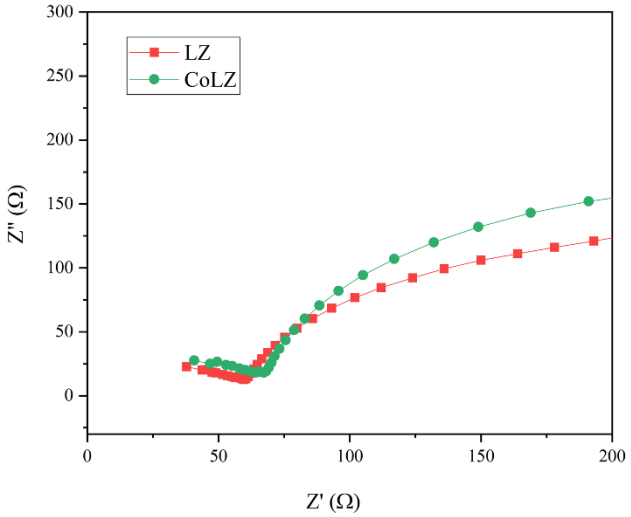

Figure 3.17. Nyquist plots for different electrodes in CO_2-saturated 0.5 M $KHCO_3$ electrolyte.

The electrochemical impedance spectroscopy (EIS) was also conducted, and the Nyquist plots were obtained by running the experiment at an open circuit potential (**Figure 3.17**). LZ showed the lower interfacial charge transfer resistance, suggesting that electron transfer on LZ electrode surface was more facile than others. Therefore, LZ showed significant advantages in all the key steps for CO_2 electroreduction to ethylene.

3.4. Conclusions

In this work, disordered-macroporous $La_2O_2CO_3$/ZnO composite materials were synthesized as function of the La/Zn ratios and the calcination temperatures by the solution combustion method. All of the composite materials prepared by the solution combustion method clearly showed a disordered-macroporous framework which were composed of ZnO and monoclinic $La_2O_2CO_3$ nanoparticles. On the contrary, the composite materials prepared by the conventional co-precipitation method were composed of aggregates of nanoparticles with the dominant formation of hexagonal $La_2O_2CO_3$ phase. The calcination at 700 °C transformed the $La_2O_2CO_3$ phase into La_2O_3 phase in the composite materials. Based on the sizes of ZnO nanoparticles, the ZnO nanoparticles in the disordered-macroporous LZ composite materials

would interact strongly with the monoclinic $La_2O_2CO_3$ nanoparticles, which caused the inhibition of growth of the monoclinic $La_2O_2CO_3$ phase in the disordered-macroporous LZ composites. The addition of ZnO to the $La_2O_2CO_3$ electrocatalyst increased the production of CO. However, the LZ catalyst had higher current density and more positive onset potential. In addition, LZ showed the lower interfacial charge transfer resistance. The disordered macroporous structure of $ZnO/La_2O_2CO_3$ could offer great advantageous in electrochemical applications since macropore channels permit fast ions transport to increase the selectivity of C_2 products, but also reduced the overpotential.

PART III –COPPER OXIDE AND ITS COMPOSITES IN CO_2 ELECTROREDUCTION

Chapter 4. Electrical and Structural Properties of Copper oxide supported by $La_2O_2CO_3$

4.1. Introduction

Electrochemical CO_2 reduction has emerged as a promising strategy powered by renewable energy, which can produce fuels and commodity chemicals in a carbon-neutral way.[161-165] The activity of CO_2 reduction has been boosted by various factors and strategies, such as controlling morphology of nanostructured catalysts,[166-169] manipulation of oxidation states,[170-172] incorporation with other component,[173-176] and selecting suitable electrolyte.[17-18] Strikingly, when compared to C_1 products, C_2 counterparts have more considerable energy density and economical value. Up to date, Cu-based materials have proved to be the stand out as electrocatalysts because of their capability to convert CO_2 into long-chain hydrocarbons and multi-carbon oxygenate (C_{2+} products). [179-187] In specific, it is reported that oxide-derived copper synthesized by a common method can boost CO_2 molecules activation and C-C bond formation extremely, where the surface Cu^+ sites were proposed to be the active sites for CO_2 electroreduction. [178] To summarize the previous research findings, it is found that the preparation method of oxide-derived catalysts played an important role for the selectivity of the products. In general, the methods can be classified into two types: [179-182] annealing and uncalcined methods. The annealed Cu_2O showed higher selectivity for C_1 products than C_2 products at low overpotential. The total C1 faradic efficiency (FE) of 70 % (40 % CO and 30 % HCOOH) can be achieved. [189] In addition, it is discovered that electroreduction annealed oxide-derived copper could produce CO with FE reached to 60 %.[190] The annealing technique can lower the overpotential for CO_2 reduction, but the dominant product was CO while the FE of C_2 products

were poor. Interestingly, oxide-derived copper synthesized by the unannealed method seems to prefer C_2 products. An electrodeposited Cu_2O shows promising selectivity for ethylene where the FE can be achieved to reach up 40 %.[191] Moreover, O-plasma-treated Cu electrode can reach high FE of ethylene up to about 60 %[192] and the Cu-based catalyst prepared by in situ electrosynthesis achieve total FE of ethanol and acetate up to 80 %.[193] Currently, it is found that a branched Cu_2O nanoparticles synthesized in aqueous ammonia solution can efficiently reduce CO_2 to ethylene, and the FE is about 70%.[194] Further studies prove that Cu^+ can promote CO_2 to form C_2 products over the unannealed oxide-derived copper own to the facilitation of C-C dimerization whilst they also suffer from high overpotentials [195].

Here we design the macroporous Cu nanoparticles supported by $La_2O_2CO_3$ as an electrocatalyst for ethylene synthesis from CO_2RR. The nano-scaled defects are in size of 2-14 nm, which can be considered as a large collection of atomic defects. Such a nano-defective structure strengthens the adsorption, enrichment and confinement for reaction intermediates and hydroxyl ions on the electrocatalyst. The C-C coupling is thus promoted to produce ethylene efficiently. The mechanism for the high ethylene selectivity on the macroporous copper oxide was investigated by a series of experiments.

4.2. Materials and analysis technologies

4.2.1. Preparation procedures

CuO nanosheets were synthesized in a high concentrated alkaline solution. 1.2 mL of 0.05 M, 0.1 M, 0.2 M $CuCl_2$ aqueous solution was dropwise added into 4.0 mL of $La_2O_2CO_3$ aqueous solution (concentration, 1.0 mg/mL) and stirred for 2 h. Then, 1.8 mL of 2 M NaOH solution was slowly added into the mixture to get a suspension. The solution was vigorously stirred and then transferred into a Teflon-lined autoclave, sealed and heated at 100 °C for 10 h. The system was allowed to cool to room temperature naturally and the resulting product was centrifuged, rinsed with distilled water and ethanol several times to remove any alkaline salt and then dried in a vacuum oven at 60 °C for 12 h. The CuO nanosheet electrode was via in situ CO_2

electro-reduced at -2 V (vs RHE) from after an initial electrolysis running for 30 min. The catalysts were named as EL-Cu-1, EL-Cu-2, EL-Cu-3.

4.2.2. Electrochemical measurements

To prepare the working electrode, 2 mg of the as-prepared catalyst were dispersed into a mixture solution of 100 μL ethanol and 5 μL of 5.0 wt % Nafion. The solution was homogeneously mixed to get the final uniform catalyst ink by bath-sonication. The uniform ink was then dropcast onto a glass carbon electrode with an diameter of 3 mm and naturally dried. The electrochemical experiments were performed in a gas-tight H-type electrochemical cell and the Nafion-117 proton exchange membrane was used to separate the cathodic and anodic compartment. The working electrode and reference electrode (Ag/AgCl) were mounted in the cathodic compartment while the counter electrode of Pt was placed in the anodic side. For both cathodic and anodic sides, 30 mL of 0.5 M $KHCO_3$ solution was added as the electrolyte. The 0.5 M $KHCO_3$ solution was presaturated with CO_2 (pH = 8.81). During the measurement, CO_2 or at a rate of 20 sccm was continuously bubbled into the solution to keep the saturation of the electrolyte. The potentials (vs. SCE) were transformed to reversible hydrogen electrode (RHE) potential for the final performance characterization. Before the CO_2 electroreduction measurements, the as-prepared catalysts were first reduced t applying a biased potential of -2 V (vs. RHE) for 30 mins.

4.2.3. Characterization techniques

Morphologies of the EL-Cu-*x* materials were investigated via field-emission scanning electron microscopy (FE-SEM, JSM-600F, JEOL, Japan) and high-resolution transmission electron microscopy (HR-TEM, JEM-2100F, JEOL, Japan). Samples were deposited onto carbon-coated Cu grids. Crystalline structures were determined via X-ray diffraction (XRD, Rigaku D/MAZX 2500V/PC high-power diffractometer, Japan) with a Cu Kα X-ray source

(wavelength λ = 1.5415 Å, scanning rate 2° (2θ) min^{-1}). Functional groups of the catalysts were verified via a Nicolet 380 Fourier transform infrared (FTIR) spectrometer (Thermo Electron Co., USA). UV-visible diffuse reflectance spectra (UV-Vis-DRS) were collected with a SPECORD 210 Plus spectroscope (Analytik Jena, Germany). The specific surface area and other porosity characteristics were measured via N_2 adsorption isotherm processes using a Micromeritics ASAP 2020 instrument (USA).

4.3. Results and discussions

4.3.1. Morphology and structural properties

Crystalline phases of the Cu/$La_2O_2CO_3$ materials were determined from X-ray diffraction patterns, as shown in **Figure 4.1**. The XRD pattern of $La_2O_2CO_3$ in the EL-Cu-1 samples matches well with pure hexagonal phase (PDF# 37-0840). With the lower content of copper catalyst, the main phase of EL-Cu-1 is copper oxide (PDF# 02-1040). However, it should be noted that the feature copper peaks of EL-Cu-2 and EL-Cu-3 were converted to tribasic copper chlorides $Cu_2(OH)_3Cl$ (PDF# 04-0836) with increasing ratio of copper precursor gradually. Hence, there is a mixture of CuO with $Cu_2(OH)_3Cl$ in EL-Cu-2 while it's almost pure phase of $Cu_2(OH)_3Cl$ in EL- Cu-3. Furthermore, the XRD pattern of high content Cu/ $La_2O_2CO_3$ also does not show any peak of the crystallite structure of $La_2O_2CO_3$. The signals may be hidden in high content copper phases due to the $La_2O_2CO_3$ is too well-dispersed to distinguish by XRD.

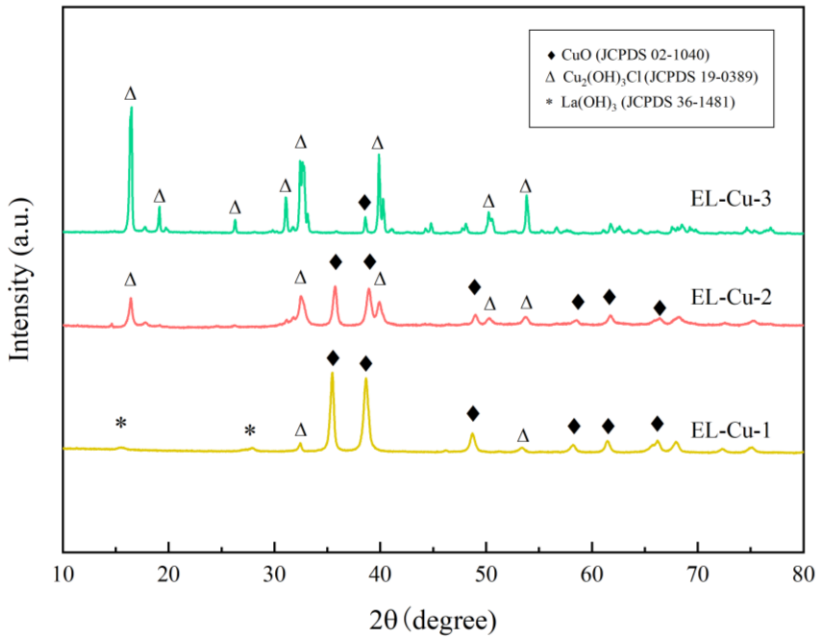

Figure 4.1. XRD patterns of EL-Cu-x.

Fourier transform infrared (FTIR) spectra of the EL-Cu-*x* samples can be seen in **Figure 4.2**. According to the general spectrum analysis method, the observed IR absorption may be readily attributed to the OH-related modes, Cu−O-related modes, Cu−Cl related modes, and lattice modes as well as their sum/ difference/overtones. 37−40 In the high-frequency region typical of functional groups, the IR bands at 3306, 3365, 3449 cm^{-1} can be assigned as the stretching modes of the hydroxyl groups ($v_{O–H}$). They correspond to the two types of OH environments with different atomic distances ($d_{O–H}$) and hydrogen bond angles ($\theta_{O–H\cdots Cl}$). In fact, in the $(O–H)_3\cdots Cl$ interlayer trimeric hydrogen bond, two hydroxyl groups are crystallographically equivalent and the third is not, thus giving rise to the appearance of two vibrational frequencies of $v_{O–H}$ stretching. The IR bands at 1386, 1637 cm^{-1} may be caused by the residual water in the KBr discs and/or the deformation modes of dangling OH groups on the surface. The residual stresses in the KBr discs and large LO-TO splitting effects may contribute to the enlarged bandwidth and the poorly defined spectroscopic profile. The IR bands at 867, 921, 993 cm^{-1} can be assigned to the Cu−O−H deformation modes (δCu−O−H). However, due to the combination of accidental degeneracy, Davydov splitting, and the existence of sum/

difference/overtones, an exact assignment is very difficult in this 1100-600 cm^{-1} window region.

The reaction pathway is proposed as below:

$$2Cu^{2+} + 3OH^{-} + Cl^{-} \rightarrow Cu_2OH_3Cl\downarrow.$$

$$Cu_2(OH)_3Cls + OH^{-} \rightarrow 2Cu(OH)_2s + Cl^{-}$$

$$Cu(OH)_2s \rightarrow CuOs + H_2O.$$

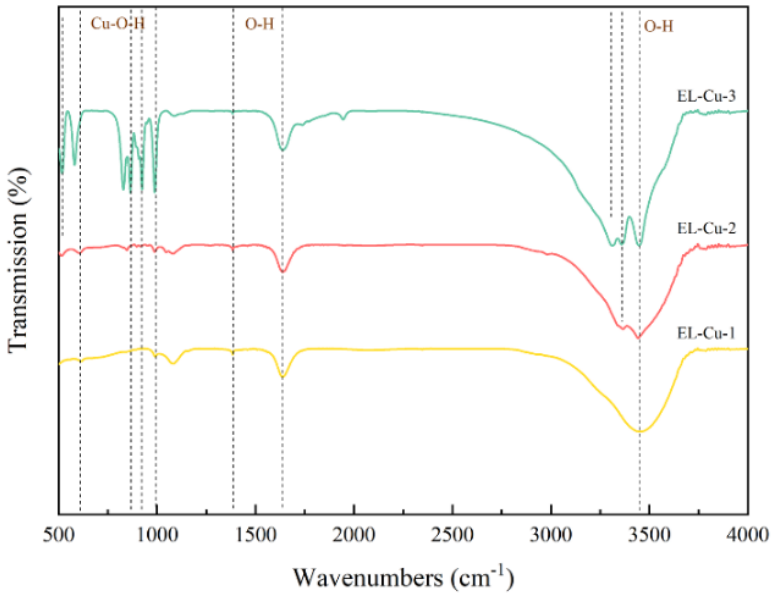

Figure 4.2. FTIR spectra of prepared EL-Cu-x materials.

Table 4.1. Physical properties of EL-Cu-*x* materials.

Sample name	S_{BET} (m^2/g)[b]	V_t(cm^3/g)[b]
EL-Cu-1	14.046	0.0275
EL-Cu-2	32.443	0.0675
EL-Cu-3	2.262	0.0065

[b] Specific surface area, pore volume, and average pore sizes determined via N_2 adsorption-desorption isotherm measurements.

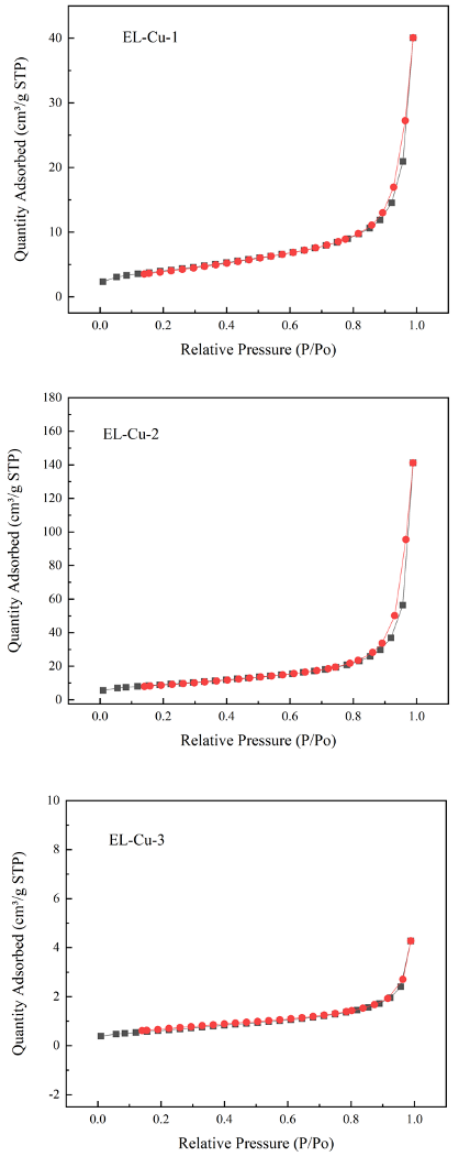

Figure 4.3. N2 adsorption-desorption isotherms for the EL-Cu-x samples.

The porous network of hierarchical EL-Cu-*x* structures were investigated using nitrogen adsorption/desorption isotherms (**Figure 4.3**). According to the N_2 adsorption-desorption isotherm analysis, the specific surface area calculated by the Brunauer–Emmett–Teller (S_{BET}) method was gradually increased with Cu doping (**Table 4.1**). The EL-Cu-1, EL-Cu-2 and EL-Cu-3 feature type IV isotherms with a H_2-type hysteresis loop for typical mesocage materials with large pore cavities. However, EL-Cu-3 show type II isotherms without any hysteresis loops. Irrespective of the Cu loading, the measured Brunauer–Emmett–Teller (BET) specific surface area (SSA) was enhanced to a maximum of 32.443 $m^2 g^{-1}$ with a pore volume of 0.0675 cm^3/g at EL-Cu-2 and dropped to 2.262 m^2/g at EL-Cu-3(**Table 4.1**). Such control of hierarchical surface morphologies with well-developed porous network could fasten the ions transport on the surface of the electrode.

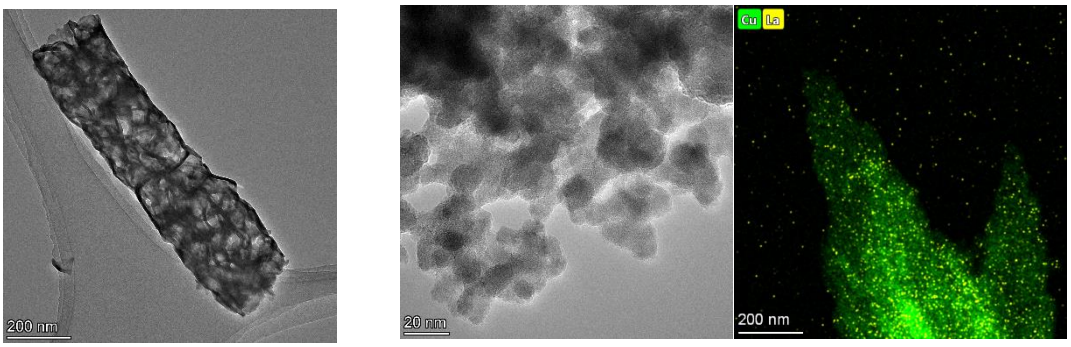

Figure 4.4. Morphology and surface characteristic via FE-TEM images and EDS elemental mapping of EL support and EL-Cu-2 catalysts.

The as-prepared EL support and EL-Cu-2 samples were characterized by FE-TEM. As shown in **Figure 4.4**, the EL support catalysts show disordered honeycomb-like macroporous structure resulting from the release of a large amount of gas produced by the low-temperature oxidation of EG to the glyoxylate dianion in aqueous solution and the thermal decomposition of metal glyoxylates during the preparation. As for the EL-Cu-2 sample, the morphology has shown the macroporous structure covered by multiple agglomerations of nanoparticles.

4.3.2 Electrocatalytic performance of CO_2 reduction

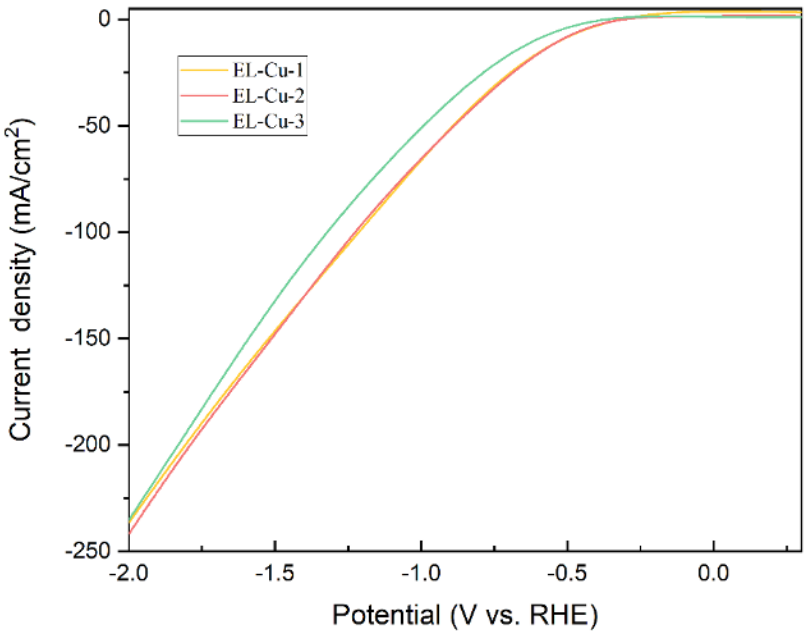

Figure 4.5. Linear sweeping voltammetry (LSV) curves of EL-Cu-x modified electrodes at various reaction times in a 0.5 M $KHCO_3$ solution at a scan rate of 100 mV/s.

For evaluating the CO_2 electroreduction performance of the samples, a typical three-electrode H-type cell containing CO_2-saturated or N_2-saturated 0.5 M $KHCO_3$ water solutions was employed in this work. LSV curves on EL-Cu-x decorated glass carbon electrode were gained via sweeping the potential ranging from –2 V RHE to 0.6V vs. RHE at a sweep rate of 100 mV s^{-1} (**Figure 4.5**). Remarkably, EL-Cu-2 sample showed the highest current density with most negative onset potential. In addition, the Nyquist plots shown in **Figure 4.6** revealed that the EL-Cu-2 composite had a ten-fold resistance reduction in the equivalent circuit, which suggested that a lowest charge-transfer resistance.

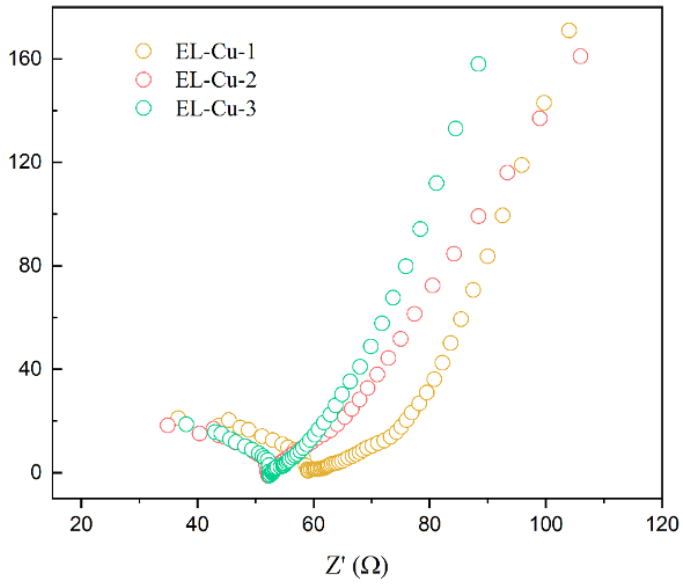

Figure 4.6. Electrochemical impedance spectroscopy (EIS) spectrum for EL-Cu-x decorated electrodes.

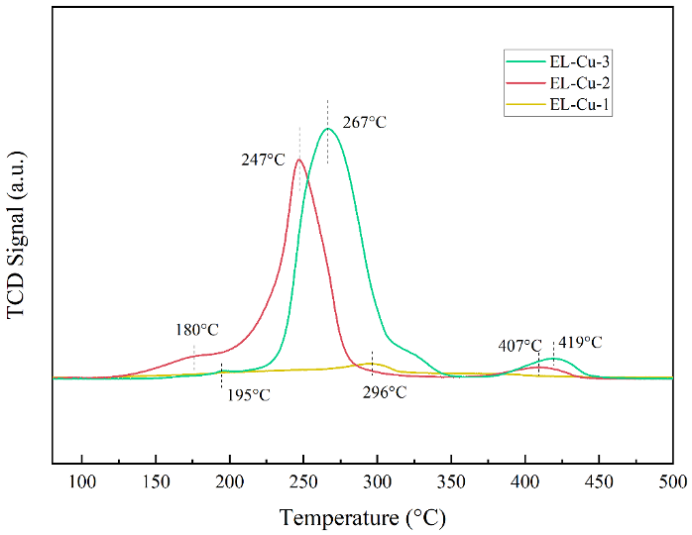

Figure 4.7. CO-TPD profiles of EL-Cu-x samples.

Table 4.2. The peak intensities quantified in the CO-TPD patterns.

Samples	Temperature at maximum (°C)	Quantity (cm^3/g STP)
EL-Cu-1	296	54.2
	348	10.5
EL-Cu-2	180	108.8
	247	383.3
	407	31.5
EL-Cu-3	195	12.6
	268	651.8
	415	47.1

For the formation of C_2H_4, the selectivity-determining step is the generation of the *COH intermediate by protonation of *CO and the subsequent converting into $*CH_2$ intermediate, which can further produce C_2H_4 via a nonelectrochemical $*CH_2$ dimerization.[2] To further investigate the nature of adsorbed and activated *CO species involved in the CO_2RR, the temperature-programmed desorption (TPD) experiments were carried out to explore the capability of these samples for CO adsorption (i.e., CO-TPD, **Figure 4.7**). In addition, **Table 4.2** summarizes the different CO binding sites quantified analysis results. CO-TPD profiles confirmed the existence of three forms of chemisorbed CO species, and the bonding strength increased in the following order: CO^L (linear) < CO^B (dicoordinated bridging) < CO^H (triple-coordinated bridging). [] After deconvolution, the regions are mainly located at 350-400, 500-700, and 600-800 K. Considering the bonding strength order, these three ranges, from low to high temperature, can be assigned to CO^L, CO^B, and CO^H, respectively. The EL-Cu-2 sample shows the lowest temperature of CO^L, CO^B, and CO^H desorption peaks among the three samples which explains it has highest Faradic efficiency of CO (23.7 % at 1.1V). Moreover, the peaks at 100 °C and 200 °C is also corresponded to the external surface and inner surface adsorption between CO reactant and sample, respectively. []As for the desorption peak at about 200 °C, it is related to the inner surface and the C_2 selectivity can be promoted via enhancing C–C formation in inner surface, benefitting from the localized high-concentration of ∗CO. The EL-Cu-2 has

highest CO desorbed amount (108.8 cm^3/g STP) at 180 °C compared with EL-Cu-3 (12.6 cm^3/g STP) at 195 °C.

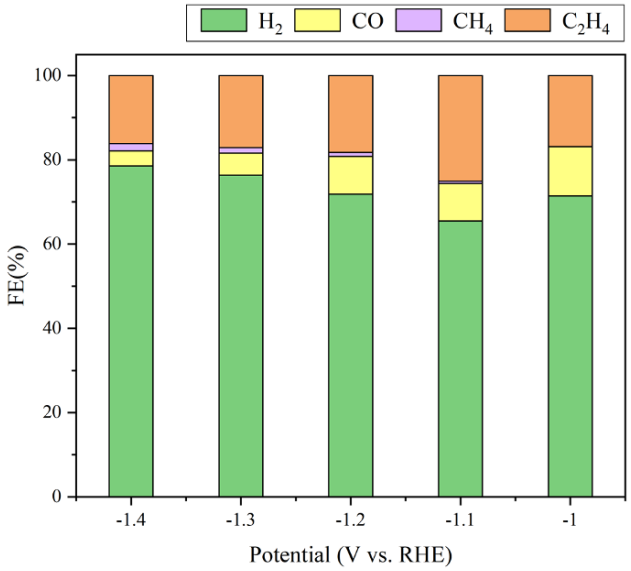

Figure 4.8. Faradic efficiency of EL-Cu-x catalyzed CO_2RR at different potentials: EL-Cu-1

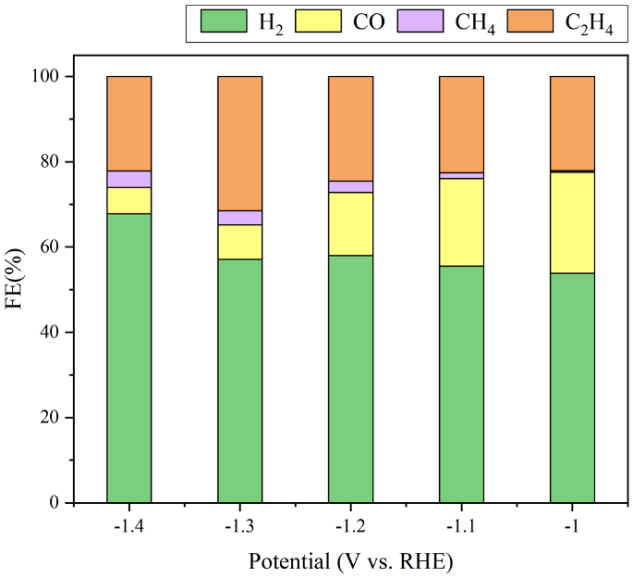

Figure 4.9. Faradic efficiency of EL-Cu-x catalyzed CO_2RR at different potentials: EL-Cu-2

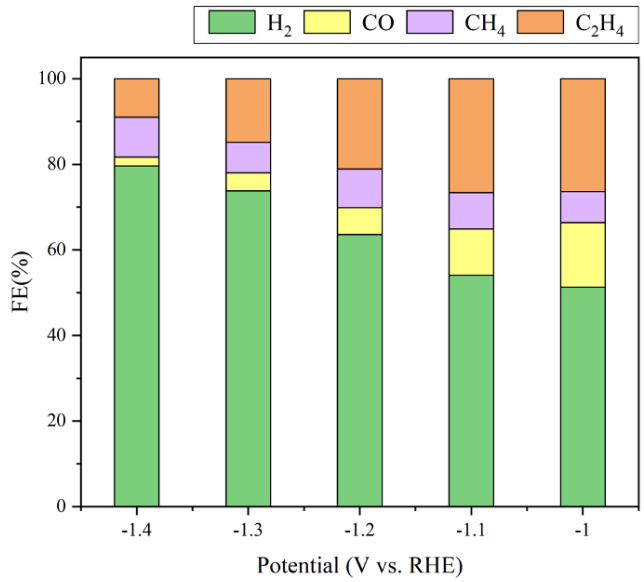

Figure 4.10. Faradic efficiency of EL-Cu-x catalyzed CO_2RR at different potentials: EL-Cu-3

The detailed Faradaic efficiencies for all products at various potentials are shown in **Figure 4.8, Figure 4.9** and **Figure 4.10.**Overall, the fragmented EL-Cu-x exhibited the highly enhanced CO_2RR catalytic activity with suppressed HER, compared to the $ZnO/La_2O_2CO_3$ catalysts. The chronoamperometry (CA) experiments were performed at different potentials for each 10 min, and gaseous products were determined by GC. Among all the EL-Cu-x samples, the main gaseous products are CH_4, C_2H_4, CO and H_2. C_2H_4 is a dominant carbonaceous product at low potential. A maximum of the ethene FE 25%) for EL-Cu-2 is achieved at −1.3 V (vs RHE), which is consistent with its largest surface area. The superior electrocatalytic activity of HL-12h to PL-12h would result from the better CO adsorption ability at 200°C which can optimize the C-C coupling, which is then converted to C_2H_4. The higher electrical conductivity also leads to its highest FE_{C2H4}.

4.4. Conclusions

In this study, EL-Cu-*x* series catalysts were well prepared by hydrothermal method and the main phase of copper was converted from CuO to $Cu_2(OH)_3Cl$ with the increasing content of

copper precursor. The EL-Cu-2 sample shows the highest BET surface (32.443 m^2/g), explained its best activity towards CO_2RR. The CO-desorption peak at about 200°C is related to its inner surface adsorption and the C-C coupling usually happened on the inner surface. The EL-Cu-2 has highest CO adsorption at 180°C which is on consistent with its highest FE_{C2H4}= 25% achieved at -1.3V vs. RHE.

Chapter 5. Copper composite supported by carbon in CO_2RR

5.1. Introduction

Compared to all conversion paths, electrocatalytic reduction appears to be the most realizable as it can be carried out under ambient conditions with a relatively controllable reaction step and promising conversion efficiency, which can be driven by renewable energy. [196-197] The CO_2RR system is remarkable because: (1) it neutralizes carbon in the atmosphere, (2) it provides an alternative to non-renewable energy and (3) it can synthesize industrial chemicals and fuels. Moreover, the society should decrease its dependency on conventional fossil fuels, or a crisis will exist in the materials and petrochemical industries. If the petroleum feedstock can be produced from CO_2 reduction, then it can be potentially implemented into conventional downstream industries directly. The catalysts which can electrochemically reduce CO_2 efficiently should meet the following conditions: low activity in the competing HER, suitable binding strength of CO with the catalyst surface, promising selectivity and activity toward CO_2 electroreduction, and long-term stability.[198] In recent years, nanostructured carbon-based materials have received much attention in the research fields of nanomaterials, and have been widely applied for energy conversion, such as water splitting reaction. The superiority of carbon materials in this area is its extremely high surface area, allowing compositional fine tuning, heteroatom doping and structural fine tuning, which have excellent conductivity. Being metal-free materials, they also can help to reduce the usage of metals in these technologies, which is environmentally friendly. For the CO_2RR and other processes, carbon based electrocatalysts and supports have proved to be very stable and efficient in reaction. [199-202] Whatever employed as totally metal free or as carbon-metal composites, it is necessary to develop efficient carbon-based material can potentially realize energy storage/conversion devices for mainstream applications.

5.2. Materials and analysis technologies

5.2.1. Preparation of catalysts

Carbon spheres (CSs) were prepared by the hydrothermal treatment of 20 g of anhydrous glucose dissolved in 180 mL of ultrapure at 180 °C for 9 h, and then it was dried at 80 °C for 6 h after centrifugation and washing. CuO nanosheets were synthesized in a high concentrated alkaline solution. 1.2 mL of 0.05 M, 0.1 M, 0.2 M $CuCl_2$ aqueous solution was dropwise added into 4.0 mL of carbon support aqueous solution (concentration, 1.0 mg/mL) and stirred for 2 h. Then, 1.8 mL of 2 M NaOH solution was slowly added into the mixture to get a suspension. The solution was vigorously stirred and then transferred into a Teflon-lined autoclave, sealed and heated at 100 °C for 10 h. The system was allowed to cool to room temperature naturally and the resulting product was centrifuged, rinsed with distilled water and ethanol several times to remove any alkaline salt and then dried in a vacuum oven at 60 °C for 12 h. The CuO nanosheet electrode was via in situ CO_2 electro-reduced at -2 V (vs RHE) from after an initial electrolysis running for 30 min. The catalysts were named as CSs-Cu, CNT-Cu, GO-Cu, AC-Cu.

5.2.2. Characterization

Field-emission scanning electron microscopy (FE-SEM; JSM-600F) and high-resolution transmission electron microscopy (HR-TEM; JEM-2100F) were used to study the morphologies of photocatalysts. Samples were cast onto carbon-coated Cu grids before analysis. Crystalline structures were determined via X-ray diffraction (XRD) with a Rigaku D/MAZX 2500V/PC high-power diffractometer utilizing a Cu Kα X-ray source with a wavelength of 1.5415Å and a scanning rate of 2° (2θ) min^{-1}. Functional groups of the catalysts were verified with a Nicolet 380 Fourier transform infrared (FTIR) spectrometer (Thermo Scientific Nicolet iS5 with an adopted iD1 transmission accessory). The specific surface area and other porosity characteristics were measured via N_2 adsorption isotherm processes using a Micromeritics ASAP 2020 instrument. A Thermo Scientific K-Alpha X-ray photoelectron spectroscopy (XPS) system was applied to measure the elemental composition empirical formula, chemical state, and electronic state of the elements in a material. The absorbance of photons was investigated via UV-visible diffuse reflectance (UV-Vis-DRS; SPECORD 210 Plus spectroscope). The recombination rate

of charges was measured by a Cary Eclipse fluorescence spectrophotometer (PL; Agilent Technologies) at room temperature with a 473 nm diode laser.

5.2.3. Electroreduction reactions

To prepare the working electrode, 2 mg of the as-prepared catalyst were dispersed into a mixture solution of 100 μL ethanol and 5 μL of 5.0 wt% Nafion. The solution was homogeneously mixed to get the final uniform catalyst ink by bath-sonication. The uniform ink was then dropcast onto a glass carbon electrode with an diameter of 3 mm and naturally dried. The electrochemical experiments were performed in a gas-tight H-type electrochemical cell and the Nafion-117 proton exchange membrane was used to separate the cathodic and anodic compartment. The working electrode and reference electrode (Ag/AgCl) were mounted in the cathodic compartment while the counter electrode of Pt was placed in the anodic side. For both cathodic and anodic sides, 30 mL of 0.5 M $KHCO_3$ solution was added as the electrolyte. The 0.5 M $KHCO_3$ solution was pre-saturated with CO_2 (pH = 8.81). During the measurement, CO_2 or at a rate of 20 sccm was continuously bubbled into the solution to keep the saturation of the electrolyte. The potentials (vs. SCE) were transformed to reversible hydrogen electrode (RHE) potential for the final performance characterization. Before the CO_2 electroreduction measurements, the as-prepared catalysts were first reduced t applying a biased potential of -2 V (vs. RHE) for 30 mins.

5.3. Results and discussions

5.3.1. Morphology and structural properties

Crystalline phases of the C/Cu materials were determined from X-ray diffraction patterns, as shown in **Figure 5.1**. With all the copper catalysts supported by carbon show the main phase of copper oxide (PDF# 02-1040) and copper monoxide (PDF# 77-0199). However, it should be

noted that the feature carbon peaks at 25.7^{O} and 44.5^{O} related to (100/101) Bragg reflections were only detected with the AC-Cu sample.

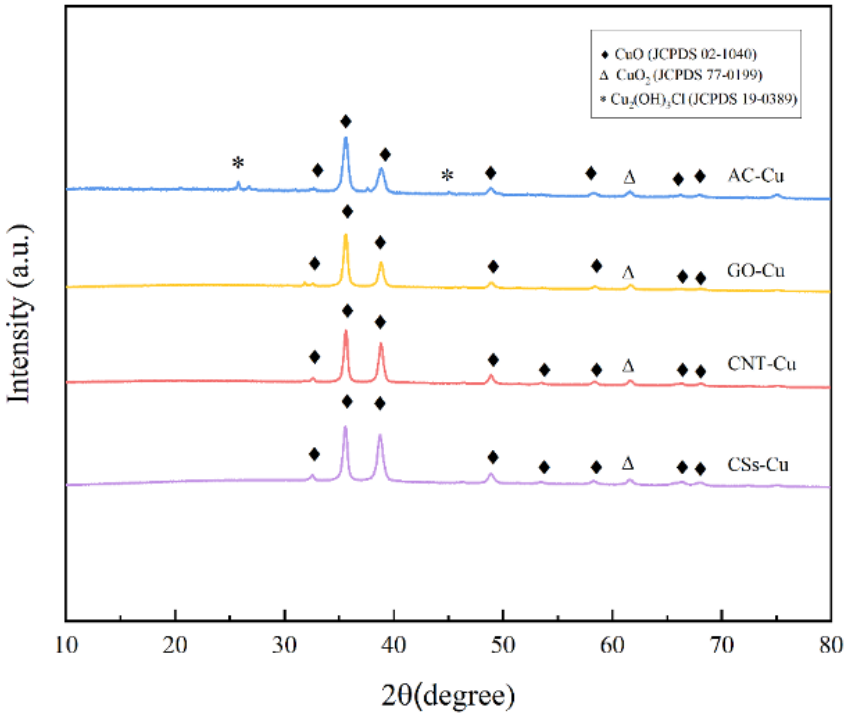

Figure 5.1. XRD patterns of C-Cu materials.

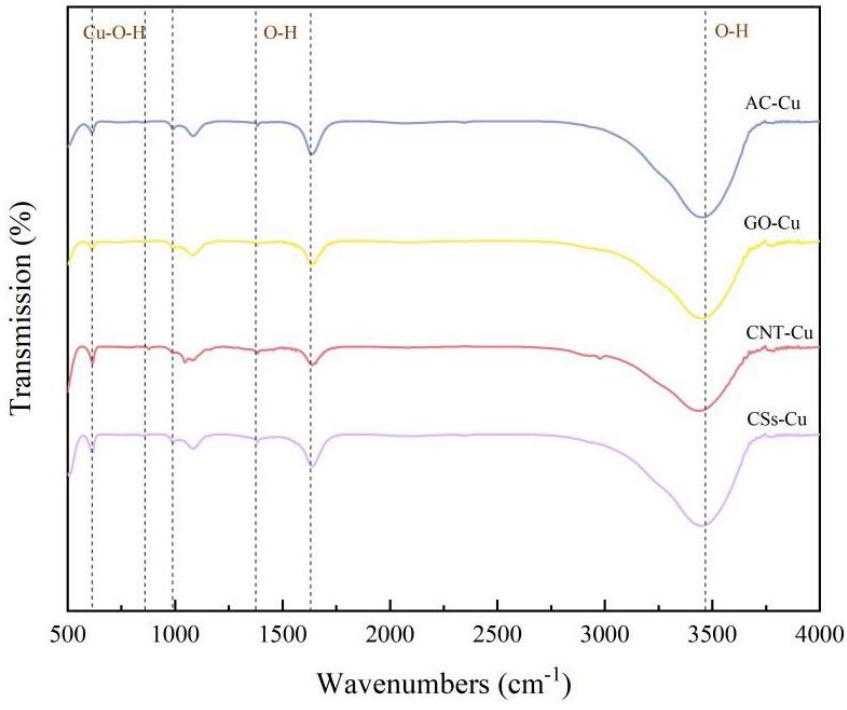

Figure 5.2. FTIR spectra of prepared C-Cu materials.

Fourier transform infrared (FTIR) spectra of the C-Cu samples can be seen in **Figure 5.2**. According to the general spectrum analysis method, the observed IR absorption may be readily attributed to the OH-related modes, Cu−O-related modes, Cu−Cl related modes, and lattice modes as well as their sum/ difference/overtones. 37−40 In the high-frequency region typical of functional groups, the IR bands at 3306, 3365, 3449 cm^{-1} can be assigned as the stretching modes of the hydroxyl groups (v_{O-H}). They correspond to the two types of OH environments with different atomic distances (d_{O-H}) and hydrogen bond angles ($\theta_{O-H\cdots Cl}$). In fact, in the $(O-H)_3\cdots Cl$ interlayer trimeric hydrogen bond, two hydroxyl groups are crystallographically equivalent and the third is not, thus giving rise to the appearance of two vibrational frequencies of v_{O-H} stretching. The IR bands at 1386, 1637 cm^{-1} may be caused by the residual water in the KBr discs and/or the deformation modes of dangling OH groups on the surface. The residual stresses in the KBr discs and large LO-TO splitting effects may contribute to the enlarged bandwidth and the poorly defined spectroscopic profile. The IR bands at 867, 921, 993 cm^{-1} can be assigned to the Cu−O−H deformation modes (δCu−O−H). However, due to the combination of accidental degeneracy, Davydov splitting, and the existence of sum/ difference/overtones, an exact assignment is very difficult in this 1100-600 cm^{-1} window region.

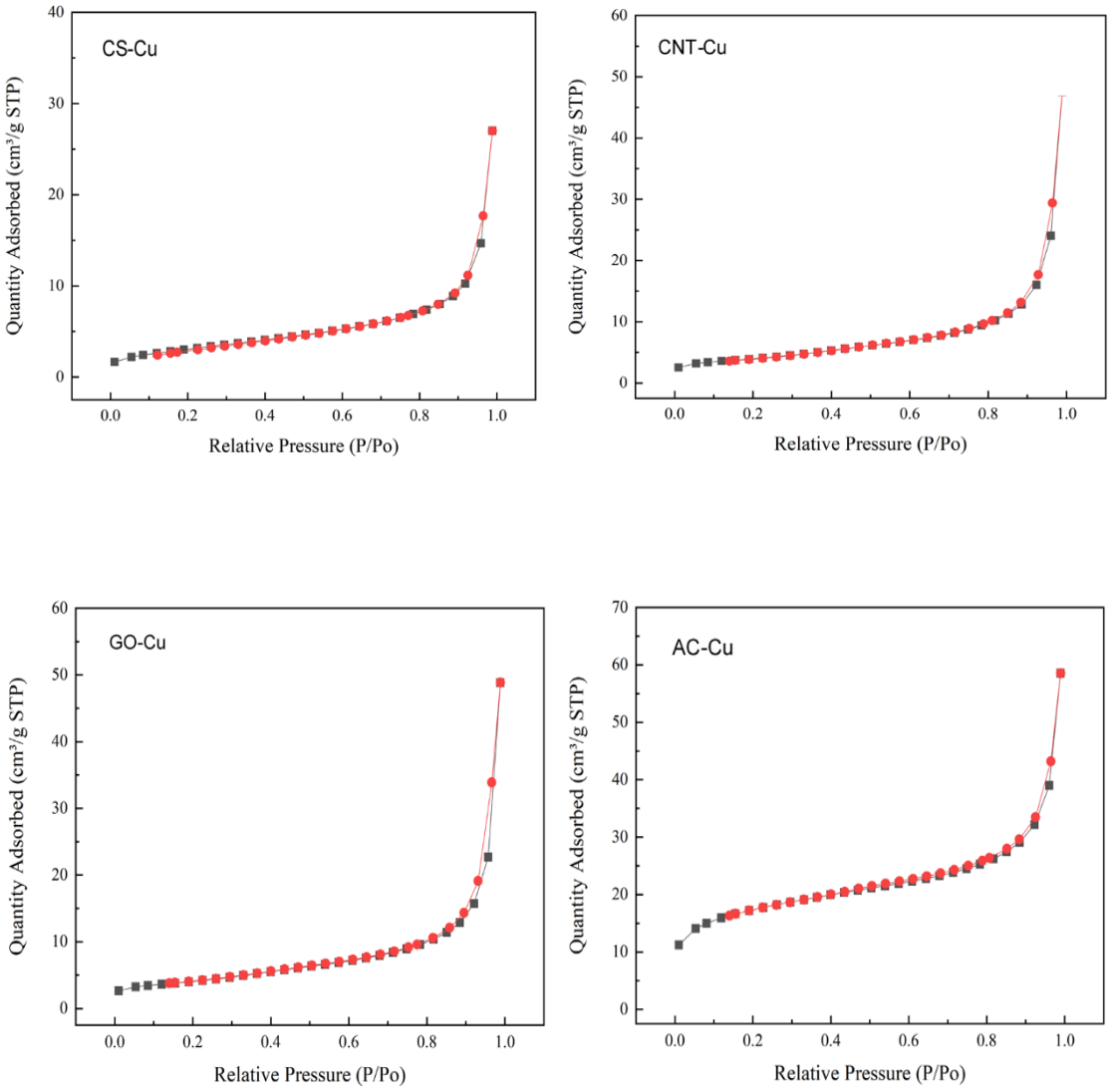

Figure 5.3. N_2 adsorption-desorption isotherms for the C-Cu samples.

Table 5.1. Physical properties of EL-Cu-*x* materials.

Sample name	$S_{BET}(m^2/g)^b$	$V_t(cm^3/g)^b$
CSs-Cu	11.2957	0.0422
CNT-Cu	13.9627	0.0732
GO-Cu	14.4274	0.0752
AC-Cu	57.7328	0.0755

The porous network of hierarchical C-Cu structures was investigated using nitrogen adsorption/desorption isotherms (**Figure 5.3**). According to the N_2 adsorption-desorption

isotherm analysis, the specific surface area calculated by the Brunauer–Emmett–Teller (S_{BET}) method was various with different carbon supports (**Table 5.1**). The CSs-Cu, CNT-Cu and GO-CU feature type V isotherms with a H_3-type hysteresis loop resulted from weak interaction between N_2 and samples. However, AC-Cu show type IV isotherms with H_3-type hysteresis loop for its mesoporous structure. Irrespective of the Cu loading, the measured Brunauer–Emmett–Teller (BET) specific surface area (SSA) was enhanced to a maximum of 57.7328 $m^2\ g^{-1}$ with a pore volume of 0.0755 cm^3/g at AC-Cu (**Table 5.1**). Such control of hierarchical surface morphologies with well-developed porous network could fasten the ions transport on the surface of the electrode.

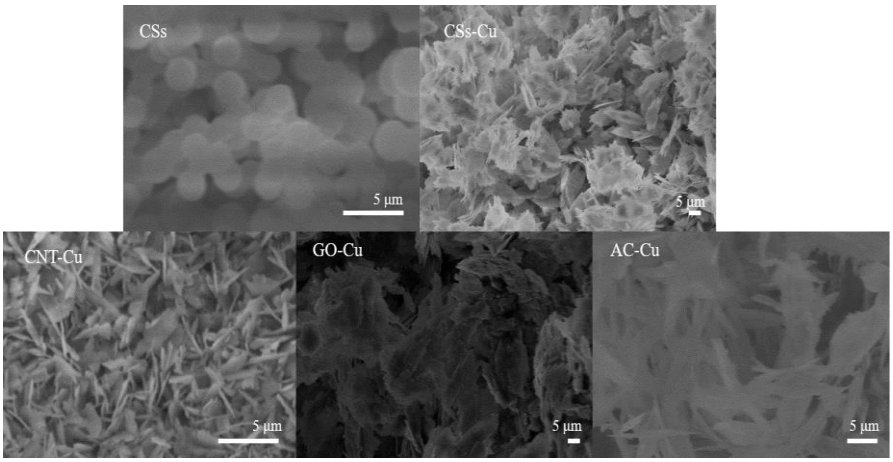

Figure 5.4. SEM images of C-Cu materials.

The as-prepared CSs support and C-Cu samples were characterized by SEM. As shown in Figure 5.4, the CSs support has orbicular morphology with an identical diameter of approximately 385nm. As for the CSs-Cu sample, the morphology has shown the carbon spheres and multiple agglomerations of nanosheets. As for the CNT-Cu, the carbon nanotubes mix with nanosheets while the GO-Cu shows layer structure of nanosheets. In addition, the AC-Cu sample shows uniform extreme thin nannosheets.

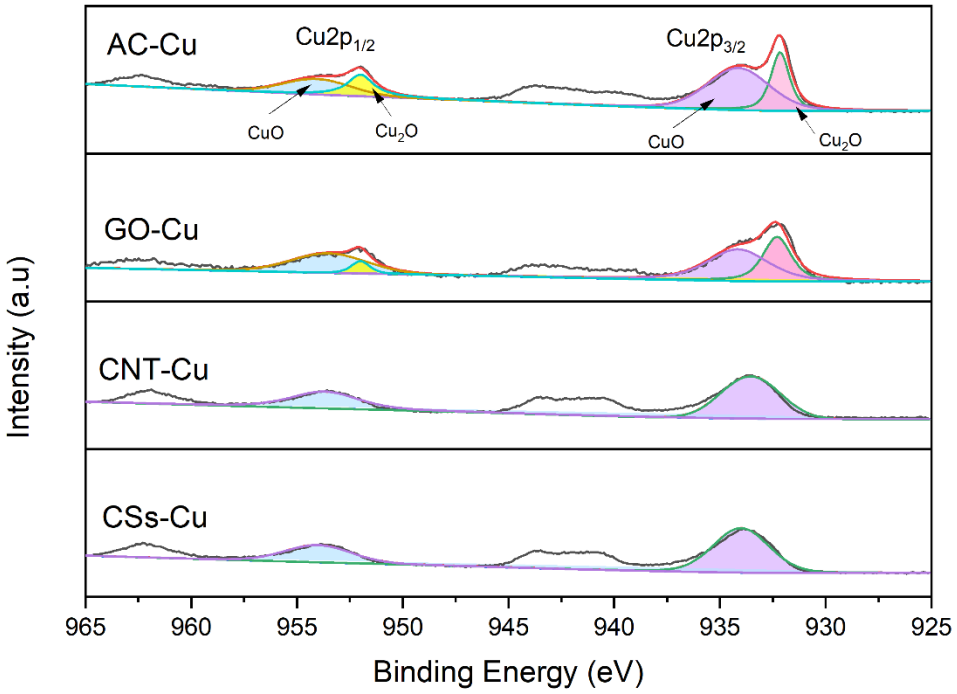

Figure 5.5. Cu 2p XPS spectra of C-Cu samples.

Furthermore, a XPS study has been carried out to properly evaluate the Cu oxidation state at the surface layer. Figure 5.5 shows the high resolution Cu 2p XPS spectra obtained for the Cu oxides supported by carbon. The characteristic doublet peaks corresponding to Cu $2p_{1/2}$ and Cu $2p_{3/2}$ at about ~954 eV and ~933 eV, respectively, and their shake-up stellite structures, are clearly observed. The analysis of AC-Cu and GO-Cu contributions at 932.3 eV and 952.2 eV which are related to the presence of Cu_2O. Interestingly, another two samples have shown CuO peaks, which implies the coexistence of CuO and Cu_2O can promote to form C_2H_4.

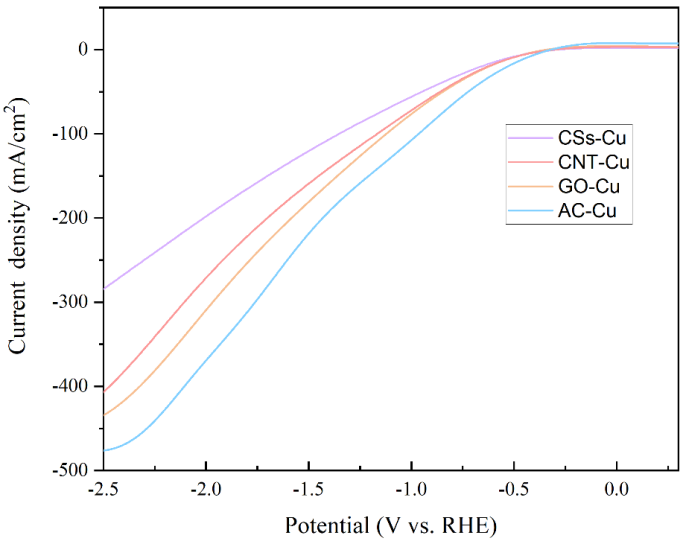

Figure 5.6. Linear sweeping voltammetry (LSV) curves of C-Cu decorated electrodes at various reaction times in a 0.5 M $KHCO_3$ solution at a scan rate of 100 mV/s.

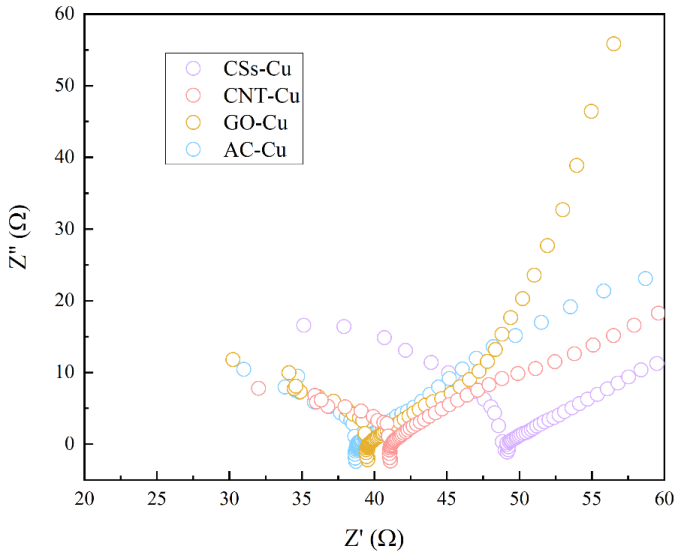

Figure 5.7. Electrochemical impedance spectroscopy (EIS) spectrum for C-Cu decorated electrodes.

For evaluating the CO_2 electroreduction performance of the samples, a typical three-electrode H-type cell containing CO_2-saturated or N_2-saturated 0.5 M $KHCO_3$ water solutions was employed in this work. LSV curves on C-Cu decorated glass carbon electrode were gained via sweeping

the potential ranging from –2 V RHE to 0.6V vs. RHE at a sweep rate of 100 mV s^{-1} (**Figure 5.5**). Remarkably, AC-Cu sample showed the highest current density with most negative onset potential. In addition, the Nyquist plots shown in **Figure 5.6** revealed that the AC-Cu composite had lowest resistance reduction in the equivalent circuit, which suggested that a lowest charge-transfer resistance. Both of the two electrical techniques imply the AC-Cu has the best electrical response towards to CO_2.

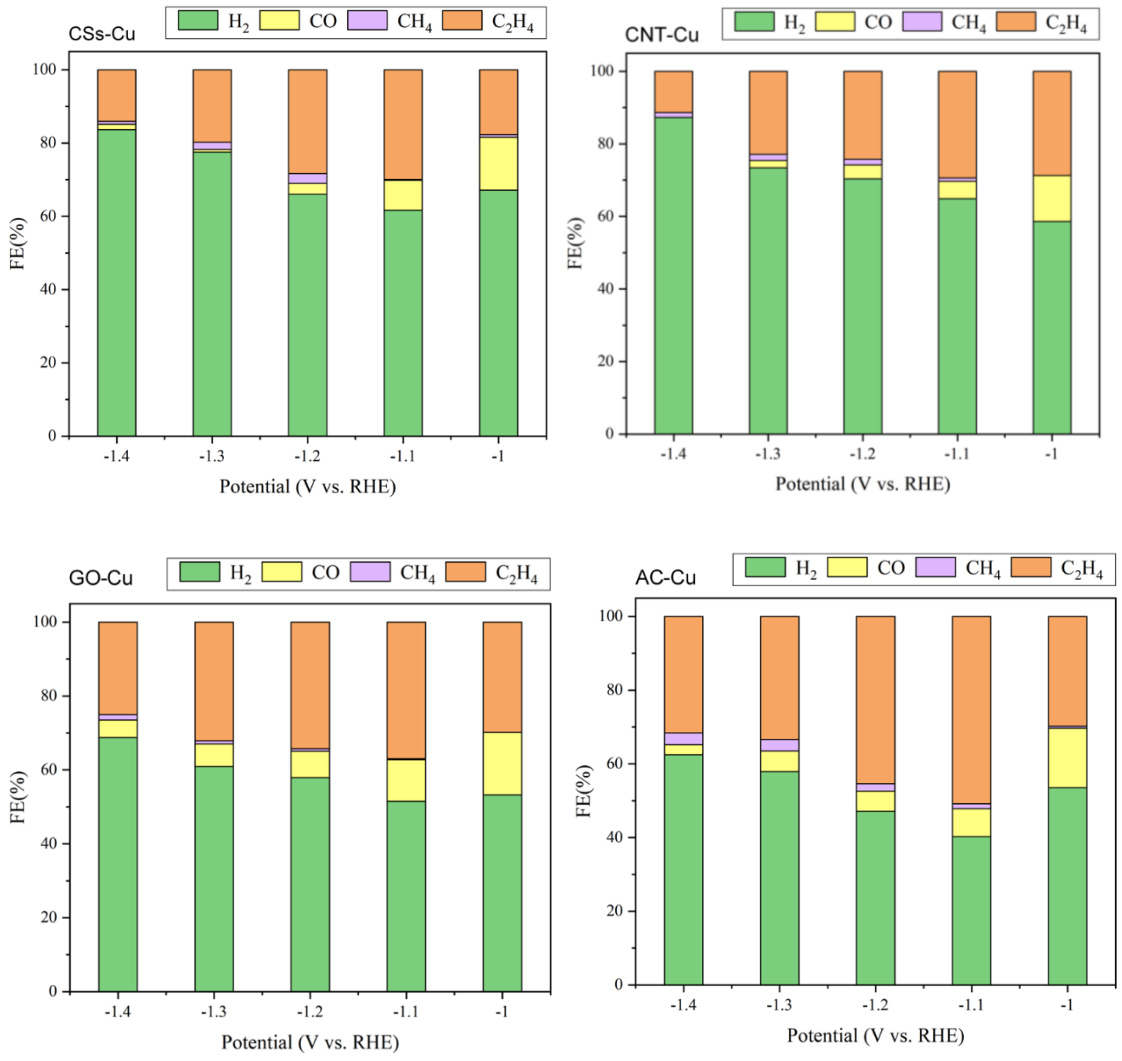

Figure 5.8. Faradic efficiency of C-Cu catalyzed CO_2RR at different potentials.

The faradic efficiencies were evaluated by faradic equation and the results were shown in **Figure 5.7**. The dominant product of all the C-Cu catalysts were ethylene from the range of FE_{C2H4} 25% - 50%, which resulted from the coexistence of both Cu (0) and Cu(I). The BET surface areas greatly influence the CO_2 involved catalytic performance result in more CO_2RR products formed when the HER reaction is suppressed. Moreover, the optimal electrical conductivity of AC-Cu also determined its excellent CO_2 electro-catalytic performance. It is believed that there are synergistic effects between Cu (I) and Cu (II) and the mechaniam illustration is proposed as below:

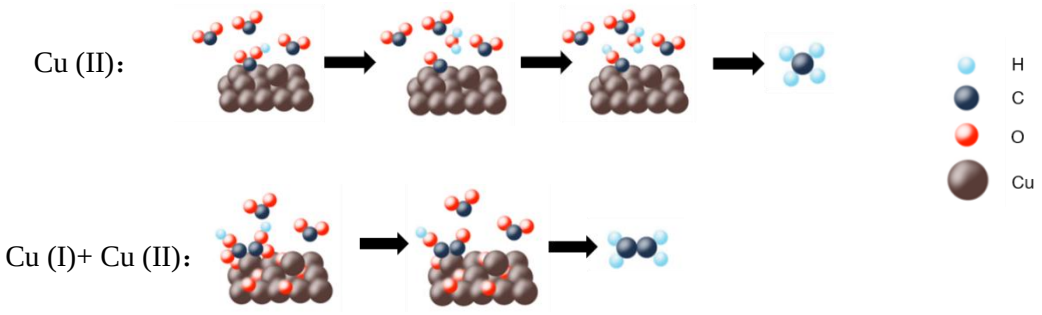

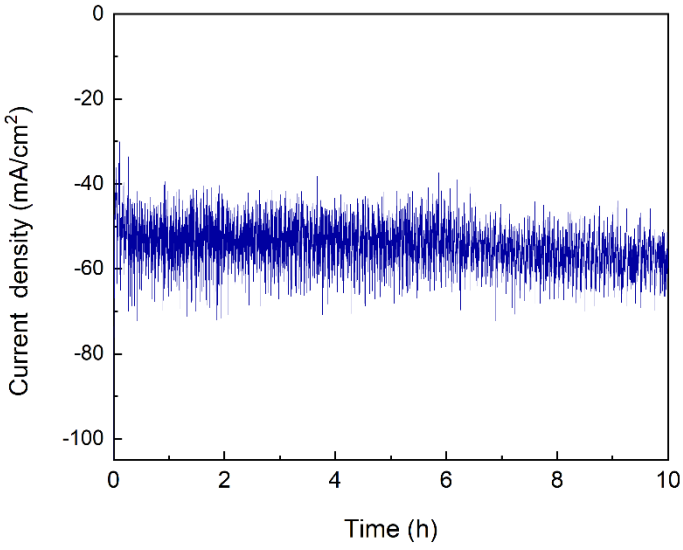

Figure 5.9. Current density stability of AC-Cu over 10 h.

To further study the catalytic stability of AC-Cu catalyst, long-term electrolysis of CO_2 tests was carried out at -1.1 V vs. RHE for 10 hours. Figure 5.9 does not display a visible change in the current density over 10 hours of electrolysis, indicating its good stability.

Table 5.2. Kinds of representative Cu-based catalysts used to produce C_2H_4 products in ECR in recent years.

Catalyst	**Preparation method**	**Main C_2 product, FE**	**Environment (vs. RHE)**	**Stability**	**Conclusive remarks**	**Ref.**
Cu(B)	Precipitation	C_2H_4, 52.5%	At-1.1 V, in 0.1 M KCl	40 h	Adjust Fermi level, reduce coupling energy	[201]
Cu NDs	Precipitation	C_2H_4, 22.3%	At-1.2 V, in 0.1 M $KHCO_3$	7 h	High ECSA, efficient electron/mass transfer	[202]
Multi-hollow Cu_2O	Precipitation	C_2H_4, 38.0 ± 1.4%	At-0.61 V, in 2 M KOH	3 h	Increase and stabilize CO adsorption	[203]
44 nm Cu nanocube	Wet chemical	C_2H_4, 41.0%	At-1.1 V, in 0.1 M $KHCO_3$	1 h	Balance between plane and edge sites for reaction	[204]
4H/fcc Au@Cu	Wet chemical	C_2H_4, 46.7%	At-1.17 V, in 0.1 M $KHCO_3$	9 h	Lower Gibbs energy of COOH	[205]
Cu--on--Cu_3N	Wet chemical	C_2H_4, 39.0 ±2%	At-0.95 V, in 0.1 M $KHCO_3$	15 h	Protection of active species	[206]
ERD Cu	Wet chemical, electrochemical	C_2H_4, 36.0%	At-1.0 V, in 0.1 M KHCO3	1 h	Sharper structures im-prove current densiti-es and local pH	[207]
Reconstructed Cu	Wet chemical, electrochemical	C_2H_4, 56.0%	At-1.4 V, in 0.05 M $KHCO_3$	–	Increase surface active sites	[208]
F-Cu	Solvothermal, electrochemical	C_2H_4, 65.2%	At-0.89 V, in 0.75 M KOH	40h	Accelerate H_2O dissociation and electron transfer	[209]
Cu_2O thin films	Solvothermal, electrochemical	C_2H_4, 31.0%	At-0.98 V, in 0.1 M $KHCO_3$	70min	Efficient CO adsorption with small nanoparticle	[210]
HPR-LDH	Precipitation, electrochemical	C_2H_4, 36.3%	At-1.1 V, in 0.1 M $KHCO_3$	20h	High ECSA, efficient charge transfer	[211]

CuOx-Vo	Thermal treatment, electrochemical	C_2H_4, 63.0%	At-1.4 V, in 0.1 M $KHCO_3$	13h	Facilitate the adsorption of *CO, *COH intermediates	[212]
3D porous CuO	Thermal treatment, electrochemical	C_2H_4, 39.3%	At-0.65 V, in 1 M KOH	2 h	Rapid gas transport	[213]
Cu np1 20	Thermal treatment, electrochemical	C_2H_4, 35.0%	At-1.3 V, in 0.1 M $KHCO_3$	8h	High ECSA, expose low-coordinated steps and edges	[214]
Plasma-activated	Plasma treatment,	C_2H_4, ~45%	At-1.0 V, in 0.1 M $KHCO_3$	5h	Regeneration of active species	[215]
30/70 Cu Mesopore	Sputtering, electrochemical	C_2H_6, 46.0%	At-1.3 V, in 0.1 M $KHCO_3$	4h	Prolongation of reaction time	[216]
Cu_3N-D Cu NWs	CVD, electrochemical	C_2H_4, 66.0%	At-1.0 V, in 0.1 M $KHCO_3$	28h	Abundant grain boundaries	[217]
CSNP	Electrospray	C_2H_4, 48.7%	At-1.0 V, in 0.1 M $KHCO_3$	20h	Suppress H_2 evolution	[218]
Cu mesocrystal	Electrochemical	C_2H_4, 27.2%	At-0.99 V, in 0.1 M $KHCO_3$	6h	Increase and stabilize CO adsorption	[219]
100-cycle Cu	Electrochemical	C_2H_4, 32.0%	At-0.96 V, in 0.25 M $KHCO_3$	2h	Expose Cu (100)	[220]
$CuCO_3$	Electrochemical	C_2H_4, ~47%	At-0.95 V, in 0.1 M $KHCO_3$	22h	High ECSA, low-coordinated sites	[221]
CuDAT-wire	Electrochemical	C_2H_4, ~40%	At-0.5 V, in 1 M $KHCO_3$	8h	low-coordinated steps and edges	[222]
GB-Cu	Electrochemical	C_2H_4, ~38%	At-1.2 V, in 1 M KOH	3h	Increase and stabilize CO adsorption	[223]
HPR-Cu	Electrochemical	C_2H_4, 38.1%	At-1.08 V, in 0.1 M $KHCO_3$	40h	Abundant oxygen state of the Cu	[224]
Prism-shaped Cu	Electrochemical	C_2H_4, 27.8%	At-1.1 V, in 0.1 M $KHCO_3$	12h	Modification of the local pH	[225]
CuAg-wire	Electrochemical	C_2H_4, ~60%	At-0.7 V, in 1 M KOH	–	Inhibit reduction of active species	[226]

AC-Cu	Electrochemical	C_2H_4, ~50.8%	At-1.1 V, in 0.5 M $KHCO_3$	10h	High surface area and Abundant oxygen state of the Cu	This work

Table 5.2 summarized the representative works in recent years related to Cu-based catalysts in ECR with C_2H_4 products and the research result in this study. The performance of each catalyst in ECR was introduced, including the highest C_2 product and Faraday efficiency, as well as maximum stability verified by experiments. The design strategy and conclusive remarks are also summarized.

5.4. Conclusions

In summary, four kinds of carbon support were adopted to prepare the CuO/C catalysts. The BET surface area in the following order: AC-Cu > GO-Cu > CNT- Cu > CSs- Cu which is consist with the CO_2RR catalytic performance. The highest FE_{C2H4}= 50.8 % of CuO/C was achieved by AC-Cu at -1.2 V vs. RHE possibly own to its highest surface area and lowest impedance. From the ex-situ surface analysis by XRD, XPS, and XANES, it was found that C_2H_4 production was favored on the catalysts containing mixed oxidized copper species along with high oxygen content. These results show the relation between the durability of ethylene production and Cu-O containing surface states. This will provide new strategies to control the selectivity and durability of O-Cu combination catalysts for electrochemical CO_2 conversion to value-added chemicals.

SUMMARY

In summary, this research is based on the idea of developing a highly efficient electrocatalyst based on three key factors:

- High surface area which can benefit the adsorption of CO_2.
- Optimal electrical conductivity.
- Strong adsorption with CO on the inner surface for C-C coupling.

We systematically investigated the chemical-physical properties of copper oxide-based electrocatalysts and their applications in electrocatalytic reduction of carbon dioxide. Basic characterizations were carried out by XRD, FTIR, FE-SEM and HR-TEM to determine the phase composition and their morphology in materials. One of the important properties of Faradic efficiency, current density, were evaluated by CA and LSV electro-techniques. The interactions between different components within the materials were identified by XPS core level spectra. Finally, electrocatalysts are applied in the CO_2 electrochemical reduction reaction and check their adsorption capacity as well as electrocatalytic performance.

RECOMMENDATIONS FOR FUTURE WORK

In this study, we investigated various preparation methods in developing La-based and Cu-based catalysts for electrochemical reduction of CO_2 to C^{2+} products. although electrolysis cell, electrolyte, and reduction process conditions are some research focuses for CO_2 reduction, determining a suitable electrode is one of the significant points to be considered. promising rather than using a bulk metal electrode. The catalytic activity could be improved by depositing or modifying the carbon surface with metal particles of various types, amounts, and sizes, resulting in a possibility to control product selectivity and efficiency. Finally, the challenge is developing stable and easy-fabricated electrodes, which can be used for actual CO_2 reduction applications with high production efficiency. Based on the current research progress and the blank space in this research field, it is recommended that further research be carried out from the following five aspects:

- The metalloid dopants (N, B, P, S) were reported to adjust the density of surface vacancies of Cu catalyst and form stable surface defects, which notably affects the CO binding and C_{2+} production. Thus, further researches are encouraged to focus on developing metalloid-doped Cu catalyst and exploring their application potential.

- Considering the synergistic effect of the metal modified Cu catalyst, the synthesis of two-dimensional conductive Cu-MOF is also meaningful to be developed due to that the electron conduction channel of two-dimensional framework materials play important role in the electrochemical reaction process.

- Surface modification is one important strategy to tune the selectivity. For example, Cu nanowire electrodes modified by amino acids and their derivatives stabilized

the and facilitated C^{2+} hydrocarbon formation, owning to the strong interaction between the $–NH_2$ groups and intermediate CHO*.

- For Cu-based catalyst in CO_2RR, the Cu electrode/electrolyte interface is a very complex reaction involving multiple proton and electron transfers. The electrocatalyst generally undergoes structure reconstruction under the applied potential. Applying advanced operando techniques (optical, X-ray and electron-based techniques) and theoretical calculation methods are highly demanded to characterize the morphology, crystal facet and electronic states of the electrochemical synthesized Cu catalyst under real operating CO_2RR process, which would shed light on understanding the reaction mechanism and provide further guidance for the catalyst development.
- Because of its low synthesis cost and easy scalability, in-situ electrochemical reduction allows the large-scale production of Cu coated electrode, which is particularly attractive for the production of catalyst electrodes for use in electrochemical reduction of CO_2. Therefore, Large scale experiment related to the scalable Cu-based catalyst needs be performed by choosing appropriate electrochemical conditions and accurately adjusting the parameters of the electrochemical method, for the industrialization of CO_2 electrocatalytic reduction.

REFERENCES

[1] Sekoai P T, Yoro K O. Biofuel development initiatives in sub-Saharan Africa: opportunities and challenges[J]. Climate, 2016, 4(2): 33.

[2] Kang Y, Khan S, Ma X. Climate change impacts on crop yield, crop water productivity and food security–A review[J]. Progress in natural Science, 2009, 19(12): 1665-1674.

[3] VijayaVenkataRaman S, Iniyan S, Goic R. A review of climate change, mitigation and adaptation[J]. Renewable and Sustainable Energy Reviews, 2012, 16(1): 878-897.

[4] Azevedo V G, Sartori S, Campos L M S. CO_2 emissions: A quantitative analysis among the BRICS nations[J]. Renewable and Sustainable Energy Reviews, 2018, 81: 107-115.

[5] Freund P. Anthropogenic climate change and the role of CO_2 capture and storage (CCS)[M]//Geological Storage of Carbon Dioxide (CO2). Woodhead Publishing, 2013: 3-25.

[6] Yoro K O, Sekoai P T. The potential of CO_2 capture and storage technology in South Africa's coal-fired thermal power plants[J]. Environments, 2016, 3(3): 24.

[7] Yoro K O, Isafiade A, Daramola M O. Synthesis of Mass Exchanger Networks Using Sequential Techniques[C]//The World Congress on Engineering and Computer Science. Springer, Singapore, 2018: 173-185.

[8] Amaral S S, Costa M A M, Neto T G S, et al. CO_2, CO, hydrocarbon gases and PM2. 5 emissions on dry season by deforestation fires in the Brazilian Amazonia[J]. Environmental Pollution, 2019, 249: 311-320.

[9] Ozonoh M, Aniokete T C, Oboirien B O, et al. Prediction of Emissions and Profits from a Biomass, Tyre, and Coal Fired Co-Gasification CHP Plant Using Artificial Neural Network: Nigerian and South African Perspectives[C]//Journal of Physics: Conference Series. IOP Publishing, 2019, 1378(2): 022021.

[10] Damiani D, Litynski J T, McIlvried H G, et al. The US department of Energy's R&D program to reduce greenhouse gas emissions through beneficial uses of carbon dioxide[J]. Greenhouse Gases: Science and Technology, 2012, 2(1): 9-16.

[11] Whipple D T, Kenis P J A. Prospects of CO_2 utilization via direct heterogeneous electrochemical reduction[J]. The Journal of Physical Chemistry Letters, 2010, 1(24): 3451-3458.

[12] Galadima A, Muraza O. Catalytic thermal conversion of CO_2 into fuels: Perspective and challenges[J]. Renewable and Sustainable Energy Reviews, 2019, 115: 109333.

[13] Chen C S, Cheng W H, Lin S S. Study of iron-promoted Cu/SiO_2 catalyst on high temperature reverse water gas shift reaction[J]. Applied Catalysis A: General, 2004, 257(1): 97-106.

[14] Roy S, Cherevotan A, Peter S C. Thermochemical CO_2 hydrogenation to single carbon products: scientific and technological challenges[J]. ACS Energy Letters, 2018, 3(8): 1938-1966.

[15] Kho E T, Tan T H, Lovell E, et al. A review on photo-thermal catalytic conversion of carbon dioxide[J]. Green Energy & Environment, 2017, 2(3): 204-217.

[16] Agarwal A S, Rode E, Sridhar N, et al. Conversion of CO_2 to value-added chemicals: Opportunities and challenges[J]. Handbook of Climate Change Mitigation and Adaptation; Springer International Publishing: Cham, Switzerland, 2017: 2487-2526.

[17] Quadrelli E A, Centi G, Duplan J L, et al. Carbon dioxide recycling: emerging large-scale technologies with industrial potential[J]. ChemSusChem, 2011, 4(9): 1194-1215.

[18] Kho E T, Tan T H, Lovell E, et al. A review on photo-thermal catalytic conversion of carbon dioxide[J]. Green Energy & Environment, 2017, 2(3): 204-217.

[19] Appel A M, Bercaw J E, Bocarsly A B, et al. Frontiers, opportunities, and challenges in biochemical and chemical catalysis of CO_2 fixation[J]. Chemical reviews, 2013, 113(8): 6621-6658.

[20] Cadham W, Van Dyk J S, Kumar J S L, et al. Challenges and opportunities for the conversion technologies used to make forest bioenergy[M]//Mobilisation of Forest Bioenergy in the Boreal and Temperate Biomes. Academic Press, 2016: 102-126.

[21] Aresta M, Dibenedetto A. Utilisation of CO_2 as a chemical feedstock: opportunities and challenges[J]. Dalton transactions, 2007 (28): 2975-2992.

[22] He M, Sun Y, Han B. Green carbon science: scientific basis for integrating carbon resource processing, utilization, and recycling[J]. Angewandte Chemie International Edition, 2013, 52(37): 9620-9633.

[23] Hunt A J, Sin E H K, Marriott R, et al. Generation, capture, and utilization of industrial carbon dioxide[J]. ChemSusChem: Chemistry & Sustainability Energy & Materials, 2010, 3(3): 306-322.

[24] Miller R, Wu G, Deshpande R R, et al. Changes in transcript abundance in Chlamydomonas reinhardtii following nitrogen deprivation predict diversion of metabolism[J]. Plant physiology, 2010, 154(4): 1737-1752.

[25] Morgan-Kiss R M, Priscu J C, Pocock T, et al. Adaptation and acclimation of photosynthetic microorganisms to permanently cold environments[J]. Microbiology and molecular biology reviews, 2006, 70(1): 222-252.

[26] Dexter J, Fu P. Metabolic engineering of cyanobacteria for ethanol production[J]. Energy & Environmental Science, 2009, 2(8): 857-864.

[27] Atsumi S, Higashide W, Liao J C. Direct photosynthetic recycling of carbon dioxide to isobutyraldehyde[J]. Nature biotechnology, 2009, 27(12): 1177-1180.

[28] Lindberg P, Park S, Melis A. Engineering a platform for photosynthetic isoprene production in cyanobacteria, using Synechocystis as the model organism[J]. Metabolic engineering, 2010, 12(1): 70-79.

[29] Ungerer J, Tao L, Davis M, et al. Sustained photosynthetic conversion of CO_2 to ethylene in recombinant cyanobacterium Synechocystis 6803[J]. Energy & Environmental Science, 2012, 5(10): 8998-9006.

[30] Berla B M, Saha R, Immethun C M, et al. Synthetic biology of cyanobacteria: unique challenges and opportunities[J]. Frontiers in microbiology, 2013, 4: 246.

[31] Markley A L, Begemann M B, Clarke R E, et al. Synthetic biology toolbox for controlling gene expression in the cyanobacterium Synechococcus sp. strain PCC 7002[J]. ACS synthetic biology, 2015, 4(5): 595-603.

[32] Nozzi N E, Case A E, Carroll A L, et al. Systematic approaches to efficiently produce 2, 3-butanediol in a marine cyanobacterium[J]. ACS synthetic biology, 2017, 6(11): 2136-2144.

[33] Phillips J R, Huhnke R L, Atiyeh H K. Syngas fermentation: a microbial conversion process of gaseous substrates to various products[J]. Fermentation, 2017, 3(2): 28.

[34] Cheng S, Xing D, Call D F, et al. Direct biological conversion of electrical current into methane by electromethanogenesis[J]. Environmental science & technology, 2009, 43(10): 3953-3958.

[35] Gross R, Buehler K, Schmid A. Engineered catalytic biofilms for continuous large scale production of n-octanol and (S)-styrene oxide[J]. Biotechnology and bioengineering, 2013, 110(2): 424-436.

[36] Darensbourg D J. Chemistry of carbon dioxide relevant to its utilization: a personal perspective[J]. Inorganic chemistry, 2010, 49(23): 10765-10780.

[37] Biermann M, Gruß H, Hummel W, et al. Guerbet alcohols: from processes under harsh conditions to synthesis at room temperature under ambient pressure[J]. ChemCatChem, 2016, 8(5): 895-899.

[38] Yong J K J, Stevens G W, Caruso F, et al. The use of carbonic anhydrase to accelerate carbon dioxide capture processes[J]. Journal of Chemical Technology & Biotechnology, 2015, 90(1): 3-10.

[39] Long N V D, Lee J, Koo K K, et al. Recent progress and novel applications in enzymatic conversion of carbon dioxide[J]. Energies, 2017, 10(4): 473.

[40] Parkin A, Seravalli J, Vincent K A, et al. Rapid and efficient electrocatalytic CO_2/CO interconversions by Carboxydothermus hydrogenoformans CO dehydrogenase I on an electrode[J]. Journal of the American Chemical Society, 2007, 129(34): 10328-10329.

[41] Spinner N, Mustain W E. Electrochemical Conversion of CO_2 and CH_4 to CH_3OH at Room Temperature through a Carbonate Anion Pathway[C]//ECS Meeting Abstracts. IOP Publishing, 2011 (18): 1501.

[42] Reda T, Plugge C M, Abram N J, et al. Reversible interconversion of carbon dioxide and formate by an electroactive enzyme[J]. Proceedings of the National Academy of Sciences, 2008, 105(31): 10654-10658.

[43] Shi Q, Chen J, Shen L. Driving factors of the changes in the carbon emissions in the Chinese construction industry[J]. Journal of Cleaner Production, 2017, 166: 615-627.

[44] Reda T, Plugge C M, Abram N J, et al. Reversible interconversion of carbon dioxide and formate by an electroactive enzyme[J]. Proceedings of the National Academy of Sciences, 2008, 105(31): 10654-10658.

[45] Shi Q, Chen J, Shen L. Driving factors of the changes in the carbon emissions in the Chinese construction industry[J]. Journal of Cleaner Production, 2017, 166: 615-627.

[46] Schlager S, Dumitru L M, Haberbauer M, et al. Electrochemical reduction of carbon dioxide to methanol by direct injection of electrons into immobilized enzymes on a modified electrode[J]. ChemSusChem, 2016, 9(6): 631.

[47] Aresta M, Dibenedetto A. Utilisation of CO_2 as a chemical feedstock: opportunities and challenges[J]. Dalton transactions, 2007 (28): 2975-2992.

[48] Yang S, Peng S, Xu J, et al. Methane and nitrous oxide emissions from paddy field as affected by water-saving irrigation[J]. Physics and Chemistry of the Earth, Parts A/B/C, 2012, 53: 30-37.

[49] Hong S G, Jeon H, Kim H S, et al. One-pot enzymatic conversion of carbon dioxide and utilization for improved microbial growth[J]. Environmental science & technology, 2015, 49(7): 4466-4472.

[50] Shi J, Jiang Y, Jiang Z, et al. Enzymatic conversion of carbon dioxide[J]. Chemical Society Reviews, 2015, 44(17): 5981-6000.

[51] Atsumi S, Higashide W, Liao J C. Direct photosynthetic recycling of carbon dioxide to isobutyraldehyde[J]. Nature biotechnology, 2009, 27(12): 1177-1180.

[52] Cazelles R, Drone J, Fajula F, et al. Reduction of CO_2 to methanol by a polyenzymatic system encapsulated in phospholipids–silica nanocapsules[J]. New Journal of Chemistry, 2013, 37(11): 3721-3730.

[53] Yaashikaa P R, Kumar P S, Varjani S J, et al. A review on photochemical, biochemical and electrochemical transformation of CO2 into value-added products[J]. Journal of CO_2 Utilization, 2019, 33: 131-147.

[54] Tahir M, Amin N A S. Photo-induced CO_2 reduction by hydrogen for selective CO evolution in a dynamic monolith photoreactor loaded with Ag-modified TiO_2 nanocatalyst[J]. International Journal of Hydrogen Energy, 2017, 42(23): 15507-15522.

[55] Xiang Q, Cheng B, Yu J. Graphene-based photocatalysts for solar-fuel generation[J]. Angewandte Chemie International Edition, 2015, 54(39): 11350-11366.

[56] Xi G, Ouyang S, Li P, et al. Ultrathin $W_{18}O_{49}$ nanowires with diameters below 1 nm: synthesis, near-infrared absorption, photoluminescence, and photochemical reduction of carbon dioxide[J]. Angewandte Chemie International Edition, 2012, 51(10): 2395-2399.

[57] Li X, Pan H, Li W, et al. Photocatalytic reduction of CO_2 to methane over HNb_3O_8 nanobelts[J]. Applied Catalysis A: General, 2012, 413: 103-108.

[58] Zhou Y, Tian Z, Zhao Z, et al. High-yield synthesis of ultrathin and uniform Bi_2WO_6 square nanoplates benefitting from photocatalytic reduction of CO_2 into renewable hydrocarbon fuel under visible light[J]. ACS applied materials & interfaces, 2011, 3(9): 3594-3601.

[59] Kočí K, Obalová L, Matějová L, et al. Effect of TiO_2 particle size on the photocatalytic reduction of CO_2[J]. Applied Catalysis B: Environmental, 2009, 89(3-4): 494-502.

[60] Liu Q, Zhou Y, Kou J, et al. High-yield synthesis of ultralong and ultrathin Zn_2GeO_4 nanoribbons toward improved photocatalytic reduction of CO_2 into renewable hydrocarbon fuel[J]. Journal of the American Chemical Society, 2010, 132(41): 14385-14387.

[61] Lekse J W, Underwood M K, Lewis J P, et al. Synthesis, Characterization, Electronic Structure, and Photocatalytic Behavior of CuGaO2 and $CuGa1–xFe_xO_2$ (x= 0.05, 0.10, 0.15, 0.20) Delafossites[J]. The Journal of Physical Chemistry C, 2012, 116(2): 1865-1872.

[62] Barton E E, Rampulla D M, Bocarsly A B. Selective solar-driven reduction of CO_2 to methanol using a catalyzed p-GaP based photoelectrochemical cell[J]. Journal of the American Chemical Society, 2008, 130(20): 6342-6344.

[63] Wang C, Xie Z, deKrafft K E, et al. Doping metal–organic frameworks for water oxidation, carbon dioxide reduction, and organic photocatalysis[J]. Journal of the American Chemical Society, 2011, 133(34): 13445-13454.

[64] Jensen J, Mikkelsen M, Krebs F C. Flexible substrates as basis for photocatalytic reduction of carbon dioxide[J]. Solar energy materials and solar cells, 2011, 95(11): 2949-2958.

[65] Qiao J, Liu Y, Hong F, et al. A review of catalysts for the electroreduction of carbon dioxide to produce low-carbon fuels[J]. Chemical Society Reviews, 2014, 43(2): 631-675.

[66] Seh Z W, Kibsgaard J, Dickens C F, et al. Combining theory and experiment in electrocatalysis: Insights into materials design[J]. Science, 2017, 355(6321).

[67] Zhao C X, Bu Y F, Gao W, et al. CO_2 reduction mechanism on the Pb (111) surface: effect of solvent and cations[J]. The Journal of Physical Chemistry C, 2017, 121(36): 19767-19773.

[68] Ye F, Gao J, Chen Y, et al. Oxidized indium with transformable dimensions for CO_2 electroreduction toward formate aided by oxygen vacancies[J]. Sustainable Energy & Fuels, 2020, 4(7): 3726-3731.

[69] Zheng X, De Luna P, de Arquer F P G, et al. Sulfur-modulated tin sites enable highly selective electrochemical reduction of CO_2 to formate[J]. Joule, 2017, 1(4): 794-805.

[70] Zhang S, Kang P, Meyer T J. Nanostructured tin catalysts for selective electrochemical reduction of carbon dioxide to formate[J]. Journal of the American Chemical Society, 2014, 136(5): 1734-1737.

[71] Deng P, Wang H, Qi R, et al. Bismuth oxides with enhanced bismuth–oxygen structure for efficient electrochemical reduction of carbon dioxide to formate[J]. ACS Catalysis, 2019, 10(1): 743-750.

[72] Atifi A, Keane T P, DiMeglio J L, et al. Insights into the Composition and Function of a Bismuth-Based Catalyst for Reduction of CO_2 to CO[J]. The Journal of Physical Chemistry C, 2019, 123(14): 9087-9095.

[73] Liu M, Pang Y, Zhang B, et al. Enhanced electrocatalytic CO_2 reduction via field-induced reagent concentration[J]. Nature, 2016, 537(7620): 382-386.

[74] Ham Y S, Choe S, Kim M J, et al. Electrodeposited Ag catalysts for the electrochemical reduction of CO_2 to CO[J]. Applied Catalysis B: Environmental, 2017, 208: 35-43.

[75] Lei F, Liu W, Sun Y, et al. Metallic tin quantum sheets confined in graphene toward high-efficiency carbon dioxide electroreduction[J]. Nature communications, 2016, 7(1): 1-8.

[76] Klinkova A, De Luna P, Dinh C T, et al. Rational design of efficient palladium catalysts for electroreduction of carbon dioxide to formate[J]. Acs Catalysis, 2016, 6(12): 8115-8120.

[77] Xia R, Zhang S, Ma X, et al. Surface-functionalized palladium catalysts for electrochemical CO_2 reduction[J]. Journal of Materials Chemistry A, 2020, 8(31): 15884-15890.

[78] Yan C, Lin L, Gao D, et al. Selective CO_2 electroreduction over an oxide-derived gallium catalyst[J]. Journal of Materials Chemistry A, 2018, 6(40): 19743-19749.

[79] Zhang L, Zhao Z J, Gong J. Nanostructured materials for heterogeneous electrocatalytic CO_2 reduction and their related reaction mechanisms[J]. Angewandte Chemie International Edition, 2017, 56(38): 11326-11353.

[80] Klinkova A, De Luna P, Dinh C T, et al. Rational design of efficient palladium catalysts for electroreduction of carbon dioxide to formate[J]. Acs Catalysis, 2016, 6(12): 8115-8120.

[81] Xie H, Wang T, Liang J, et al. Cu-based nanocatalysts for electrochemical reduction of CO_2[J]. Nano Today, 2018, 21: 41-54.

[82] Zhang B, Zhang J. Rational design of Cu-based electrocatalysts for electrochemical reduction of carbon dioxide[J]. Journal of energy chemistry, 2017, 26(6): 1050-1066.

[83] Handoko A D, Steinmann S N, Seh Z W. Theory-guided materials design: two-dimensional MXenes in electro-and photocatalysis[J]. Nanoscale Horizons, 2019, 4(4): 809-827.

[84] Lim K R G, Handoko A D, Nemani S K, et al. Rational design of two-dimensional transition metal carbide/nitride (MXene) hybrids and nanocomposites for catalytic energy storage and conversion[J]. ACS nano, 2020, 14(9): 10834-10864.

[85] He D, Wang B, Wu T, et al. TiO_2 Nanocrystal-Framed Li_2TiSiO_5 Platelets for Low-Voltage Lithium Battery Anode[J]. Advanced Functional Materials, 2020, 30(45): 2001909.

[86] Zhang S, Fan Q, Xia R, et al. CO_2 reduction: from homogeneous to heterogeneous electrocatalysis[J]. Accounts of chemical research, 2020, 53(1): 255-264.

[87] Regulacio M D, Wang Y, Seh Z W, et al. Tailoring porosity in copper-based multinary sulfide nanostructures for energy, biomedical, catalytic, and sensing applications[J]. ACS Applied Nano Materials, 2018, 1(7): 3042-3062.

[88] Le Van T, Che M, Kermarec M, et al. Structure sensitivity of the catalytic oxidative coupling of methane on lanthanum oxide[J]. Catalysis letters, 1990, 6(3): 395-400.

[89] Wang F, Ta N, Li Y, et al. La $(OH)_3$ and $La_2O_2CO_3$ nanorod catalysts for Claisen-Schmidt condensation[J]. Chinese Journal of Catalysis, 2014, 35(3): 437-443.

[90] Park C, Nguyen-Phu H, Shin E W. Glycerol carbonation with CO_2 and $La_2O_2CO_3$/ZnO catalysts prepared by two different methods: Preferred reaction route depending on crystalline structure[J]. Molecular Catalysis, 2017, 435: 99-109.

[91] Lacombe S, Geantet C, Mirodatos C. Oxidative coupling of methane over lanthana catalysts: I. Identification and role of specific active-sites[J]. Journal of Catalysis, 1995, 151(2): 439-452.

[92] Chen H, Yu H, Peng F, et al. Efficient and stable oxidative steam reforming of ethanol for hydrogen production: effect of in situ dispersion of Ir over Ir/La_2O_3[J]. Journal of Catalysis, 2010, 269(2): 281-290.

[93] Wang H, Fang Y, Liu Y, et al. Perovskite $LaFeO_3$ supported bi-metal catalyst for syngas methanation[J]. Journal of natural gas chemistry, 2012, 21(6): 745-752.

[94] Turcotte R P, Sawyer J O, Eyring L R. Rare earth dioxymonocarbonates and their decomposition[J]. inorganic Chemistry, 1969, 8(2): 238-246.

[95] Olafsen A, Fjellvåg H. Synthesis of rare earth oxide carbonates and thermal stability of $Nd_2O_2CO_3$ II[J]. Journal of Materials Chemistry, 1999, 9(10): 2697-2702.

[96] Hirsch O, Kvashnina K O, Luo L, et al. High-energy resolution X-ray absorption and emission spectroscopy reveals insight into unique selectivity of La-based nanoparticles for CO_2[J]. Proceedings of the National Academy of Sciences, 2015, 112(52): 15803-15808.

[97] Hölsä J, Turkki T. Preparation, thermal stability and luminescence properties of selected rare earth oxycarbonates[J]. Thermochimica acta, 1991, 190(2): 335-343.

[98] Koyabu K, Masui T, Tamura S, et al. Synthesis of a new phosphor based on rare earth oxycarbonate[J]. Journal of alloys and compounds, 2006, 408: 867-870.

[99] Yu H, Men Y, Shin E W. Structural properties of disordered macroporous $La_2O_2CO_3$/ZnO materials prepared by a solution combusion method[J]. Korean Journal of Chemical Engineering, 2019, 36(4): 522-528.

[100] Yoshio H, Katsuhei K, Shin S. Production of CO and CH_4 in electrochemical reduction of CO_2 at metal electrodes in aqueous hydrogencarbonate solution[J]. Chem. Lett, 1985, 14: 1695-1698.

[101] Hori Y, Wakebe H, Tsukamoto T, et al. Electrocatalytic process of CO selectivity in electrochemical reduction of CO_2 at metal electrodes in aqueous media[J]. Electrochimica Acta, 1994, 39(11-12): 1833-1839.

[102] Hori Y. Electrochemical CO_2 reduction on metal electrodes[M]//Modern aspects of electrochemistry. Springer, New York, NY, 2008: 89-189.

[103] McCreery R L. Advanced carbon electrode materials for molecular electrochemistry[J]. Chemical reviews, 2008, 108(7): 2646-2687.

[104] Yang N, Waldvogel S R, Jiang X. Electrochemistry of carbon dioxide on carbon electrodes[J]. ACS applied materials & interfaces, 2016, 8(42): 28357-28371.

[105]Yang N, Swain G M, Jiang X. Nanocarbon electrochemistry and electroanalysis: current status and future perspectives[J]. Electroanalysis, 2016, 28(1): 27-34.

[106] Ivandini T A, Einaga Y. Polycrystalline boron-doped diamond electrodes for electrocatalytic and electrosynthetic applications[J]. Chemical Communications, 2017, 53(8): 1338-1347.

[107] Ramli Z A C, Kamarudin S K. Platinum-based catalysts on various carbon supports and conducting polymers for direct methanol fuel cell applications: a review[J]. Nanoscale research letters, 2018, 13(1): 1-25.

[108] Ding D, Lu W, Xiong Y, et al. Facile synthesis of $La_2O_2CO_3$ nanoparticle films and its CO_2 sensing properties and mechanisms[J]. Applied Surface Science, 2017, 426: 725-733.

[109] Wang F, Zhang Z, Wei X, et al. The shape effect of $La_2O_2CO_3$ in Pd/$La_2O_2CO_3$ catalyst for selective hydrogenation of cinnamaldehyde[J]. Applied Catalysis A: General, 2017, 543: 196-200.

[110] Li X, Li D, Tian H, et al. Dry reforming of methane over Ni/La_2O_3 nanorod catalysts with stabilized Ni nanoparticles[J]. Applied Catalysis B: Environmental, 2017, 202: 683-694.

[111] Bosch C E, Copley M P, Eralp T, et al. Tailoring the physical and catalytic properties of lanthanum oxycarbonate nanoparticles[J]. Applied Catalysis A: General, 2017, 536: 104-112.

[112] Mu Q, Wang Y. Synthesis, characterization, shape-preserved transformation, and optical properties of La $(OH)_3$, $La_2O_2CO_3$, and La_2O_3 nanorods[J]. Journal of alloys and compounds, 2011, 509(2): 396-401.

[113] Sun C, Sun J, Xiao G, et al. Mesoscale organization of nearly monodisperse flowerlike ceria microspheres[J]. The Journal of Physical Chemistry B, 2006, 110(27): 13445-13452.

[114] Yi G, Lu H, Zhao S, et al. Synthesis, characterization, and biological application of size-controlled nanocrystalline $NaYF_4$: Yb, Er infrared-to-visible up-conversion phosphors[J]. Nano letters, 2004, 4(11): 2191-2196.

[115] Li G, Peng C, Zhang C, et al. Eu^{3+}/Tb^{3+}-doped $La_2O_2CO_3$/La_2O_3 nano/microcrystals with multiform morphologies: facile synthesis, growth mechanism, and luminescence properties[J]. Inorganic chemistry, 2010, 49(22): 10522-10535.

[116] Lin J, Yu M, Lin C, et al. Multiform oxide optical materials via the versatile Pechini-type sol− gel process: Synthesis and characteristics[J]. The Journal of Physical Chemistry C, 2007, 111(16): 5835-5845.

[117] Koyabu K, Masui T, Tamura S, et al. Synthesis of a new phosphor based on rare earth oxycarbonate[J]. Journal of alloys and compounds, 2006, 408: 867-870.

[118] Kresse G, Furthmüller J. Efficient iterative schemes for ab initio total-energy calculations using a plane-wave basis set[J]. Physical review B, 1996, 54(16): 11169.

[119] Kresse G, Furthmüller J. Efficiency of ab-initio total energy calculations for metals and semiconductors using a plane-wave basis set[J]. Computational materials science, 1996, 6(1): 15-50.

[120] Perdew J P, Burke K, Ernzerhof M. Generalized gradient approximation made simple[J]. Physical review letters, 1996, 77(18): 3865.

[121] Monkhorst H J, Pack J D. Special points for Brillouin-zone integrations[J]. Physical review B, 1976, 13(12): 5188.

[122] Hou Y H, Han W C, Xia W S, et al. Structure sensitivity of $La_2O_2CO_3$ catalysts in the oxidative coupling of methane[J]. ACS Catalysis, 2015, 5(3): 1663-1674.

[123] Fleming P, Farrell R A, Holmes J D, et al. The rapid formation of La $(OH)_3$ from La_2O_3 powders on exposureto water vapor[J]. Journal of the American Ceramic Society, 2010, 93(4): 1187-1194.

[124] Fedorov P P, Nazarkin M V, Zakalyukin R M. On polymorphism and morphotropism of rare earth sesquioxides[J]. Crystallography Reports, 2002, 47(2): 281-286.

[125] Bakiz B, Guinneton F, Arab M, et al. Elaboration, characterization of $LaOHCO_3$, $La_2O_2CO_3$ and La_2O_3 phases and their gas solid interactions with CH4 and CO gases[J]. Moroccan Journal of Condensed Matter, 2010, 12(1).

[126] Sholl D, Steckel J A. Density functional theory: a practical introduction[M]. John Wiley & Sons, 2011.

[127] Olafsen A, Larsson A K, Fjellvåg H, et al. On the crystal structure of $Ln_2O_2CO_3$ II (Ln= La and Nd)[J]. Journal of Solid State Chemistry, 2001, 158(1): 14-24.

[128] Attfield J P, Ferey G. Structure determinations of $La_2O_2CO_3$-II and the unusual disordered phase La_2O_2. 52 (CO_3) 0.74 Li_0. 52 using powder diffraction[J]. Journal of Solid State Chemistry, 1989, 82(1): 132-138.

[129] Di Cosimo J I, Dıez V K, Xu M, et al. Structure and surface and catalytic properties of Mg-Al basic oxides[J]. Journal of Catalysis, 1998, 178(2): 499-510.

[130] Zhang J, Yin R, Shao Q, et al. Oxygen vacancies in amorphous InOx nanoribbons enhance CO_2 adsorption and activation for CO_2 electroreduction[J]. Angewandte Chemie International Edition, 2019, 58(17): 5609-5613.

[131] Zhang B, Zhang J, Hua M, et al. Highly electrocatalytic ethylene production from CO_2 on nanodefective Cu nanosheets[J]. Journal of the American Chemical Society, 2020, 142(31): 13606-13613.

[132] Rémiás R, Kukovecz Á, Darányi M, et al. Synthesis of zinc glycerolate microstacks from a ZnO nanorod sacrificial template[J]. European Journal of Inorganic Chemistry, 2009, 2009(24): 3622-3627.

[133] Manoilova O V, Podkolzin S G, Tope B, et al. Surface acidity and basicity of La_2O_3, LaOCl, and $LaCl_3$ characterized by IR spectroscopy, TPD, and DFT calculations[J]. The Journal of Physical Chemistry B, 2004, 108(40): 15770-15781.

[134] Horiuchi T, Hidaka H, Fukui T, et al. Effect of added basic metal oxides on CO_2 adsorption on alumina at elevated temperatures[J]. Applied Catalysis A: General, 1998, 167(2): 195-202.

[135] Meadowcroft D B. Some properties of strontium-doped lanthanum chromite[J]. Journal of Physics D: Applied Physics, 1969, 2(9): 1225.

[136] Song Q W, Wang X M, Bussjager R, et al. Electro-optic beam-steering device based on a lanthanum-modified lead zirconate titanate ceramic wafer[J]. Applied optics, 1996, 35(17): 3155-3162.

[137] Tarjomannejad A, Farzi A, Niaei A, et al. An experimental and kinetic study of toluene oxidation over LaMn 1− xB_xO_3 and La 0.8 A 0.2 Mn 0.3 B 0.7 O 3 (A= Sr, Ce and B= Cu, Fe) nano-perovskite catalysts[J]. Korean Journal of Chemical Engineering, 2016, 33(9): 2628-2637.

[138] Park S H, Chun B H, Kim S H. Effects of La_2O_3 on ZrO_2 supported Ni catalysts for autothermal reforming of CH_4[J]. Korean Journal of Chemical Engineering, 2011, 28(2): 402-408.

[139] Kašpar J, Fornasiero P, Hickey N. Automotive catalytic converters: current status and some perspectives[J]. Catalysis today, 2003, 77(4): 419-449.

[140] Ma J, Fang M, Lau N T. The catalytic reduction of SO_2 by CO over lanthanum oxysulphide[J]. Applied Catalysis A: General, 1997, 150(2): 253-268.

[141] Herrera G, Jiménez-Mier J, Chavira E. Layered-structural monoclinic–orthorhombic perovskite La2Ti2O7 to orthorhombic $LaTiO_3$ phase transition and their microstructure characterization[J]. Materials characterization, 2014, 89: 13-22.

[142] Ding D, Lu W, Xiong Y, et al. Facile synthesis of $La_2O_2CO_3$ nanoparticle films and its CO_2 sensing properties and mechanisms[J]. Applied Surface Science, 2017, 426: 725-733.

[143] Jia L, Li J, Fang W. Effect of H_2/CO_2 mixture gas treatment temperature on the activity of $LaNiO_3$ catalyst for hydrogen production from formaldehyde aqueous solution under visible light[J]. Journal of alloys and compounds, 2010, 489(2): L13-L16.

[144] Wang F, Zhang Z, Wei X, et al. The shape effect of $La_2O_2CO_3$ in Pd/$La_2O_2CO_3$ catalyst for selective hydrogenation of cinnamaldehyde[J]. Applied Catalysis A: General, 2017, 543: 196-200.

[145] Li X, Li D, Tian H, et al. Dry reforming of methane over Ni/La_2O_3 nanorod catalysts with stabilized Ni nanoparticles[J]. Applied Catalysis B: Environmental, 2017, 202: 683-694.

[146] Park C, Nguyen-Phu H, Shin E W. Glycerol carbonation with CO_2 and $La_2O_2CO_3$/ZnO catalysts prepared by two different methods: Preferred reaction route depending on crystalline structure[J]. Molecular Catalysis, 2017, 435: 99-109.

[147] Park C, Nguyen-Phu H, Shin E W. Glycerol carbonation with CO_2 and $La_2O_2CO_3$/ZnO catalysts prepared by two different methods: Preferred reaction route depending on crystalline structure[J]. Molecular Catalysis, 2017, 435: 99-109.

[148] Li H, Jiao X, Li L, et al. Synthesis of glycerol carbonate by direct carbonylation of glycerol with CO_2 over solid catalysts derived from Zn/Al/La and Zn/Al/La/M (M= Li, Mg and Zr) hydrotalcites[J]. Catalysis Science & Technology, 2015, 5(2): 989-1005.

[149] Zhang Y, Jin L, Sterling K, et al. Potassium modified layered $Ln_2O_2CO_3$ (Ln: La, Nd, Sm, Eu) materials: efficient and stable heterogeneous catalysts for biofuel production[J]. Green Chemistry, 2015, 17(6): 3600-3608.

[150] Bosch C E, Copley M P, Eralp T, et al. Tailoring the physical and catalytic properties of lanthanum oxycarbonate nanoparticles[J]. Applied Catalysis A: General, 2017, 536: 104-112.

[151] Niu H, Min Q, Tao Z, et al. One-pot facile synthesis and optical properties of porous La2O2CO3 hollow microspheres[J]. Journal of alloys and compounds, 2011, 509(3): 744-747.

[152] Mu Q, Wang Y. Synthesis, characterization, shape-preserved transformation, and optical properties of La $(OH)_3$, $La_2O_2CO_3$, and La_2O_3 nanorods[J]. Journal of alloys and compounds, 2011, 509(2): 396-401.

[153] Tsoukalou A, Imtiaz Q, Kim S M, et al. Dry-reforming of methane over bimetallic Ni–M/La_2O_3 (M= Co, Fe): The effect of the rate of $La_2O_2CO_3$ formation and phase stability on the catalytic activity and stability[J]. Journal of Catalysis, 2016, 343: 208-214.

[154] Pakhare D, Schwartz V, Abdelsayed V, et al. Kinetic and mechanistic study of dry (CO_2) reforming of methane over Rh-substituted $La_2Zr_2O_7$ pyrochlores[J]. Journal of catalysis, 2014, 316: 78-92.

[155] Yu H, Men Y, Shin E W. Structural properties of disordered macroporous $La_2O_2CO_3$/ZnO materials prepared by a solution combusion method[J]. Korean Journal of Chemical Engineering, 2019, 36(4): 522-528.

[156] Zhang G, Zhen Z, Jian L, et al. Macroporous perovskite-type complex oxide catalysts of La1–xKxCo1–yFeyO$_3$ for diesel soot combustion[J]. Journal of Rare Earths, 2009, 27(6): 955-960.

[157] Irusta S, Cornaglia L M, Lombardo E A. Effects of rhodium and platinum on the reactivity of lanthanum phases[J]. Materials chemistry and physics, 2004, 86(2-3): 440-447.

[158] Turcotte R P, Sawyer J O, Eyring L R. Rare earth dioxymonocarbonates and their decomposition[J]. inorganic Chemistry, 1969, 8(2): 238-246.

[159] Levan T, Che M, Tatibouet J M, et al. Infrared study of the formation and stability of $La_2O_2CO_3$ during the oxidative coupling of methane on La_2O_3[J]. Journal of Catalysis, 1993, 142(1): 18-26.

[160] Ni J, Chen L, Lin J, et al. High performance of Mg–La mixed oxides supported Ni catalysts for dry reforming of methane: The effect of crystal structure[J]. International journal of hydrogen energy, 2013, 38(31): 13631-13642.

[161] Gao S, Lin Y, Jiao X, et al. Partially oxidized atomic cobalt layers for carbon dioxide electroreduction to liquid fuel[J]. Nature, 2016, 529(7584): 68-71.

[162] Jiang K, Sandberg R B, Akey A J, et al. Metal ion cycling of Cu foil for selective C–C coupling in electrochemical CO_2 reduction[J]. Nature Catalysis, 2018, 1(2): 111-119.

[163] Ren W, Tan X, Yang W, et al. Isolated diatomic Ni‐Fe metal–nitrogen sites for synergistic electroreduction of CO_2[J]. Angewandte Chemie International Edition, 2019, 58(21): 6972-6976.

[164] Yang H B, Hung S F, Liu S, et al. Atomically dispersed Ni (I) as the active site for electrochemical CO_2 reduction[J]. Nature energy, 2018, 3(2): 140-147.

[165] Sun X, Chen C, Liu S, et al. Aqueous CO_2 Reduction with High Efficiency Using α‐Co $(OH)_2$‐Supported Atomic Ir Electrocatalysts[J]. Angewandte Chemie, 2019, 131(14): 4717-4721.

[166] Zhu W, Zhang L, Yang P, et al. Low‐coordinated edge sites on ultrathin palladium nanosheets boost carbon dioxide electroreduction performance[J]. Angewandte Chemie, 2018, 130(36): 11718-11722.

[167] Jeon H S, Kunze S, Scholten F, et al. ACS Catal. 2018, 8, 531-535; g) A. Eilert, FS Roberts, D. Friebel, A. Nilsson[J]. J. Phys. Chem. Lett, 2016, 7: 1466-1470.

[168] Liu S, Tao H, Zeng L, et al. Shape-dependent electrocatalytic reduction of CO_2 to CO on triangular silver nanoplates[J]. Journal of the American chemical society, 2017, 139(6): 2160-2163.

[169] Dinh C T, Burdyny T, Kibria M G, et al. tokaldani, CM Gabardo, FPG de Arquer, A[J]. Kiani, JP Edwards, P. De Luna, OS Bushuyev, CQ Zou, R. Quintero-Bermudez, YJ Pang, D. Sinton and EH Sargent, Science, 2018, 360: 783-787.

[170] Lee S Y, Jung H, Kim N K, et al. Mixed copper states in anodized Cu electrocatalyst for stable and selective ethylene production from CO_2 reduction[J]. Journal of the American Chemical Society, 2018, 140(28): 8681-8689.

[171] Jiao J, Lin R, Liu S, et al. Copper atom-pair catalyst anchored on alloy nanowires for selective and efficient electrochemical reduction of CO_2[J]. Nature chemistry, 2019, 11(3): 222-228.

[172] De Luna P, Quintero-Bermudez R, Dinh C T, et al. Catalyst electro-redeposition controls morphology and oxidation state for selective carbon dioxide reduction[J]. Nature Catalysis, 2018, 1(2): 103-110.

[173] Wang X, de Araújo J F, Ju W, et al. Mechanistic reaction pathways of enhanced ethylene yields during electroreduction of CO_2–CO co-feeds on Cu and Cu-tandem electrocatalysts[J]. Nature nanotechnology, 2019, 14(11): 1063-1070.

[174] Liu J, Guo C, Hu X, et al. Bio-proton coupled semiconductor/metal-complex hybrid photoelectrocatalytic interface for efficient CO_2 reduction[J]. Green Chemistry, 2019, 21(2): 339-348.

[175] Huang X, Shen Q, Liu J, et al. A CO_2 adsorption-enhanced semiconductor/metal-complex hybrid photoelectrocatalytic interface for efficient formate production[J]. Energy & Environmental Science, 2016, 9(10): 3161-3171.

[176] Zhou Y, Che F, Liu M, et al. Dopant-induced electron localization drives CO_2 reduction to C_2 hydrocarbons[J]. Nature chemistry, 2018, 10(9): 974-980.

[177] Cui R, Shen Q, Guo C, et al. Syngas electrosynthesis using self-supplied CO_2 from photoelectrocatalytic pollutant degradation[J]. Applied Catalysis B: Environmental, 2020, 261: 118253.

[178] Zhu Q, Ma J, Kang X, et al. Efficient reduction of CO_2 into formic acid on a lead or tin electrode using an ionic liquid catholyte mixture[J]. Angewandte Chemie, 2016, 128(31): 9158-9162.

[179] Lv J J, Jouny M, Luc W, et al. A highly porous copper electrocatalyst for carbon dioxide reduction[J]. Advanced Materials, 2018, 30(49): 1803111.

[180] Nam D H, Bushuyev O S, Li J, et al. Metal–organic frameworks mediate Cu coordination for selective CO_2 electroreduction[J]. Journal of the American Chemical Society, 2018, 140(36): 11378-11386.

[181] Morales-Guio C G, Cave E R, Nitopi S A, et al. Improved CO_2 reduction activity towards C_{2+} alcohols on a tandem gold on copper electrocatalyst[J]. Nature Catalysis, 2018, 1(10): 764-771.

[182] Liang Z Q, Zhuang T T, Seifitokaldani A, et al. Copper-on-nitride enhances the stable electrosynthesis of multi-carbon products from CO_2[J]. Nature communications, 2018, 9(1): 1-8.

[183] Jung H, Lee S Y, Lee C W, et al. Electrochemical fragmentation of Cu_2O nanoparticles enhancing selective C–C coupling from CO_2 reduction reaction[J]. Journal of the American Chemical Society, 2019, 141(11): 4624-4633.

[184] Huang J, Mensi M, Oveisi E, et al. Structural sensitivities in bimetallic catalysts for electrochemical CO_2 reduction revealed by Ag–Cu nanodimers[J]. Journal of the American Chemical Society, 2019, 141(6): 2490-2499.

[185] Grosse P, Gao D, Scholten F, et al. Dynamic changes in the structure, chemical state and catalytic selectivity of Cu nanocubes during CO_2 electroreduction: size and support effects[J]. Angewandte Chemie International Edition, 2018, 57(21): 6192-6197.

[186] Chen C, Sun X, Lu L, et al. Efficient electroreduction of CO_2 to C_2 products over B-doped oxide-derived copper[J]. Green Chemistry, 2018, 20(20): 4579-4583.

[187] Duan Y X, Meng F L, Liu K H, et al. Amorphizing of Cu nanoparticles toward highly efficient and robust electrocatalyst for CO_2 reduction to liquid fuels with high faradaic efficiencies[J]. Advanced Materials, 2018, 30(14): 1706194.

[188] Handoko A D, Chan K W, Yeo B S. $–CH_3$ mediated pathway for the electroreduction of CO_2 to ethane and ethanol on thick oxide-derived copper catalysts at low overpotentials[J]. ACS Energy Letters, 2017, 2(9): 2103-2109.

[189] Li C W, Kanan M W. CO_2 reduction at low overpotential on Cu electrodes resulting from the reduction of thick Cu_2O films[J]. Journal of the American Chemical Society, 2012, 134(17): 7231-7234.

[190] Raciti D, Livi K J, Wang C. Highly dense Cu nanowires for low-overpotential CO_2 reduction[J]. Nano letters, 2015, 15(10): 6829-6835.

[191] Ren D, Deng Y L, Handoko A D, et al. Selective electrochemical reduction of carbon dioxide to ethylene and ethanol on copper (I) oxide catalysts. ACS Catal 5: 2814–2821[J]. 2015.

[192] Mistry H, Varela A S, Bonifacio C S, et al. Highly selective plasma-activated copper catalysts for carbon dioxide reduction to ethylene[J]. Nature communications, 2016, 7(1): 1-9.

[193] Zhu Q, Sun X, Yang D, et al. Carbon dioxide electroreduction to C_2 products over copper-cuprous oxide derived from electrosynthesized copper complex[J]. Nature communications, 2019, 10(1): 1-11.

[194] Kim J, Choi W, Park J W, et al. Branched copper oxide nanoparticles induce highly selective ethylene production by electrochemical carbon dioxide reduction[J]. Journal of the American Chemical Society, 2019, 141(17): 6986-6994.

[195] Verdaguer-Casadevall A, Li C W, Johansson T P, et al. Probing the active surface sites for CO reduction on oxide-derived copper electrocatalysts[J]. Journal of the American Chemical Society, 2015, 137(31): 9808-9811.

[196] Kondratenko E V, Mul G, Baltrusaitis J, et al. Status and perspectives of CO_2 conversion into fuels and chemicals by catalytic, photocatalytic and electrocatalytic processes[J]. Energy & environmental science, 2013, 6(11): 3112-3135.

[197] Qiao J, Liu Y, Hong F, et al. A review of catalysts for the electroreduction of carbon dioxide to produce low-carbon fuels[J]. Chemical Society Reviews, 2014, 43(2): 631-675.

[198] Hatsukade T, Kuhl K P, Cave E R, et al. Insights into the electrocatalytic reduction of CO_2 on metallic silver surfaces[J]. Physical Chemistry Chemical Physics, 2014, 16(27): 13814-13819.

[199] Yang N, Waldvogel S R, Jiang X. Electrochemistry of carbon dioxide on carbon electrodes[J]. ACS applied materials & interfaces, 2016, 8(42): 28357-28371.

[200] Chen W, Xin Q, Sun G, et al. The effect of carbon support treatment on the stability of Pt/C electrocatalysts[J]. Journal of power sources, 2008, 180(1): 199-204.

[201] Zhou Y, Che F, Liu M, et al. Dopant-induced electron localization drives CO_2 reduction to C_2 hydrocarbons[J]. Nature chemistry, 2018, 10(9): 974-980.

[202] Wu M, Zhu C, Wang K, et al. Promotion of CO_2 electrochemical reduction via Cu nanodendrites[J]. ACS applied materials & interfaces, 2020, 12(10): 11562-11569.

[203] Yang P P, Zhang X L, Gao F Y, et al. Protecting copper oxidation state via intermediate confinement for selective CO_2 electroreduction to C_2+ fuels[J]. Journal of the American Chemical Society, 2020, 142(13): 6400-6408.

[204] Loiudice A, Lobaccaro P, Kamali E A, et al. Tailoring copper nanocrystals towards C_2 products in electrochemical CO_2 reduction[J]. Angewandte Chemie International Edition, 2016, 55(19): 5789-5792.

[205] Chen Y, Fan Z, Wang J, et al. Ethylene selectivity in electrocatalytic CO_2 reduction on Cu nanomaterials: a crystal phase-dependent study[J]. Journal of the American Chemical Society, 2020, 142(29): 12760-12766.

[206] Liang Z Q, Zhuang T T, Seifitokaldani A, et al. Copper-on-nitride enhances the stable electrosynthesis of multi-carbon products from CO_2[J]. Nature communications, 2018, 9(1): 1-8.

[207] De Luna P, Quintero-Bermudez R, Dinh C T, et al. Catalyst electro-redeposition controls morphology and oxidation state for selective carbon dioxide reduction[J]. Nature Catalysis, 2018, 1(2): 103-110.

[208] Kibria M G, Dinh C T, Seifitokaldani A, et al. A surface reconstruction route to high productivity and selectivity in CO_2 electroreduction toward C_{2+} hydrocarbons[J]. Advanced Materials, 2018, 30(49): 1804867.

[209] Ma W, Xie S, Liu T, et al. Electrocatalytic reduction of CO_2 to ethylene and ethanol through hydrogen-assisted C–C coupling over fluorine-modified copper[J]. Nature Catalysis, 2020, 3(6): 478-487.

[210] Handoko A D, Ong C W, Huang Y, et al. Mechanistic insights into the selective electroreduction of carbon dioxide to ethylene on Cu_2O-derived copper catalysts[J]. The Journal of Physical Chemistry C, 2016, 120(36): 20058-20067.

[211] Altaf N, Liang S, Huang L, et al. Electro-derived Cu-Cu_2O nanocluster from LDH for stable and selective C_2 hydrocarbons production from CO_2 electrochemical reduction[J]. Journal of Energy Chemistry, 2020, 48: 169-180.

[212] Gu Z, Yang N, Han P, et al. Oxygen vacancy tuning toward efficient electrocatalytic CO_2 reduction to C_2H_4[J]. Small Methods, 2019, 3(2): 1800449.

[213] Lv J J, Jouny M, Luc W, et al. A highly porous copper electrocatalyst for carbon dioxide reduction[J]. Advanced Materials, 2018, 30(49): 1803111.

[214] Peng Y, Wu T, Sun L, et al. Selective electrochemical reduction of CO_2 to ethylene on nanopores-modified copper electrodes in aqueous solution[J]. ACS applied materials & interfaces, 2017, 9(38): 32782-32789.

[215] Gao D, Zegkinoglou I, Divins N J, et al. Plasma-activated copper nanocube catalysts for efficient carbon dioxide electroreduction to hydrocarbons and alcohols[J]. ACS nano, 2017, 11(5): 4825-4831.

[216] Yang K D, Ko W R, Lee J H, et al. Morphology‐directed selective production of ethylene or ethane from CO_2 on a Cu mesopore electrode[J]. Angewandte Chemie, 2017, 129(3): 814-818.

[217] Mi Y, Shen S, Peng X, et al. Selective electroreduction of CO_2 to C_2 products over Cu_3N‐derived Cu nanowires[J]. ChemElectroChem, 2019, 6(9): 2393-2397.

[218] Lee S Y, Chae S Y, Jung H, et al. Controlling the C_{2+} product selectivity of electrochemical CO_2 reduction on an electrosprayed Cu catalyst[J]. Journal of Materials Chemistry A, 2020, 8(13): 6210-6218.

[219] Chen C S, Handoko A D, Wan J H, et al. Stable and selective electrochemical reduction of carbon dioxide to ethylene on copper mesocrystals[J]. Catalysis Science & Technology, 2015, 5(1): 161-168.

[220] Jiang K, Sandberg R B, Akey A J, et al. Metal ion cycling of Cu foil for selective C–C coupling in electrochemical CO_2 reduction[J]. Nature Catalysis, 2018, 1(2): 111-119.

[221] Gao D, Sinev I, Scholten F, et al. Selective CO_2 Electroreduction to Ethylene and Multicarbon Alcohols via Electrolyte‐Driven Nanostructuring[J]. Angewandte Chemie, 2019, 131(47): 17203-17209.

[222] Hoang T T H, Ma S, Gold J I, et al. Nanoporous copper films by additive-controlled electrodeposition: CO_2 reduction catalysis[J]. ACS catalysis, 2017, 7(5): 3313-3321.

[223] Chen Z, Wang T, Liu B, et al. Grain-boundary-rich copper for efficient solar-driven electrochemical CO_2 reduction to ethylene and ethanol[J]. Journal of the American Chemical Society, 2020, 142(15): 6878-6883.

[224] Lee S Y, Jung H, Kim N K, et al. Mixed copper states in anodized Cu electrocatalyst for stable and selective ethylene production from CO_2 reduction[J]. Journal of the American Chemical Society, 2018, 140(28): 8681-8689.

[225] Jeon H S, Kunze S, Scholten F, et al. Prism-shaped Cu nanocatalysts for electrochemical CO_2 reduction to ethylene[J]. ACS Catalysis, 2018, 8(1): 531-535.

[226] Hoang T T H, Verma S, Ma S, et al. Nanoporous copper–silver alloys by additive-controlled electrodeposition for the selective electroreduction of CO_2 to ethylene and ethanol[J]. Journal of the American Chemical Society, 2018, 140(17): 5791-5797.

LIST OF PUBLICATIONS

1. H Yu, Y Men, EW Shin, Structural properties of disordered macroporous $La_2O_2CO_3$/ZnO materials prepared by a solution combusion method, Korean Journal of Chemical Engineering 36 (4), 522-528.

2. H Yu, K Jiang, SG Kang, Y Men, EW Shin, Hexagonal and Monoclinic Phases of $La_2O_2CO_3$ Nanoparticles and Their Phase-Related CO_2 Behavior, Nanomaterials 10 (10), 2061.

3. H Yu, Y Men, EW Shin, Ethanol conversion over $La_2O_2CO_3$/ZnO catalysts prepared by two methods: the effect of macroporous structure and basic sites, Journal of Shanghai University of Engineering Science.

4. K Jiang, Y Men, S Liu, J Wang, W An, H Yu, E Shin, Highly stable and selective CoxNiyTiO$_3$ for CO_2 methanation: Electron transfer and interface interaction, Journal of CO_2 Utilization, 13, 101743.

5. K Jiang, H Jung, TT Pham, DQ Dao, TKA Nguyen, H Yu, Y Men, EW Shin, Modification of $NiTiO_3$ visible light-driven photocatalysts by Nb doping and NbOx heterojunction: Oxygen vacancy in the Nb-doped $NiTiO_3$ structure, Journal of Alloys and Compounds 861, 158636